Chapter 1

Inelastic X-Ray Scattering as a Probe of the Transition Between the Hydrodynamic and the Single Particle Regimes in Simple Fluids

Alessandro Cunsolo

Additional information is available at the end of the chapter

http://dx.doi.org/10.5772/66126

Abstract

In the last few decades, the study of the spectrum of density fluctuations in fluids at the transition from the continuous to the single particle regimes has attracted an increasing interest. Although the shape of the spectrum is well known in these two extreme limits, no theory firmly predicts its evolution in the broad crossover region. However, the development of inelastic X-ray scattering (IXS) has substantially expanded the potentialities of modern spectroscopy, thus, providing an unprecedented detailed mapping of such a crossover. A better understanding of the line-shape evolution in this intermediate regime is deemed to improve our knowledge of all dynamical processes occurring in a fluid from macroscopic to microscopic scales. The aim of this chapter is to review some relevant experimental contributions brought about by IXS in this field since its development toward the end of past millennium.

Keywords: inelastic X-ray scattering, simple fluids, hydrodynamics, single particle limit, collective excitations

1. Introduction

In the last 50 years, the short-time collective dynamics of molecules in fluid and glassy systems has been in the focus of a thorough experimental, theoretical, and computational scrutiny, yet it still has many unsettled aspects. This mostly owes to the lack of a large-scale symmetry in the structure of these systems and to the often exceptionally complex movements of their microscopic constituents. Among various variables providing insight into the dynamic behavior of a disordered system, density fluctuations are a particularly well-suited subject to

study, as they can be directly accessed by several independent investigation methods. Indeed, the most significant advances made in the field of dynamics of liquids have been achieved thanks to the critical comparison of parallel experimental and computational results. In fact, both spectroscopy experiments and molecular dynamics simulations provide direct access to the Fourier transform of correlation functions between density fluctuations, i. e., the dynamic structure factor, $S(Q,\omega)$. This variable is a unique function of the energy, $\hbar\omega$, and the momentum $\hbar\vec{Q}$ exchanged between the probe and the sample in a scattering event; here $\hbar = h/2\pi$ with h being the Planck constant.

In general, the shape of $S(Q,\omega)$ is reasonably understood both at quasi-macroscopic distances, over which the fluid appears as a continuum, and at truly microscopic scales where instead the single particle dynamics is probed.

The evolution of the $S(Q,\omega)$ shape in the whole crossover between these two limits still represents a theoretical challenge. This particularly applies to the so-called "mesoscopic" regime, corresponding to distances and timescales roughly matching first neighboring molecules' separations and cage oscillations periods, respectively. From the experimental side, the study of $S(Q,\omega)$ in liquids at mesoscopic scales has been for long time an exclusive domain of inelastic neutron scattering (INS), a technique already in its mature phase, having been developed in the mid-1950s [1]. The complementary mesoscopic technique, inelastic X-ray scattering (IXS), is instead relatively young, since its first demonstration dates back to the last decade of the past millennium [2, 3]. Its implementation was enabled by the advent of synchrotron sources with unprecedented brilliance and by parallel advances in crystal optics fabrication. Furthermore, the improved performance of X-ray sources has greatly increased the level of statistical accuracy typically achieved by inelastic scattering measurements, thus enabling more detailed and physically informative modeling of the spetral shape. Across the years, this new spectroscopic tool allowed the scientific community to gain a deep-seated knowledge of the mesoscopic dynamics of disordered systems. Nowadays, IXS experiments have reached the level of statistical accuracy required for extremely detailed and informative line-shape analyses, thus representing a valuable test for the most advanced theories of liquid dynamics.

As a simple example of possible IXS applications, this chapter will provide a concise overview of relevant IXS investigations of the $S(Q,\omega)$ across the transition from the hydrodynamic to the single particle regimes. Looking at the available literature results from a global perspective has a relevant scientific interest since a better understanding of this crossover can shed further insight into the various dynamic events occurring in a fluid from macroscopic to microscopic scales.

2. Generalities on an inelastic scattering experiment

In a scattering experiment, a beam impinges on the sample exchanging with it, an energy of $\hbar\omega$ and a momentum of $\hbar\vec{Q}$. It can be shown that intensity measured in a spectroscopy

http://dx.doi.org/10.5772/66126

experiment from GHz frequencies [4] to THz ones [5–7] is proportional to the spectrum of density fluctuations, or dynamic structure factor:

$$S(Q,\omega) = \int_V d\vec{r} \int_{-\infty}^{+\infty} \left\langle \delta\rho(\vec{r},t)\delta\rho^*(\vec{r},0) \right\rangle \exp\left[i(\vec{Q}\cdot\vec{r} - \omega t) \right] dt \tag{1}$$

with $\delta\rho(\vec{r},t)$ being the space ($\vec{r}$) and time *(t)* dependent density fluctuation of the target sample within the volume *V*. The term $\delta\rho(\vec{r},t)$ appearing in Eq. (1) may represent either a spontaneous or a scattering-induced density fluctuation, in either case its amplitude is assumed small enough to induce a linear response on the target sample. Under this condition, the response of the latter can be expressed in terms of correlation functions calculated at its equilibrium. Note that for isotropic systems as liquids and glasses, only the amplitude $Q = |\vec{Q}|$ of the exchanged wave-vector $\vec{Q}$ counts, the actual direction being irrelevant. For this reason, while dealing with these systems, it is customary to express the dynamic structure factor as $S(Q,\omega)$ rather than $S(\vec{Q}, \omega)$.

Typically, in a scattering experiment the sample is kept at a constant temperature *T* and therefore the correlation function, defined by the symbol ⟨.....⟩, can be calculated as a thermal average over the initial states of the target atoms. For a classical system, this sum can be performed using the counting factor $n(E_I)=\exp(-\beta E_I)\Big/\sum_I \exp(-\beta E_I)$, with $\beta = 1/k_B T$, where E_I is the energy of the *I*-th initial state and k_B, the Boltzmann constant. From the above formula, one readily recognizes that the scattering of a plane wave at an energy (frequency) and a direction (wavevector) different from the initial ones is caused by a density fluctuation $\delta\rho(\vec{r},t)$. If, for instance, if the probe is visible light, the occurrence of a density fluctuation causes a local variation of the index of refraction, thereby disrupting the optical homogeinity of the medium. By virtue of the scattering event, according to the Huygens principle (see, e.g., [8]), the target sample becomes the source of spherical wave: $\psi_{sc} \propto e^{ikr}/r$ with *r* being the distance from the origin, that is the location of the probe-sample collision.

The photoms deviated at an angle 2θ, after passing through an analyzer filter are ultimately counted by the detector. If the latter intercepts only a very small portion of the solid angle, it can be safely assumed that the wavevector of photons impinging on its sensitive area is constant and orthogonal to the front wave (plane wave approximation). Consequently, the scattering process can be treated as a transition between two distinct plane waves.

Given the above general considerations, we can now attempt a course derivation of the frequency distribution of the scattering from a density wave to achieve a rough estimate of the shape of $S(Q,\omega)$.

As apparent from Eq. (1), $S(Q,\omega)$ is connected to density fluctuations through the space and time Fourier transform of their correlation function. Its determination thus provides a snapshot of this correlation function over timescale ~ ω^{-1} and distances ~ Q^{-1}. For small *Q* and ω, the target system is "perceived" by the probe as a continuous and homogeneus medium, whose dynamic response is averaged over long times. This continuous limit can be probed, for

instance, by illuminating the sample with the visible light beam emitted by a laser. In fact, Q values typical of visible light scattering measurements span the 10^{-3}–10^{-2} nm^{-1} range, corresponding to sub-μm to μm lengthscales. These distances are sufficiently smaller than the sample size, yet still much larger than first neighboring atoms' separations. Clearly, at these scales the detail of the microscopic structure and dynamics cannot be directly observed, since only long distances and times effects on the dynamics can be captured by the probe.

Over long distances density fluctuations in a liquid can, for instance, have the form of density (acoustic) waves propagating throughout the medium with the speed of sound, c_s. Since c_s is much smaller the speed of light in the medium a given density wave is "seen" by the incident photons as essentially static, i. e., stationary, perturbation.

We can now focus on the intensity scattered, e.g., by successive crests of the density wave, as illustrated in **Figure 1**. The interference between these successive reflections is constructive whenever the difference in their optical paths (namely, the two red segments in the scheme of **Figure 1**) equals an integer multiple of the incident wavelength in the medium. Considering the smallest of these integer numbers, one has:

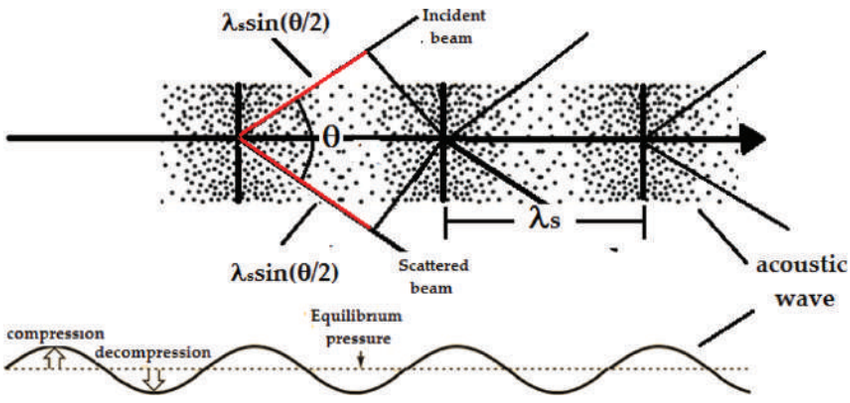

Figure 1. Schematics of the interaction between a density wave and a photon beam (see text) causing a scattering at an angle 2θ.

$$\frac{\lambda}{n} = 2\lambda_s \sin\vartheta = 4\pi \frac{c_s}{\omega_s} \sin\vartheta \tag{2}$$

where λ and λ/n are, respectively, the wavelength of light in vacuum and in the target medium, with n being the refractive index of the sample; furthermore, λ_s, c_s, and ω_s are the wavelength, the speed and the angular frequency of the acoustic wave with $\lambda_s = 2\pi c_s/\omega_s$. The scattering-genearted acoustic wave has a wavevector of amplitude amplitude = Q, therefore it propagates at a frequency $\omega_s = c_s Q$. From Eq. (2) it follows that the amplitude of the exchanged wavevector is $Q = (4\pi n/\lambda) \sin\theta$.

From a physical point of view, the acoustic wave can be considered as a source of scattered radiation traveling with a velocity c_s. As well known from Physics textbooks, the frequency of

http://dx.doi.org/10.5772/66126

the radiation emitted by a moving source is frequency-shifted by the Doppler effect. This ultimately causes $a \pm c_s Q$ offset of the frequency of scattered wave with respect to the one of the incident beam; here the signs "+" and "−" refer to the acoustic wave propagating toward or away from the detector, respectively. From these very general arguments, one can expect the frequency distribution of the scattered intensity, i.e., the spectrum, to be dominated by two peaks symmetrically shifted by an amount $\pm c_s Q$ from the center of the spectrum, $\omega = 0$.

These peaks are customarily quoted as "inelastic" insofar their energy is either lower or higher (by an amount $E = \hbar c_s Q$) than the energy of the impinging beam.

The two symmetric side peaks are named Brillouin peaks after their prediction by L. Brillouin in the early 1920s [9] and, as discussed in the following, their position and width convey insight, on the frequency and the lifetime of acoustic waves, respectively.

Let us now consider the case of diffusive, rather than propagating, density fluctuations. These can be for instance those generated by local temperature gradients causing transient density inhomogeneities. Their time evolution can be described by the Fick's law [10], which predicts a simple exponential time decay. The corresponding spectral shape is the Fourier transform of such an exponential law, namely a Lorentzian centered at $w = 0$. Since this position corresponds to the absence of energy-transfer, the corresponding peak is thus customarily referred to as quasi-elastic. Here the prefix "quasi-" alludes to the nonvanishing width of the peak and to its wings extending to the inelatic region of the spectrum ($w \neq 0$).

Since in general density fluctuations in a fluid can have either a diffusive, or a propagating character, one can anticipate that the spectrum of density fluctuations has a triplet shape composed by a quasi-elastic peak—connected to internal diffusive motions—and two symmmetric side peaks— arising from acoustic modes.

A physically more informative description of the spectral shape in the continuous limit requires a detailed knowledge of the thermodynamic and transport properties of the sample. As well assessed both experimentally and computationally, the hydrodynamic theory for continuous media can be consistently used to describe the spectral shape in this limit.

This theory stems from an explicit expression of the conservation laws of the density of mass, momentum, and energy of the target sample [4, 11]. These can be described by few independent equations, which, however, do not form a complete set unless complemented by two so-called constitutive equations: the Navier-Stokes equation and the heat transfer one. The spectrum of density fluctuation can be ultimately obtained through Fourier and Laplace transforms of this set of equations. The result can be conveniently expressed in terms of a hydrodynamic matrix, whose eigenvalues define the modes dominating the spectral shape. As shown in Ref. [4] these long-lived, or quasi-conserved, collective modes are customarily referred to as "hydrodynamic modes," and appear in the spectrum as a triplet, well approximated by the following expression:

$$S(Q,\omega) \propto A_h \frac{z_h}{\omega^2 + z_h^2} + A_S \left[\frac{z_S}{(\omega - \omega_S)^2 + z_S^2} + \frac{z_S}{(\omega + \omega_S)^2 + z_S^2} \right] + \\ + A_S b \left[\frac{(\omega - \omega_S)}{(\omega - \omega_S)^2 + z_S^2} - \frac{(\omega + \omega_S)}{(\omega + \omega_S)^2 + z_S^2} \right] \tag{3}$$

where the shape parameters ω_s, z_h and z_s represent the acoustic frequency and the inverse lifetime of the quasi-elastic and inelastic modes, respectively. All shape parameters in Eq. (3) are in general Q dependent, even if such dependence is not explicitly mentioned in the notation.

At low Q values, such a Q-dependence can be made explicit using a polynomial Q-expansion (see, e.g., [12]), which to the lowest order yields:

$$\omega_s \approx \omega_s^{hyd} = c_s Q \tag{4a}$$

$$z_s \approx z_s^{hyd} = \left[(\gamma - 1) D_T + \nu_L \right] Q^2 / 2 \tag{4b}$$

$$z_h \approx z_h^{hyd} = D_T Q^2 \tag{4c}$$

with c_s, D_T, and υ_L being, respectively, the adiabatic sound velocity, the thermal diffusivity, and the longitudinal kinematic viscosity.

One readily recognizes that Eq. (3) consists of these components (from left):

1. The so-called Rayleigh, or central, peak (term $\propto A_h$) which relates to entropy (heat) fluctuations diffusing at constant pressure (P).
2. The two Brillouin side peaks (term $\propto A_S$), connected to P-fluctuations propagating at constant entropy, and
3. An additional contribution (term $\propto A_S b$) asymmetric around the Brillouin peaks position having negative tails. This term distorts the Lorentzian terms (1) and (2) ultimately enabling the convergence of spectral moments $\int_{-\infty}^{+\infty} \omega^n S(Q, \omega) d\omega$ for $n \leq 2$. The latter imposes the following constraint: $b = [A_h z_h / (1 - A_h) + z_s] / \omega_s$.

The Rayleigh-Brillouin triplet in Eq. (3) is customarily quoted to as either generalized or simple hydrodynamic spectrum, respectively with or without the lowest order Q approximation in Eqs. (4a)–(4c).

It is worth stressing that the shape in Eqs. (3) and (4a)–(4c) provides an accurate description of the spectrum only when $D_T Q^2$, $\Gamma Q^2 << c_s Q$, or, equivalently, as long as the lifetime of hydrodynamic modes is much longer than the acoustic period. In this regime the spectrum is

dominated by three sharp peaks, forming the so-called Rayleigh-Brillouin triplet, typically measured in Brillouin light scattering (BLS) experiments.

Figure 2 displays the generic shape of the Rayleigh-Brillouin triplet from a liquid along with its three individual spectral components.

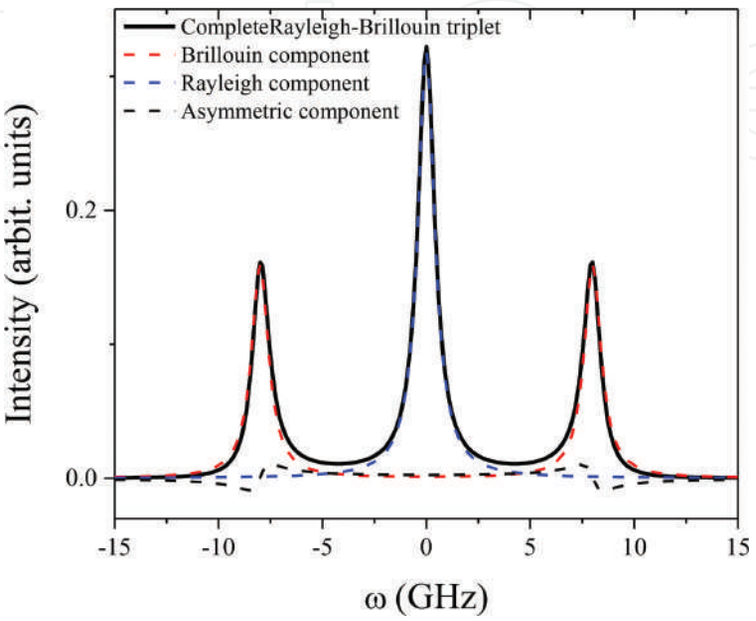

Figure 2. Typical shape of the Rayleigh-Brillouin triplet measured by Brillouin light scattering. The separate contributions to the total shape are represented by lines of different color, as indicated in the legend.

In general, the shape of the spectrum determined by a scattering experiment strongly depends on the probed space and time (or, equivalently, Q and ω) window, however the analytical form of such a dependence is generally unknown. Indeed, this is exactly known only at extreme Q and ω values: either extremely small (hydrodynamic limit-discussed above) or extremely large (single particle limit, to be discussed in Section 5).

At the crossover between these two limits, the shape of $S(Q,\omega)$ becomes highly sensitive complex dynamical processes involving inter and intramolecular degrees of freedoms. The coupling of density fluctuation with the mesoscopic dynamics of fluids makes the investigation of their spectrum of prominent interest.

3. The persistence of hydrodynamic modes beyond the continuous limit: first INS results

In principle, a "bare" extension of the hydrodynamic description of $S(Q,\omega)$ to the so-called mesoscopic regime would appear suspicious, since at those scales the matter can no longer be considered as continuous, or stationary. In fact, this regime corresponds to distances and times comparable with atomic separations and cage oscillations periods, respectively. Nonetheless,

sound arguments can still be used in support of a suitably generalized hydrodynamic description in this range. To understand this point, it is useful to recognize that for a dense liquid the mean free path can span the (10^{-1} nm) window, thus possibly becoming even smaller than interatomic separations. Under these conditions, the movements permitted to the atoms mainly resemble rapid, vibration-like, cage oscillations in the 0.1 ps window.

Consequently, even at mesoscopic (nm, ps) scales the response of the system is still "averaged" over a large number of elementary dynamic interactions, as required by a suitably generalized hydrodynamic description to hold validity. Based upon the above argument, possible reminiscences of Brillouin peaks in the THz spectrum of fluids appeared as an intriguing, yet somehow realistic, possibility since the early development of INS methods, which motivated several pioneering INS investigations in the mid-1960s.

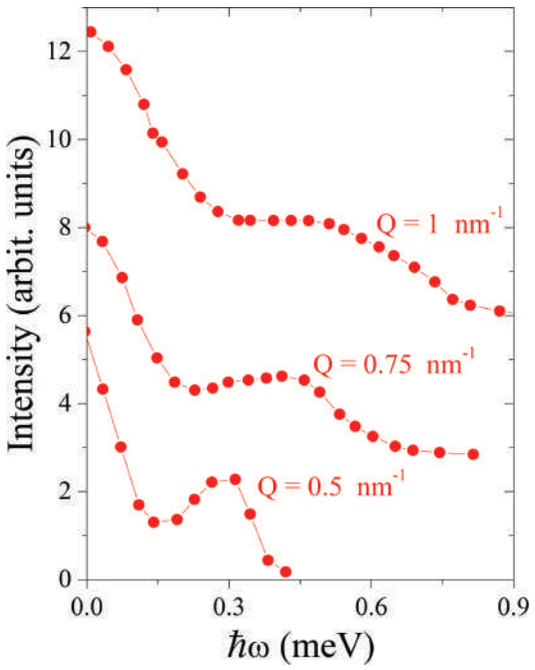

Figure 3. Few representative INS spectral line shapes of Ar measured by Bafile et al. [19] at low exchanged wave-vectors. Reported spectra have a mutual vertical offset for clarity.

Unfortunately, the first results reported in the literature were mutually inconsistent. In fact, the persistence in the spectrum of side shoulders reminiscent of hydrodynamic modes was suggested by Chen et al. [13] and successively confuted by Kroô et al. [14]. The former INS work focused on several samples having a strongly coherent neutron-scattering cross-section, as Ne, Ar, and D_2, and showed that, at low *Qs*, the frequency shift of side peaks approached from the above linear hydrodynamic law predicted by Eq. (4a) This pinpointed a link between these high frequency spectral features and the Brillouin peaks dominating the spectrum at much lower *Q*s. In a further INS work on Ar in both liquid (at $T = 94$ and 102 K) and solid (at $T = 68$ and 78 K) phases, Sköld et al. [15] found close resemblances between the phonon dispersion curves of a liquid and the one of a solid, thus suggesting that the local pseudo-periodicity of the liquid structure gives rise to quasiperiodic zones reminiscent of the Brillouin

http://dx.doi.org/10.5772/66126

zones of a crystal. A similar conclusion was previously reached by an INS investigation on liquid Pb [16], as well as a computer simulation on liquid Rb [17].

Coming back to noble gases, the first convincing evidence of well-defined inelastic peaks beyond the hydrodynamic regime is suggested by an INS measurement of Bell and collaborators on supercritical neon [18]. The low Q values explored in such a work ($0.6\ nm^{-1} \leq Q \leq 1.4\ nm^{-1}$) substantially reduced the dynamic gap between neutron and visible light Brillouin scattering techniques. The results demonstrated that the simple hydrodynamic theory consistently describes the spectral shapes well beyond the continuous limit and at least down to few nanometers distances. In particular, the inelastic shift of side peaks had, reportedly, a linear Q-dependence, whose slope is consistent with the adiabatic sound velocity.

Almost two decades after the measurement by Bell et al. on Ne, further low Q INS measurements were performed by Bafile et al. on supercritical Ar [19]. Again, the spectral line-shape measured in this work clearly confirmed the persistence of extended Brillouin peaks beyond the hydrodynamic limit (see **Figure 3**).

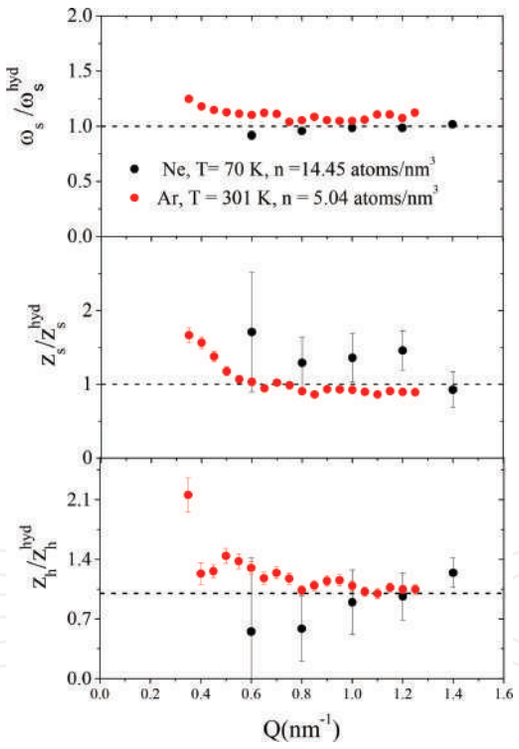

Figure 4. Shape parameters of the $S(Q,\omega)$ reported by Refs. [18, 19] for Ne and Ar, respectively, under the indicated thermodynamic conditions. Data are normalized to the corresponding hydrodynamic values as derived from Eqs. (4a)–(4c). Transport parameters in Eqs. (4a)–(4c) were extracted either from original works or from the database of the National Institute of Standards and Technology (NIST).

The extremely low Q range explored by this work ($0.35\ nm^{-1} \leq Q \leq 1.25\ nm^{-1}$) further reduced the gap separating standard INS measurements from light scattering ones. The INS investigation of Bafile and collaborators took full advantage of the improved statistical accuracy in

the beam counting and the unprecedented fine Q-grid. Both these assets enabled a very precise determination of the Q-dependence of line-shape parameters in Eq. (3).

Best-fit values of such parameters derived from [19] are reported in **Figure 4** after normalizations to the respective simple hydrodynamic predictions, expressed by Eqs. (4)–(4). The corresponding quantities derived by Bell and collaborators for neon [18] are also reported for comparison.

Data reported in **Figure 4** demonstrate that the simple hydrodynamic laws in Eqs. (4a)–(4c) derived for continuous media hold validity up to the ≈ 1 nm^{-1} mesoscopic Q-range. This result is certainly surprising since at these Q's the spectral peaks gradually transform into broad features (see, e.g., **Figure 3**) for which the simple hydrodynamic approximation ($D_T Q^2$, $\Gamma Q^2 << c_s Q$) becomes clearly inaccurate. In Ref. [19] these high frequency inelastic features are quoted to as "extended hydrodynamic modes," which emphasizes their hydrodynamic-like behavior persistent well beyond the continuous limit.

4. The advent of inelastic X-ray scattering

The only *THz* spectroscopic technique available until the mid-1990s, INS, is intrinsically hampered by kinematic limitations (see, e.g., [5] pp. 63–101). These shrink the accessible portion of dynamic plane (Q,ω) especially at low Qs, where the collective modes dominate. This problem was successfully addressed by the development of IXS, a technique virtually free from kinematic limitations [2, 3], apart from, of course, those arising from finite energy resolution width. Toward the end of past millennium, the availability of this new spectroscopic tool revitalized the interest toward experimental studies of the transition from the continuous to the mesoscopic regime. It is important to stress that noble gases present undoubted advantages in this kind of studies. In fact, at variance of molecular fluids, their microscopic components lack internal degrees of freedom and contrary to, e.g., metallic liquids, microscopic interactions are simpler and shorter-ranged. These, for instance, are key assets to reliably approximate the interatomic potential when performing molecular dynamics (*MD*) simulation studies [20]. Another advantage of gaseous systems in general is the large compressibility, which permits substantial variations of density, that is the strength of atomic interactions, even with moderate thermodynamic changes.

The first IXS measurement on a dense noble gas was performed on deeply supercritical neon (T = 295 K, n = 29.1 atoms/nm^3) in 1998. Experimental results were discussed in combination with the outcome of a parallel *MD* simulation on a Lennard-Jones model representative of the same sample [21]. In **Figure 5**, some of the IXS spectra discussed in this work (and, successively in Ref. [22]) are compared with the best-fitting line-shape obtaining using Eq. (3) as a model, without any constraint on the Q dependence of shape parameters. In this case the persistence of a triple peak structure at mesoscopic scale can be inferred at least up to Q = 6 nm^{-1}, while at Q = 10 nm^{-1} or higher the two shoulder can be no longer easily discerned in the IXS spectral shape.

http://dx.doi.org/10.5772/66126

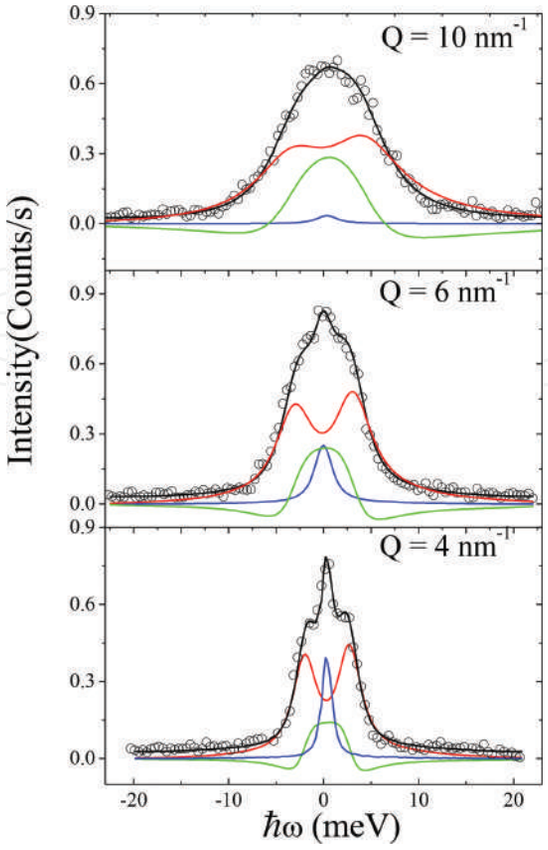

Figure 5. Some representative spectral shapes (circles) of deeply supercritical neon at P = 3 kbar and ambient temperature reported in [22] are compared with corresponding best-fitting line shapes (black lines) and their quasi-elastic (blue), inelastic (red) and "negative tails" (green line) components. These are obtained using Eq. (3) as a model for the spectral shape.

4.1. The Q-dependence of the spectral shape parameters

At this stage a question may arise on the Q dependence of inelastic peaks beyond the extremely low Q (<1nm^{-1}) extended hydrodynamic regime probed by Brillouin neutron scattering. A meaningful answer to this question is provided by the IXS results displayed in **Figure 6**, which illustrates the results reported in [21] and also discussed in [22]. These data refer to deeply supercritical neon at room temperature and 3 Kbar pressure. Plotted data appear paradigmatic of an IXS measurement on a simple, hard sphere-like, system of a supercritical dense gas. The curves are compared with the trends expected in the simple hydrodynamic limit, as obtained by inserting in Eqs. (4a)–(4c) the transport parameters derived from the National Institute of Standards and Technology (NIST). It can be readily noticed that the Q-dependence of ω_s is linear within a Q range extending up to $Q \approx 10$ nm^{-1}, the slope being consistent with the adiabatic sound velocity of the sample (1050 m/s). The Q-interval spanned by this linear trend corresponds to distances larger than about .6 nm, a value higher, yet comparable, with first neighboring atoms separations. This indicates that an extended hydrodynamic behavior can be still observed at Q higher by a decade than those previously investigated by Bell et al. [18] and Bafile et al. [19].

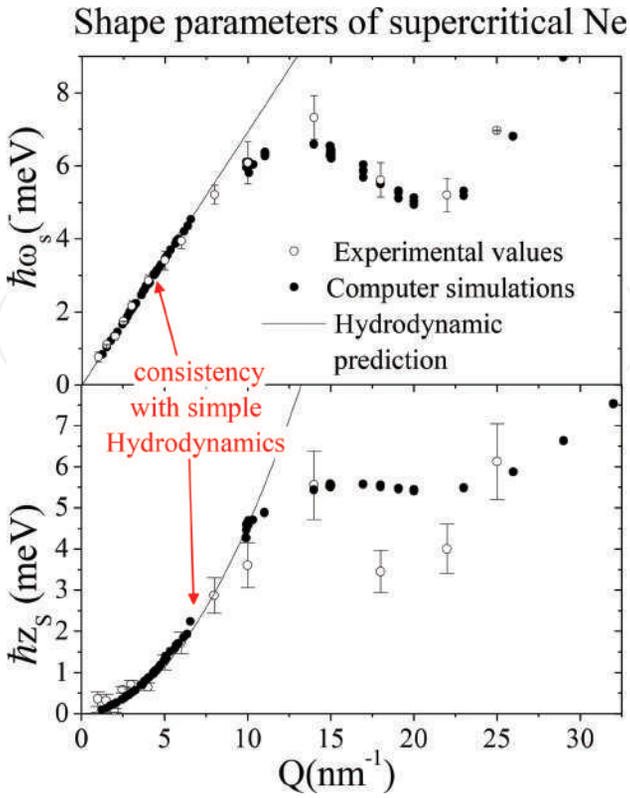

Figure 6. Shape parameters of the inelastic modes of $S(Q,\omega)$, as derived for supercritical Ne by IXS (circles [22]) and MD simulations (dots [21]). The solid lines represent the hydrodynamic predictions derived from Eqs. (4a) and (4b), while inserting in them thermodynamic and transport parameters from [28] and from [29], respectively.

4.1.1. The role of the static structure factor

From **Figure 6** one readily notices that beyond $Q = 10$ nm^{-1} the extended acoustic frequency ω_s bends down to a minimum at about 22.5 nm^{-1}. This turns out to be the same Q value where the structure factor $S(Q)$ (not reported in the plot) reaches its first maximum. We recall here that the static structure factor is related to the $S(Q,\omega)$ by the simple relation:

$$S(Q) = \int_{-\infty}^{\infty} S(Q,\omega)\, d\omega \tag{5}$$

Upon inserting Equation (1) i the formula above, it readily appears that the ω-integration of $S(Q,\omega)$ introduces a term $\propto \delta(t) = 1/2\pi \int_{-\infty}^{\infty} \exp[i\omega t]dt$, which, as well known, is nonvanishing only for $t = 0$. It follows that $S(Q)$ essentially measures the "static" ($t = 0$) value of density correlations, rather than the dynamic one probed by $S(Q,\omega)$. Therefore, $S(Q)$ carries direct insight into time-independent or structural properties of the fluid, which justify the name "static structure factor," customarily used for this variable. Alternatively, $S(Q)$ is often referred to as diffraction

http://dx.doi.org/10.5772/66126

profile as directly determined by diffraction measurements. These are frequency integrated measurements of the scattering and, as such, not directly sensitive to the dynamic (*t*-dependent) properties of the sample.

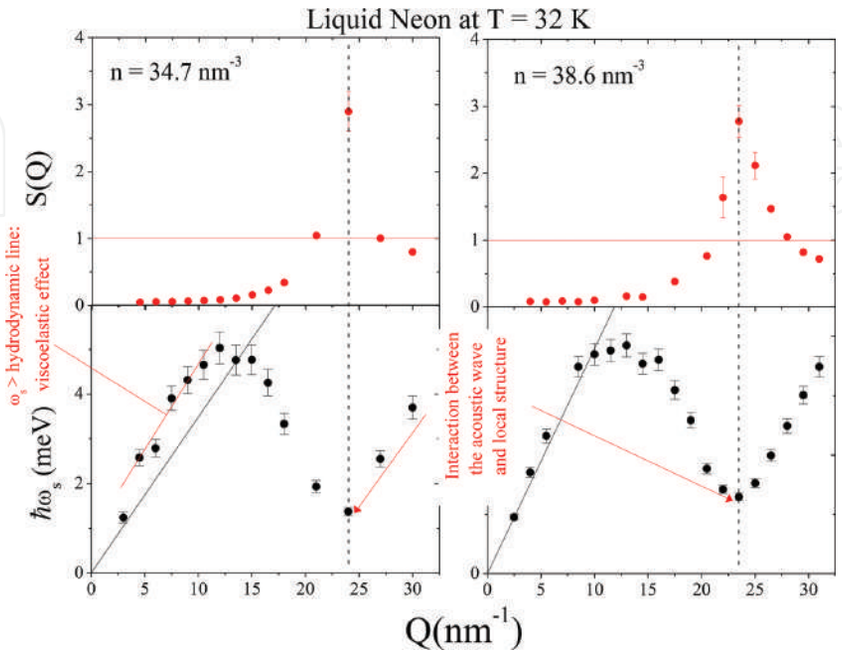

Figure 7. The dispersion liquid neon (bottom panels) are compared with the diffraction profiles *S(Q)* (upper panels), both being derived from IXS measurements discussed in Ref. [24] The vertical dashed lines indicates the essentially coincident *Q*-position of minima and maxima of ω_s and *S(Q)*, respectively. Horizontal lines in the upper plots indicate the asymptotic large *Q* unit value. The dispersive effects discussed in the text are labeled and indicated by arrows.

Typical *S(Q)* profiles of a liquid are reported in **Figures 7** and **9**. In all reported curve one readily notices the presence of a sharp maximum at some exchanged wavevector, $Q = Q_m$ for which $Q_m = 2\pi/a$, with a being the average distance between first neighboring atoms. Furthermore, it clearly appears from **Figure 9** that beyond the first diffraction peak the *S(Q)* displays oscillations from the unit limiting value, which is reached at extremely high *Q*'s. As discussed in Section 5 in further detail, these oscillations are induced by coherent or "pair" interactions. In crystalline solid pair, interactions are much stronger and this is reflected by the circumstance that the diffraction profile, rather than highly damped oscillations, displays narrow and exceptionally intense spots (Bragg peaks) [23].

4.2. The physical meaning of the dispersion minimum

The coincidence between the positions of the first *S(Q)* maximum and the ω_s minimum is an ubiquitous feature of liquids, clearly exemplified in **Figure 7**. There, the dispersion curve and corresponding static structure factor are compared as derived from the modeling of IXS spectra of liquid Ne [24]. The vertical dashed line shows unambiguously the coincidence between the *S(Q)* maximum and ω_s minimum. Indeed, both effects appear as a manifestation of the interference between the density fluctuations and the pseudo-periodicity of the local structure.

Specifically, a maximum in *S(Q)* is observed when the probed distance, Q^{-1}, roughly matches the first neighboring atoms' separation. Under this condition, the presence of an "interference node" (the first neighboring atom) causes a sharp minimum in the density wave dispersion.

This minimum arises from the coexistence of an acoustic wave "transmitted" through the node — for which $\partial\omega_s/\partial Q > 0$ (positive group velocity)—and one reflected by it— for which $\partial\omega_s/\partial Q < 0$ (negative group velocity). It is commonly observed that the sharpness of this minimum deeply enhances upon approaching the solid phase. This suggests that, at mesoscopic scales, dispersion of a dense liquid resembles the one of its crystalline counterpart.

4.3. The slowing down of the dynamics

Figure 6 clearly shows that beside the extended sound frequency ω_s, also the half-width of the sound mode, $z_{s,}$ reaches a local minimum at Q_m and, although non reported in the figure, a similar behavior is observed for the quasielastic half-width z_h [25]. The occurrence of a minimum in z_h was predicted by De Gennes [26], the effect having been named after him the "De Gennes narrowing." More in general, a large body of IXS results on liquids demonstrates that all relevant timescales defining the dynamics of density fluctuations undergo a clear enhancement at Q_m. This global slowing down of the dynamics stems from the higher correlation between the movements of the atoms and those of the respective first neighbor cages for $Q = Q_m$. As noticed by Sköld [27] *S(Q)* yields a measure of the effective number of atoms contributing to the scattered intensity at a given exchanged wave vector Q. It seems thus natural to ascribe the slowing down at Q_m to the higher inertia of the target system due to the larger number of atoms participating to the collective response of the target system. In particular, first neighbor movements become more correlated when Q matches the inverse of first neighbor's separations and *S(Q)* approaches its first maximum. One can thus identify the quantity $Q^* = Q/\sqrt{S(Q)}$ as the momentum "effectively" transferred, where the factor $\sqrt{S(Q)}$ embodies the inertia of the target system [27]. For a perfect crystal, owing to the global periodicity of first neighbors' arrangement, such a factor diverges when Bragg conditions are met. Here the whole target system coherently participates to density fluctuations and, correspondingly, an infinitely narrow intrinsic spectral linewidth is to be expected. Furthermore, the effective inelastic shift, proportional to Q^*, tends to vanish as $1/\sqrt{S(Q)}$.

4.4. The onset of viscoelastic effects

A noticeable feature displayed by the left bottom plot of **Figure 7** is the clear inconsistency between the low-intermediate Q region of the dispersion curve and the corresponding linear hydrodynamic prediction.

Although a detailed description of this effect goes beyond the scope of this chapter, it is useful to recall here that this is a manifestation of the viscoelastic response induced by the coupling with a relaxation process.

To better illustrate this point, it is useful to recall that scattering-excited density fluctuation causes a time-dependent perturbation of the local equilibrium of the target sample. As a

response, decay channels redistribute the energy from the density fluctuation toward some internal degrees of freedom, thus ultimately driving the sample to relax into a new local equilibrium within a timescale τ.

Two limiting scenarios can thus occur:

1. the time-dependent acoustic perturbation has a timescale much longer than any internal degrees of freedom of the system. Under these conditions, the latter relaxes to equilibrium "instantaneously" and the density fluctuation propagates or diffuses over successive equilibrium states (**viscous**, or liquid-like, limit);
2. If the density fluctuation is instead extremely rapid, it "perceives" internal rearrangements as frozen-like and does not couple with them thus virtually evolving with no energy losses (**elastic** or solid-like limit).

If such considered perturbation has the form of an acoustic wave, its transition from the viscous to the elastic limit is accompanied by a decrease of dissipation and a consequent increase in the propagation speed. Therefore a **viscoelastic** transition manifests itself through a systematic increase of sound velocity with Q. While the hydrodynamic theory correctly predicts (through Eq. (4a)) the Q-dependence of ω_s in the viscous limit, it fails to predict its elastic value at intermediate Qs. This explains the discrepancy between the hydrodynamic straight line and the actual value of the inelastic shift in the 5 $nm^{-1} < Q < 14$ nm^{-1} range, as evidenced in the bottom left plot of **Figure 7**.

5. Moving toward the single particle limit

Upon reaching extremely high Q values, the probed dynamic event gradually reduces to the free recoil of the single particle after the collision with the probe particle and before any successive interactions with the first neighbors' cage.

Within these short times, the struck atom can be assumed to freely stream without interacting with the neighboring cage, its equation of motion being thus expressed as $\vec{R}_j(t)=\vec{v}_j t$.

This merely "ballistic" behavior can be easily understood for a system of hard spheres, in which microscopic interactions essentially consists of atomic collisions, i.e., interactions instantaneous and localized in space. For a more realistic system, atomic interactions can no longer be considered as "close contact", rather spanning finite distance and time lapses. However, if the energy transferred in the scattering event is much larger than any local interaction, the struck particle can still be "perceived" as freely recoiling from the collision with the probe. In this so-called impulse approximation (IA) regime it can be safely assumed that no sizable external force acts on the isolated system formed by the incident photon and the struck atom.

Within the unrealistic hypothesis that the target atom is exactly at rest, its response function would reduce to a delta function centered at the recoil energy. More realistically, one can assume that the initial state of the system is characterized by a distribution of initial momenta, and the spectrum scattered by this moving source therefore becomes "Doppler broadened."

Each possible initial momentum provides a contribution to the scattering intensity and the shape of the spectrum is directly connected to the momentum distribution of the struck particle.

For a classical particle this can be assumed to have the form of a Maxwell-Boltzmann distribution $\propto \exp\left(-Mv^2/2k_BT\right)$, where M is the atomic mass. Disregarding the analytical details of the derivation (thoroughly discussed, for instance, in Ref. [5]), it is here important to mention that the use of the Boltzmann distribution ultimately yields the following Gaussian shape for the dynamic structure factor:

$$S_{IA}(Q,\omega) = \left(\frac{M}{2\pi k_B T Q^2}\right)^{1/2} \exp\left[\frac{M\hbar}{2\pi k_B T Q^2}(\omega-\omega_r)^2\right] \tag{6}$$

where the suffix "IA" labels the impulse approximation value of $S(Q,\omega)$. One readily recognizes that profile in Eq. (8) is a Gaussian centered at $\omega=0$ and its variance, k_BTQ^2/M, can be simply related to the mean kinetic energy of the struck particle ($\langle K.E.\rangle = 3/2k_BT$ for a monatomic system). It can be shown that for a quantum system, the *IA* spectrum preserves the Gaussian shape; however, its variance deviates from the classically expected values being instead simply determined by the quantum value of $\langle K.E.\rangle$. Since the latter is in general unknown, a useful application of extremely high Q measurements is to achieve a direct determination of its value (see, e.g., Ref. [30]). Another interesting application is the determination of actual shape of the momentum distribution, e.g., in intriguing quantum system as Bose condensates [31].

The study of the spectrum of simple fluids in the IA regime [32] has been for decades an essentially exclusive domain of deep inelastic neutron scattering (DINS). The first deep inelastic X-ray scattering (DIXS) investigations of the IA spectrum of liquids were pioneered by a work on liquid neon at the onset of the new millennium [33].

In this work, it was found that the single particle kinetic energy extracted from the spectral shape provided clear evidence for quantum deviations.

An example of the gradual evolution of the IXS spectrum toward the single particle Gaussian shape predicted by Eq. (6) is illustrated in **Figure 8**.

DIXS experiments are not common in the literature since this technique suffers from major intensity penalties due to the high Q decay of the form factor. Furthermore, these studies often deal with samples having a light atomic mass (as He, D_2 and H_2, and Ne), as better suited to observe quantum effects. Unfortunately, these systems have also a small atomic number which makes their IXS cross-section rather weak. Finally, the highest Q's reachable by DIXS are still below typical values covered by DINS measurements by more than an order of magnitude. These intrinsic and practical difficulties explain why DIXS experiments are still sporadic and this technique is still in its "infancy."

http://dx.doi.org/10.5772/66126

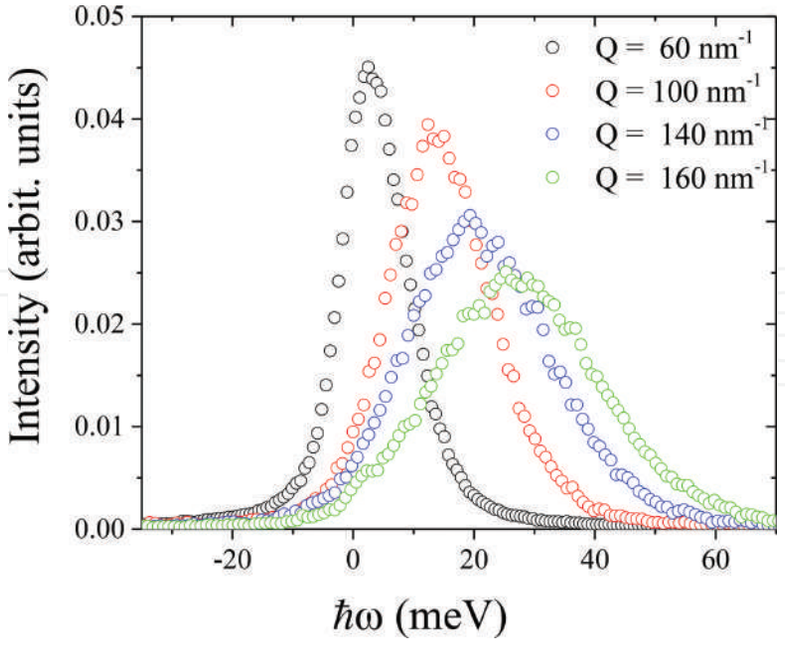

Figure 8. The gradual *Q*-evolution of the IXS spectrum of Ne [33] toward the Gaussian shape characteristic of the single particle regime.

It is important to stress that the IA regime is only joined asymptotically at extremely high *Q*s. Before this limit is fully reached, the struck atom cannot be considered as a freely recoiling object and first neighbor interactions need to be taken into account explicitly. It is usually assumed that the latter influence only the final (after scattering) state of the struck particle, while its initial state being still essentially "free." Among various recipes to handle theoretically these "final state effects," the so-called additive approach [34], is the one used in the very few extremely high *Q* IXS measurements available [33, 35, 36]. This approach stems from an expansion of the intermediate scattering function in time cumulants, in which only the first few lower order term are retained. As a results of this perturbative treatment, deviations from a perfect Gaussian shape can be easily linked to the lowest order (n) spectral moments and contain valuable information on meaningful physical parameters as, e.g., the mean force acting on the atom and the mean square Laplacian, both providing a meaningful and unique characterization of quantum effects (see, e.g., [33]).

5.1. The case of molecular systems

After the work of Monaco et al. on a monoatomic fluid [33], a successive *D*IXS work [35] aimed at investigating the next simplest case of a diatomic homonuclear system as liquid iodine. In this work, no signature of quantum effects was reported due to both the larger molecular mass and the higher temperature of the sample.

Even in the absence of quantum deviations, the interpretation of the IXS spectrum of a molecular fluid is overly complex, owing to the coupling of the spectroscopic probe with all molecular degrees of freedom [37] as well as their mutual entanglement. In the simplest assumption that all degrees of freedom are decoupled and belong to very disparate energy

windows, the observed response strongly depends on how the exchanged energy, E compares not only with centers of mass translational energies, E_t, but also with intramolecular rotational and vibrational quanta, $\hbar\omega_r$ and $\hbar\omega_v$, respectively.

Specifically, three complementary *IA* regimes can be identified:

- When $E_t << E << \hbar\omega_r, \hbar\omega_v$ the struck molecule is "seen" by the probe as an object with spherical symmetry experiencing a merely translational recoil induced by the collision with the probe. The energy of such a recoil energy is $\hbar^2 Q^2 / 2M$, with M being the molecular mass. Here the scattered intensity carries direct insight into the merely translational momentum distribution of the molecular centers of mass.

  In an intermediate window ($E_t, \hbar\omega_r << E << \hbar\omega_v$), usually referred to as the $Sachs-Teller\,(ST)$ regime [38], the molecule behaves as a freely recoiling rigid roto-translator. In this Sachs-Teller regime, the rotational component of the recoil can be written as $\hbar^2 Q^2 / 2M_{ST}$, in which the effective, or Sachs-Teller mass, M_{ST}, is determined by the eigenvalues of the molecular tensors of inertia. In this regime, the spectral density becomes proportional to the distribution of roto-translational momenta of the molecules. The DIXS work in Ref. [35] demonstrated that the Sachs-Teller theory provides a consistent interpretation of the spectral shape of iodine at the largest Q values covered by state-of-art IXS spectrometers.

- Eventually, when the $E >> \hbar\omega_{r,v}$ condition is matched, the exchanged energy becomes overwhelmingly stronger than any intramolecular and intermolecular interaction, therefore, the nucleus inside the molecule is for short-time freed from its bound state experiencing a recoil as a free particle. Under these conditions, the scattering intensity becomes proportional to the single proton initial momentum distribution.

  In principle, at higher exchanged energies and momenta higher-level IA regimes can be probed. This happens when energies transferred in the scattering event are much larger than intranuclear interaction and, correspondingly, subnuclear particle start experiencing free particle recoils. These phenomena belong to a domain of physics complementary to condensed matter Physics and rather fitting in the fields of high energy and particle physics.

6. Summarizing the state of the art of IXS technique

In conclusion, the relevant phenomenology of the spectral evolution from the hydrodynamic to the single particle regime discussed in this chapter is summarized in **Figure 9**. There, the whole crossover of the spectral shape from the hydrodynamic Brillouin triplet to the single particle Gaussian is reported as determined in separate inelastic measurements. The corresponding Q window are indicated in reference to the various regions of the diffraction profile *S(Q)*, reported in the center of the figure. It can be readily noticed that, while "climbing" the wings of the first diffraction peak, the sharp Brillouin triplet (Panel A) gradually transforms into a more complex shape in which the side peaks appear as broad features (Panels B). When Q values become comparable or higher than the position of the dominant S(Q) peak (Panel C),

http://dx.doi.org/10.5772/66126

these shoulder can no longer be resolved due to their intrinsic overdamping. The best-fit components of the spectrum, also reported for the spectra in Panel C, can help to better identify the presence of these "generalized hydrodynamic" modes. Upon further increasing *Q*, "coherent" oscillations of *S(Q)* gradually damp out and correspondingly the shape of the spectrum transforms into a Gaussian centered at the recoil energy (Panel D). This gradual evolution can be readily captured by comparing the measured shape with the Gaussian profile in Eq. (6).

Great expectations are raised by the advent of new generation IXS spectrometers further reducing the dynamic gap separating IXS from Brillouin light scattering [39]. This will possibly revitalize the dream of entire generations of condensed matter physicists: a single inelastic spectrometer covering the relevant portion of the crossover from the hydrodynamic to the single particle regimes. Parallel advances in the theory of the spectrum of fluids and the empowering of simulation methods are deemed to improve our understanding of this crossover and all dynamical phenomena happening in a fluid from macroscopic to microscopic scales.

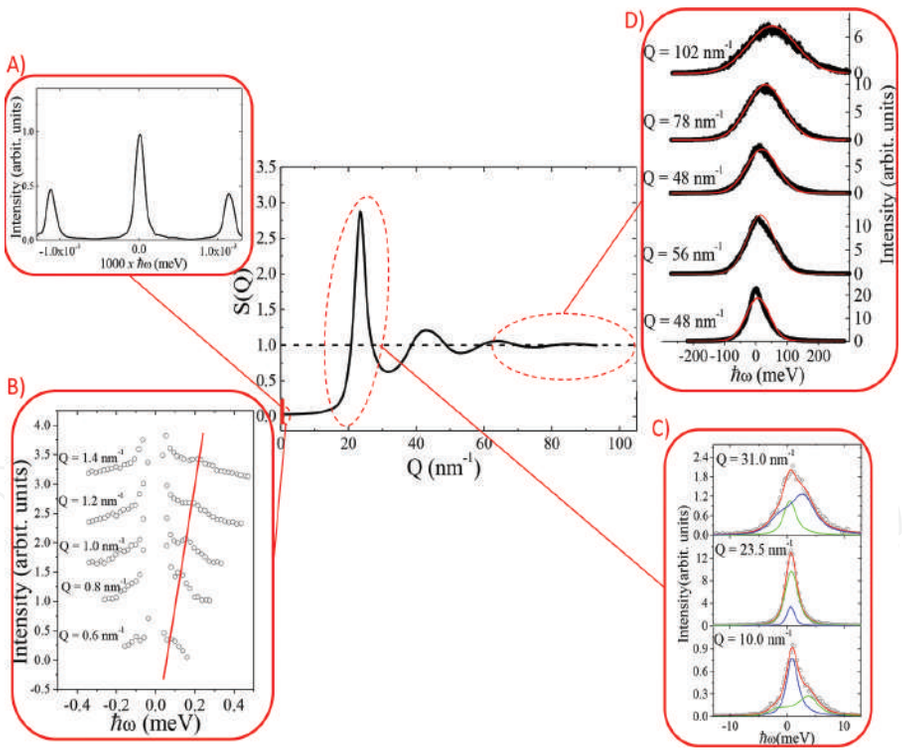

Figure 9. Overview of experimental spectra measured in several *Q* windows across the transition from the hydrodynamic to the single particle regime in monatomic fluids. Panel A reports Brillouin light scattering spectra of liquid Ar [40]. Panel B displays INS measurements on supercritical Ne [18] with the red line roughly indicating the linear dispersion of side peaks. Panel C shows IXS spectra on liquid Ne [24]) with corresponding best-fitting line shapes and individual spectral components. Finally, Panel D displays IXS spectra of liquid Li from [41] along with the single particle Gaussian shape (red line) predicted by Eq. (9).

Acknowledgements

This work used resources of the National Synchrotron Light Source II, a U.S. Department of Energy (DOE) Office of Science User Facility operated for the DOE Office of Science by Brookhaven National Laboratory under contract no. DE-SC0012704.

Author details

Alessandro Cunsolo

Address all correspondence to: acunsolo@bnl.gov

National Synchrotron Light Source II, Brookhaven National Laboratory, Upton, NY, USA

References

[1] Brockhouse BN, Stewart AT. Scattering of neutrons by phonons in an aluminum single crystal. Physical Review. 1955; 100: 756–757. DOI: http://dx.doi.org/10.1103/PhysRev.100.756

[2] Burkel E. Phonon spectroscopy by inelastic X-ray scattering. Reports on Progress in Physics, 2000; 63: 171–232. DOI: http://dx.doi.org/10.1088/0034-4885/63/2/203

[3] Krisch M, Sette F. in Neutron and X-Ray Spectroscopy. Berlin: Springer-Verlag; 2007. pp. 317–370.

[4] Berne BJ, Pecora R. Dynamic Light Scattering. Mineola: Dover; 1976. 384 p.

[5] Lovesey SW. Theory of Neutron Scattering from Condensed Matter. Vol. 1. Oxford: Clarendon Press; 1984. 329 p.

[6] Sinha SK. Theory of inelastic X-ray scattering from condensed matter. Journal of Physics-Condensed Matter, 2001; 13: 7511–7523.

[7] Cunsolo A. Using X-ray as a probe of the terahertz dynamics of disordered systems —complementarity with inelastic neutron scattering and future perspectives. in Neutron Scattering, WA Monteiro, Editors. Rjeka: InTech; 2016.

[8] Jackson JD. Classical Electrodynamics. Vol. 3. New York: Wiley; 1962.

[9] Brillouin L. Diffusion of light and X-rays by a transparent homogeneous body. Annales de Physyque (Paris), 1922; 17: 88.

[10] Mason EA, Marrero TR. The diffusion of atoms and molecules, in Advances in Atomic and Molecular Physics, Bates DR, Immanuel E, Editors. Orlando: Academic Press; 1970. pp. 155–232.

[11] Hansen, JP, IMcDonald IR. Hydrodynamics and transport coefficients, in Theory of Simple Liquids (Third edition), Chapter 8. Burlington: Academic Press; 2006. pp. 219–254.

[12] Bafile U, Guarini E, Barocchi F. Collective acoustic modes as renormalized damped oscillators: unified description of neutron and X-ray scattering data from classical fluids. Physical Review E. 2006; 73: 061203 DOI: http://dx.doi.org/10.1103/PhysRevE.73.061203.

[13] Chen SH, et al. Co-operative modes of motion in simple liquids. Physics Letters. 1965; 19: 269–271. DOI: 10.1016/0031-9163(65)90980-7

[14] Kroô N, et al. International Atomic Energy Agency. Inelastic scattering of cold neutrons by condensed argon. in Symposium on Inelastic Scattering of Neutrons. Bombay: IAEA; 1964.

[15] Skold K, Larsson KE. Atomic motion in liquid argon. Physical Review. 1967; 161: 102–116.

[16] Randolph PD, Singwi KS. Slow-neutron scattering and collective motions in liquid lead. Physical Review. 1966; 152: 99–112.

[17] Rahman A. Propagation of density fluctuations in liquid rubidium: a molecular-dynamics study. Physical Review Letters. 1974; 32: 52–54.

[18] Bell HG, Kollmar A, Alefeld B, Springer T. Investigation of collective excitations in liquid neon by means of neutron-scattering at small scattering vectors. Physics Letters A. 1973; 45: 479–480. DOI: 10.1016/0375-9601(73)90717-2

[19] Bafile U, Verkerk P, Barocchi F, de Graaf LA, Suck JB, Mutka H. Onset of departure from linearized hydrodynamic behavior in argon gas studied with neutron Brillouin scattering. Physical Review Letters. 1990; 65: 2394–2397. DOI: http://dx.doi.org/10.1103/PhysRevLett.65.2394

[20] Allen MP, Tildesley DJ. Computer Simulation of Liquids. Oxford: Oxford University Press; 1989.

[21] Cunsolo A, Pratesi G, Ruocco G, Sampoli M, Sette F, Verbeni R, Barocchi F, Krisch M, Masciovecchio C, Nardone M. Dynamics of dense supercritical neon at the transition from hydrodynamical to single-particle regimes. Physical Review Letters. 1998; 80: 3515–3518. DOI: http://dx.doi.org/10.1103/PhysRevLett.80.3515

[22] Cunsolo A. Relaxation Phenomena in the THZ Dynamics of Simple Fluids Probed by Inelastic X Ray Scattering. Grenoble: Universite' J. Fourier; 1999.

[23] Egami T, Billinge SJ. Underneath the Bragg Peaks: Structural Analysis of Complex Materials. Vol. 16. Oxford: Elsevier; 2003.

[24] Cunsolo A, Pratesi G, Verbeni R, Colognesi D, Masciovecchio C, Monaco G, Ruocco G, Sette F. Microscopic relaxation in supercritical and liquid neon. Journal of Chemical Physics, 2001; 114: 2259–2267. DOI: http://dx.doi.org/10.1063/1.1334613

[25] Cunsolo A, Pratesi G, Rosica F, Ruocco G, Sampoli M, Sette F, Verbeni R, Barocchi F, Krisch M, Masciovecchio C, Nardone M. Is there any evidence of a positive sound dispersion in the high frequency dynamics of noble gases? Journal of Physics and Chemistry of Solids. 2000; 61: 477–483. DOI: http://dx.doi.org/10.1016/S0022-3697(99)00340-6

[26] De Gennes PG. Liquid dynamics and inelastic scattering of neutrons. Physica. 1959; 25: 825–839. DOI: 10.1016/0031-8914(59)90006-0

[27] Skold K. Small energy transfer scattering of cold neutrons from liquid argon. Physical Review Letters. 1967; 19: 1023–1025. DOI: http://dx.doi.org/10.1103/PhysRevLett.19.1023

[28] NIST. Thermodynamic data are from the database *http://webbook.nist.gov/chemistry/form-ser.html*.

[29] Castillo R, Castaneda S. The bulk viscosity in dense fluids. International Journal of Thermophysics. 1988; 9: 383–390. DOI: 10.1007/BF00513078

[30] Senesi R, Andreani C, Colognesi D, Cunsolo A, Nardone M. Deep-inelastic neutron scattering determination of the single-particle kinetic energy in solid and liquid 3He. Physical Review Letters. 2001; 86: 4584–4587. DOI: http://dx.doi.org/10.1103/PhysRevLett.86.4584

[31] Stringari, S, Pitaevskii L, Stamper-Kurn DM, Zambelli F. Momentum distribution of a bose condensed trapped gas, in Bose-Einstein Condensates and Atom Lasers, S Martellucci, et al., Editors. Boston: Springer; 2002. pp. 77–95.

[32] Silver RN, Sokol PE, Editors. Momentum Distributions. New York: Springer; 2013.

[33] Monaco G, et al. Deep inelastic atomic scattering of X rays in liquid neon. Physical Review Letters. 2002; 88: 227401. DOI: http://dx.doi.org/10.1103/PhysRevLett.88.227401

[34] Glyde HR. Momentum distributions and final-state effects in neutron scattering. Physical Review B. 1994; 50: 6726–6742. DOI: http://dx.doi.org/10.1103/PhysRevB.50.6726

[35] Izzo, MG, Bencivenga F, Cunsolo A, Di Fonzo S, Verbeni R, Gimenez De Lorenzo R. The single particle dynamics of iodine in the Sachs-Teller regime: an inelastic X ray scattering study. Journal of Chemical Physics. 2010; 133: 124514. DOI: 10.1063/1.3483689

[36] Cunsolo A, Monaco G, Nardone M, Pratesi G, Verbeni R. Transition from the collective to the single-particle regimes in a quantum fluid. Physical Review B. 2003; 67: 024507. DOI: http://dx.doi.org/10.1103/PhysRevB.67.024507 38

[37] Krieger TJ, Nelkin MS. Slow neutron scattering by molecules. Physical Review. 1957; 106: 290–295. DOI: http://dx.doi.org/10.1103/PhysRev.106.290

[38] Sachs RG, Teller E. The scattering of slow neutrons by molecular gases. Physical Review. 1941; 60: 18–27. DOI: http://dx.doi.org/10.1103/PhysRev.60.18

[39] Cai YQ, Coburn1 DS, Cunsolo A, Keister JW, Honnicke MG, Huang XR, Kodituwakku CN, Y Stetsko1, Suvorov A, Hiraoka N. The ultrahigh resolution IXS beamline of nsls-ii: recent advances and scientific opportunities. 11th International Conference on Synchrotron Radiation Instrumentation (Sri 2012), 2013; 425: 202001. DOI: http://dx.doi.org/10.1088/1742-6596/425/20/202001

[40] Fleury PA, Boon JP. Brillouin Scattering in Simple Liquids – Argon and Neon. Physical Review. 1969; 186:244–254. DOI: https://doi.org/10.1103/PhysRev.186.244

[41] Scopigno T, Balucani U, Cunsolo A, Masciovecchio C, Ruocco G, Sette F, Verbeni R. Phonon-like and single-particle dynamics in liquid lithium. Europhysics Letters. 2000; 50:189–195. DOI: 10.1209/epl/i2000-00253-5

Chapter 2

Grazing Incidence Small Angle X-Ray Scattering as a Tool for In-Situ Time-Resolved Studies

Gonzalo Santoro and Shun Yu

Additional information is available at the end of the chapter

http://dx.doi.org/10.5772/64877

Abstract

With the advent of third-generation synchrotron sources and the development of fast two-dimensional X-ray detectors, X-ray scattering has become an invaluable tool for in-situ time-resolved experiments. In the case of thin films, grazing incidence small angle X-ray scattering (GISAXS) constitutes a powerful technique to extract morphological information not only of the thin film surface but also of buried structures with statistical relevance. Thus, recently in-situ GISAXS experiments with subsecond time resolution have enabled investigating the self-assembly processes during vacuum deposition of metallic and organic thin films as well as the structural changes of polymer and colloidal thin films in the course of wet deposition. Moreover, processing of thin films has also been investigated in-situ employing GISAXS. In this chapter, we review the current trends of time-resolved GISAXS studies. After an introduction to the GISAXS technique, we present exemplary results of metallic and organic thin film preparation, wet deposition of polymer thin films and self-assembly of colloidal thin films, as well as examples of thin film modification in, e.g., microfluidic channels and within working devices. Finally, an overview of the future perspectives in the field is provided.

Keywords: GISAXS, thin films, time-resolved experiments, kinetics, processing

1. Introduction

Nanostructures have become commonly used in our daily lives because of the novel properties arising at the nanoscale. These are mainly associated to the object size offering a higher surface-to-volume ratio than macroscopic entities and, thus, surface processes become more

and more crucial as the material size is reduced. Furthermore, during the last half century several ways of manipulating the materials at the nanometer scale have been developed to control the nanostructure morphology on demand via either building up the nanostructures by atomic manipulation or exploiting self-assembly concepts. The latter presents clear advantages over atomic manipulation such as less demanding fabrication steps and easier scale-up for industrial production. Nevertheless, much is yet to be understood concerning self-assembly. In this sense, apart from the manipulation of materials at the nanoscale, an appropriate and accurate characterization of nanostructures is crucial, especially for studying the kinetics both during fabrication and processing of the nanostructures.

To properly characterize nanostructures, two questions need to bear in mind: what is the size/shape of the nanostructure and how do they separate from each other. The former is critical since nanostructure geometry strongly influences, e.g., the geometric confinement of the electronic structure [1], the catalytic activity [2, 3] or the optical properties [4, 5]. The latter is important since different physical properties may arise from particular nanostructure arrangement or in the space confined between the nanostructures, e.g., highly ordered arrays of plasmonic nanostructures present a collective plasmonic behavior [6], an efficient arrangement of the nano-objects may expose higher surface area on a macroscopic level for catalysis applications [7] or polymers within nanostructured media may show different glass transition temperatures and chain mobility due to confinement [8].

Within a non ideal material system, the size of the nanostructures and the spatial arrangement present a distribution over micro/macroscopic regions. Thus, the collective effects of nanostructured objects call for sound statistic evaluation. In this respect, grazing incidence small angle X-ray scattering (GISAXS) is nowadays one of the most interesting techniques for studying the morphology of nanostructured thin films. As its counterpart, transmission SAXS [9], it is sensitive to the size and shape of the nanoparticles and to the correlation distances between them, being capable of resolving objects and distances ranging from few nanometers to several hundreds of nanometers, in real space. In contrast to SAXS, GISAXS inherently presents high surface sensitivity as a consequence of the measurement geometry employed. In GISAXS, the incident X-ray beam impinges the sample at shallow angles, thus total external reflection on the surface may take place. In addition, this implies that the beam footprint on the sample probes macroscopic areas which, together with the nature of reciprocal space techniques, ensure that high sampling statistics is achieved.

GISAXS was first demonstrated by Levine et al. using a lab source [10]. However, the full potential of GISAXS is realized when a synchrotron is used as X-ray source. This is due to several reasons. First, a high photon flux is required to probe the surface structures, which may be only present in small amount in comparison to the bulk substrate, thus presenting a weak scattering signal; second, highly collimated beams are demanded to improve the reciprocal space resolution, thus the low emittance, small divergence, and partially coherent beams provided by synchrotron radiation sources are in great favor; third, synchrotron sources provide tunable X-ray wavelength, which may be used to probe the chemical composition in parallel to exploring the morphology.

http://dx.doi.org/10.5772/64877

The high X-ray photon flux of synchrotron sources extremely diminishes the acquisition time of a GISAXS pattern. This fact, along with a high flexibility in sample environments—e.g., vacuum chambers, liquid cells, heating stages, vapor exposure chambers, etc.—makes GISAXS a very powerful tool for acquiring morphological information on kinetic processes, which is extremely relevant to elucidate self-assembly processes. Additionally, the combination of parallel characterization techniques—e.g., optical spectroscopy and microscopy, electrical and magnetic characterization—allows correlating the structural information to the properties of the thin films, of utmost importance for tailoring the thin film functionality.

However, to carry out in-situ GISAXS, the high quality X-ray beam offered by synchrotron sources is not sufficient. The development of the 2D pixel detector, especially single photon counter, has played an important role. The high quantum efficiency and fast read-out time of 2D photon-counting pixel detectors can be translated to lower acquisition times—in comparison with CCD detectors; however, at present, CCD cameras offer small pixel size, implying higher resolution in reciprocal space. The low acquisition time renders a faster capture of the morphological features and the fast detector read-out time and efficiency enable high acquisition rates, thus it is possible to promptly track morphological development and/or modifications.

In this chapter, we will present the current trends of in-situ time-resolved GISAXS investigations during thin film preparation and processing. The chapter is structured as follows. Section 2 briefly introduces the GISAXS theory and analysis of GISAXS patterns. In Section 3, selected examples of in-situ GISAXS studies during the vacuum deposition of metals and organic thin films, as well as in-situ GISAXS investigations of wet deposition processes, are presented. Some exemplary studies of thin film processing and in-operando devices in which the use of in-situ GISAXS has resulted essential are compiled in Section 4. Finally, the conclusions and future perspectives of the field, according to the authors' opinion, are summarized in Section 5.

2. Grazing incidence small angle X-ray scattering

In this section, the basics of GISAXS will be shortly described. For more detailed information on the GISAXS theory, the readers are referred to [11–13].

2.1. Geometry, index of refraction and penetration depth

The main particularity of GISAXS lies on the geometry employed. Whereas in SAXS a transmission geometry is used, in GISAXS the X-ray beam impinges on the sample surface under a shallow incident angle, α_i, typically of tenths of a degree. The intensity scattered by the sample is then collected with a two-dimensional (2D) detector as a function of the exit, α_f, and out-of-plane, ψ, angles being the scattering plane that defined by the incident and specularly reflected X-rays. Typical sample-to-detector distances are in the range of 2–5 m and typical values of the scattering vector modulus q are 1–0.01 nm^{-1}, i.e., structures in the range of one to several hundred nanometer size in real space are probed by GISAXS.

The coordinate system usually selected in GISAXS presents the x-axis in the direction of the X-ray beam, the y-axis parallel to the sample surface and the z-axis along the surface normal.[1] The scattering geometry is depicted in **Figure 1**.

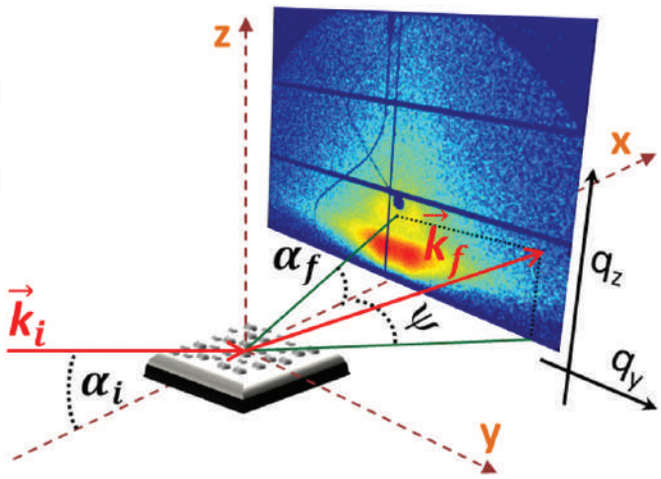

Figure 1. Sketch of the GISAXS scattering geometry. The sample is inclined by a small angle α_i with respect to the incoming X-ray beam and the diffuse scattering is recorded using a 2D detector as a function of the exit angles α_f and ψ. Typical sample-to-detector distances range from 2 to 5 m. Experimentally, the specular and the direct X-ray beams are commonly blocked by beamstops (the specular beamstop is the dark blue circle in the GISAXS pattern shown whereas the direct beamstop is not shown) to prevent the detector from oversaturation due to its strong intensity.

Within this coordinate system, the scattering vector, $\vec{q}$, i.e., the wave vector transfer due to the scattering event, in the case of monochromatic X-rays with an incident wave vector $\vec{k}_i$ and wave number $k_0 = 2\pi/\lambda$ scattered along the $\vec{k}_f$ direction is given by

$$\vec{q} = \vec{k}_f - \vec{k}_i = \begin{pmatrix} q_x \\ q_y \\ q_z \end{pmatrix} = \frac{2\pi}{\lambda} \begin{pmatrix} \cos(\alpha_f)\cos(\psi) - \cos(\alpha_i) \\ \cos(\alpha_f)\sin(\psi) \\ \sin(\alpha_i) + \sin(\alpha_f) \end{pmatrix} \quad (1)$$

Due to the small incident and exit angles involved in the GISAXS geometry a description of the sample based on a mean refractive index is sufficient and basically scattering arises from the variations in refractive index[2]

[1] For reasons out of our knowledge, the axes of the coordinate system commonly employed, and more often found in the literature, form an inverse trihedral angle—i.e., the axes are defined by the vector product $\hat{x} \times \hat{y} = -\hat{z}$, where, $\hat{x}$, $\hat{y}$ and $\hat{z}$ represent the axis unit vectors—instead of the usual direct trihedral angle. Anyway, since all the angles involved in GISAXS geometry are small, q_x is negligible (Eq. (1)) and this axis selection is not particularly relevant.

[2] Strictly, the responsible for the scattering events is the variation in electron density, which in a simplified manner is taken into account using a mean refractive index.

http://dx.doi.org/10.5772/64877

$$n(\lambda) = 1 - \delta(\lambda) + i\beta(\lambda) \tag{2}$$

where $\delta(\lambda)$ and $\beta(\lambda)$ represent the dispersion and absorption parts of X-rays, respectively, and are given by the following expressions:

$$\delta(\lambda) = \frac{r_e \lambda^2}{2\pi} \rho \frac{\Sigma_k [f_k^0(\lambda) + f'_k(\lambda)]}{\Sigma_k M_k} \tag{3}$$

$$\beta(\lambda) = \frac{r_e \lambda^2}{2\pi} \rho \frac{\Sigma_k f''_k(\lambda)}{\Sigma_k M_k} \tag{4}$$

in which $r_e = e^2/4\pi\varepsilon_0 m_e c^2$ is the classical electron radius, λ the wavelength, ρ the material mass density and M_k the atomic mass. f_k^0 is the nonresonant term of the atomic scattering factor and can be approximated by the number of electrons Z_k whereas f'_k and f''_k are the dispersion corrections. The summations are performed over all k atoms within the unit cell, molecule or, in the case of polymers, repeating unit.

Since diffuse scattering can be ascribed to changes in the refractive index any type of surface roughness or electronic contrast variation gives rise to diffuse scattering which contains the morphological information of the probed film.

On the other hand, in the case of X-rays the refractive index is less than unity, implying that total external reflection takes place for angles below the critical angle $\alpha_c(\lambda)$ of the material, which is given by

$$\alpha_c = \sqrt{2\delta} \tag{5}$$

The diffuse scattering at $\alpha_{i,f} = \alpha_c$ presents a maximum that is referred to as the Yoneda peak [14] and its position is dependent on the material[3], as is evident from Eqs. (3) and (5). The X-ray penetration depth varies from several nanometers, for incident angles below α_c, to several microns, for incident angles above α_c. In the ideal case of a perfectly flat film the penetration depth, Λ, defined as the depth at which the X-ray intensity is attenuated by 1/*e*, for α_i, $\alpha_c \ll 1$ and $\alpha_i = \alpha_f$ adopts the following expression[4] [16, 17]:

[3] Experimentally, the Yoneda peak is found at $\alpha_Y = \alpha_i + \alpha_c$ with respect to the direct beam on the detector, since it is the sample which is tilted whereas the incoming X-ray beam remains normal to the detector plane. At an angle α_i from the direct beam position the so-called sample horizon is found and the scattering below the sample horizon is mainly due to scattering through the sample, i.e., in transmission geometry, especially for angles well above the critical angle of the probed film. See [15].

[4] Actually, the depth probed in GISAXS depends on both the incident and exit angles since it is defined as the inverse of the imaginary part of q_z that presents a dependence on both angles. The probed depth is a combination of the penetration depth—incoming beam—and the depth from which scattering escapes the sample—exit beam. See [16, 17].

where β is the imaginary part of the refractive index. Thus, by varying the incident angle different film depths can be probed (**Figure 2**).

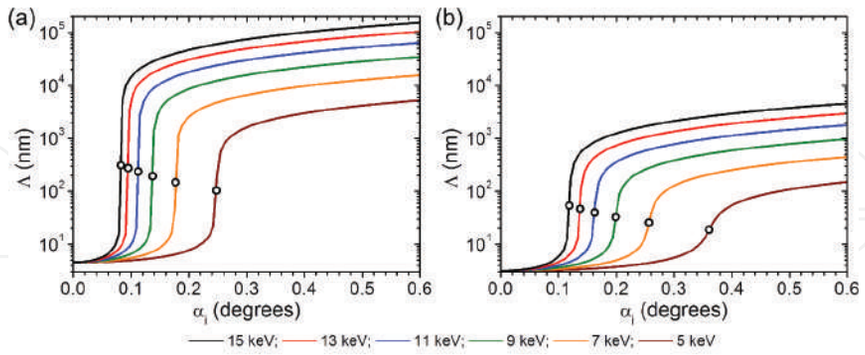

Figure 2. Penetration depth for α_i, $\alpha_c \ll 1$ and α_i, α_f as a function of the incident angle at different X-ray energies for (a) polystyrene (PS) and (b) Si. In (a), a mass density of 1.04 g/cm^3 has been assumed. The dots represent the penetration depth at α_c for each energy.

$$\Lambda = \frac{\lambda}{4\pi}\sqrt{\frac{2}{\sqrt{(\alpha_i^2 - \alpha_c^2)^2 + 4\beta^2} - (\alpha_i^2 - \alpha_c^2)}} \tag{6}$$

From the scattering geometry alone, two major advantages of GISAXS over standard microscopic techniques are easily inferred. First, due to the small incident angle used, scattering comes from all the illuminated area within the X-ray footprint—in the order of several mm even for microfocus GISAXS (μGISAXS), i.e., GISAXS performed with X-ray beam sizes of few tenths of microns or lower in both the horizontal and vertical directions—thus providing information of statistical relevance. Second, information not only from the surface but also from buried structures is accessible simply by tuning the incident angle of the X-ray beam with respect to the sample surface normal.

2.2. Scattering intensity: form factor and structure factor

The fact that GISAXS is performed at incident angles close to the critical angle implies that reflection on the surface can occur and thus multiple scattering effects take place. As a consequence the Born approximation (BA) is no longer valid and the diffuse scattering is typically analyzed within the framework of the distorted-wave Born approximation (DWBA) to account for reflection/refraction effects. Nevertheless, the basic concepts from the analysis of transmission scattering still apply, namely the use of a form factor and a structure factor. At present, several software packages are available for modeling of GISAXS data employing the DWBA [18–21].

In the simple BA, the form factor is the Fourier transform of the shape function of the scattering object

$$F(\vec{q}) = \int \exp(i\vec{q}\cdot\vec{r})d^3r \tag{7}$$

http://dx.doi.org/10.5772/64877

In the DWBA, for the case of a simple object located on a solid substrate, this form factor is replaced by the coherent sum of four terms to take into account different scattering events that involve the reflection of the incident or scattered X-ray beam on the substrate.[5] Thus, the form factor adopts the following expression

$$F_{DWBA}\left(\vec{q}_{\parallel},q_z\right)=F\left(\vec{q}_{\parallel},k_{z,f}-k_{z,i}\right)+R(\alpha_i)F\left(\vec{q}_{\parallel},k_{z,f}+k_{z,i}\right)+R\left(\alpha_f\right)F\left(\vec{q}_{\parallel},-k_{z,f}-k_{z,i}\right)$$
$$+R(\alpha_i)R\left(\alpha_f\right)F\left(\vec{q}_{\parallel},-k_{z,f}+k_{z,i}\right) \quad (8)$$

being $R(\alpha_i)$ and $R(\alpha_f)$ the Fresnel reflection coefficients of the substrate. These four terms are schematically represented in **Figure 3**.

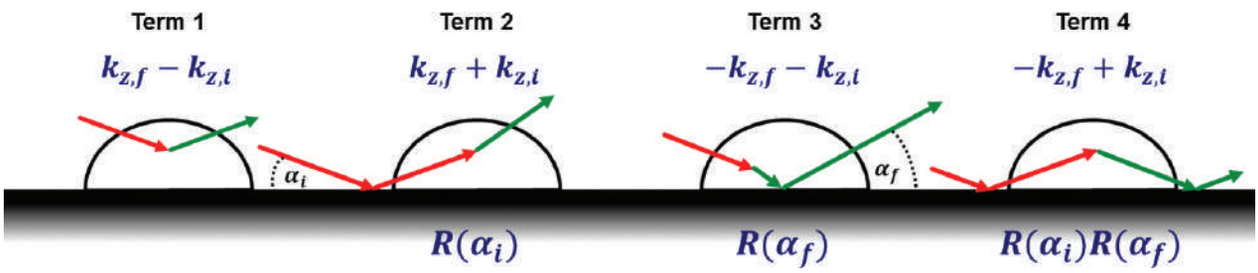

Figure 3. Schematic representation of the four terms involved in the scattering of a supported object on a solid substrate. The scattering event is represented by the color change of the arrows.

The first term is the simple BA and for $\alpha_{i,f} \gg \alpha_c$ Eq. (8) resembles the BA since $R(\alpha_i) = R(\alpha_f) = 0$. In this case—where the BA is valid and reflection/refraction effects can be neglected—the so-called effective layer approximation can be used and the differential cross-section for diffuse scattering can be written as [24, 25]:

$$\frac{d\sigma}{d\Omega}|_{diff}=\frac{C\pi^2}{\lambda 4}(1-n^2)\,|T_i|^2|T_f|^2\,P(\vec{q})\propto P(\vec{q}) \quad (9)$$

where C is the illuminated surface area, λ the wavelength, $T_{i,f}$ the Fresnel transmission functions and $P(\vec{q})$ is the diffuse scattering factor. Within this simplification, the diffuse scattering factor can be expressed in terms of the product of a form factor $F(\vec{q})$ of individual scattering objects and a structure factor $S(\vec{q}_{||})$ that accounts for the spatial arrangement of the scattering objects on the substrate surface and the interference between individual scattering events.[6] The structure factor is the Fourier transform of the so-called pair correlation

[5] In the more general case, transmission has to be taken into account and the Fresnel transmission coefficients appear also in the expression of the form factor. See, e.g., [22, 23].

[6] For this reason, the structure factor, $S(\vec{q}_{||})$, is also often called interference function.

function $g(r)$ that describes the spatial arrangement of scattering entities in real space and several ad hoc pair correlation functions can be used to analyze the GISAXS data.[7] The diffuse scattered intensity $I(\vec{q})$ for a lateral electron density fluctuation on the surface can be then expressed as

$$I(\vec{q}) \propto \langle | F_{DWBA}(\vec{q}) |^2 \rangle S(\vec{q}_{\parallel}) \tag{10}$$

In highly diluted systems $S(\vec{q}_{||})$ tends to 1 since there is no interference between the scattered photons. In these cases, the scattering pattern—being only proportional to $F(\vec{q})$ reflects the shape of the scattering objects. Opposite, in the case of concentrated systems $F(\vec{q})$ and $S(\vec{q}_{||})$ are strongly correlated.

2.3. Coupling of form and structure factors: approximations

Although sometimes useful for the analysis of horizontal line cuts—i.e., the intensity distribution as a function of q_y at constant q_z extracted from the 2D scattering pattern—the expression derived for the diffuse scattering intensity in the previous section (Eq. (10)) is a crude simplification since small angle scattering is comprised of a coherent term, which is the product of the form factor and structure factor, and an incoherent one that appears as a consequence of polydispersity in the size distribution of the scattering objects. The incoherent term weaves the form and structure factors and is very difficult to evaluate analytically, thus several approximations have been developed to consider the correlation between the scattering objects and their spatial positions.

The simplest one is the so called decoupling approximation (DA) that assumes that there is no correlation between the kind of scattering object and its position. This approximation is usually applied when the size polydispersity is small or the surface density of scattering entities is low (**Figure 4(a)**).

Opposite to DA, when the polydispersity is high, a full correlation of the size of the scattering object and its position is assumed in the local monodisperse approximation (LMA). LMA considers that within the coherence length of the X-ray beam neighboring objects present the same size and shape, i.e., the polydisperse scattering objects are clustered in monodisperse domains whose scattering intensities are incoherently summed up (**Figure 4(b)**).

In between these extreme cases, the size-spacing correlation approximation (SSCA) [26] was developed to account for more realistic correlations between the size and separation of the scattering entities. Its formalism is derived from the paracrystal theory and introduces a partial correlation of sizes and positions in a probabilistic way. Shortly, within the SSCA, given a scattering object of distinct size and position and a description of the size polydispersity by a

[7] Some of the more commonly applied are the Debye hard core interference function, the Gaussian pair correlation function, the gate-pair correlation function, the Lennard-Jones pair correlation function, etc. See [12] and references therein.

http://dx.doi.org/10.5772/64877

statistical function, the probability of finding neighboring objects of particular size and positions with respect to the first scattering object is obtained, considering a particular probability distribution. Thus, both size-dispersion and position disorder are propagated statistically along the arrangement of scattering entities and long-range order is gradually destroyed in a probabilistic way (**Figure 4(c)**).

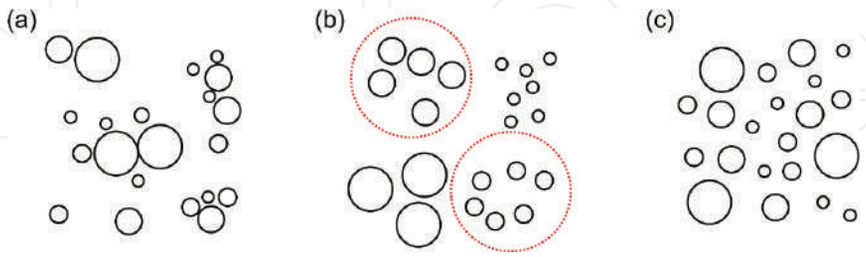

Figure 4. Schematic representation of the size-space correlation of scattering entities within (a) the decoupling approximation (DA), (b) the local monodisperse approximation (LMA), and (c) the size-spacing correlation approximation (SSCA). In (b), the red dotted circles represent the coherent X-ray domains.

3. In-situ GISAXS during deposition processes

During the last decade or so, GISAXS has been established as a very powerful technique to reveal the kinetics of deposition processes for thin film preparation employing different approaches. In particular, GISAXS is strongly contributing to reveal the mechanism of thin film growth and self-assembly both for vacuum and wet deposition processes that are relevant not only from a fundamental point of view but also for technological development. GISAXS presents two decisive advantages over standard microscopic techniques for the investigation of the growth kinetics and self-assembly: first, it provides averaged information over a large sample area—the beam footprint on the sample—thus the information acquired is of statistical significance; second, time resolutions down to several milliseconds are accessible due to the high X-ray intensities offered by third-generation synchrotron sources and the development of fast 2D X-ray detectors, thus fast kinetic processes can be studied.

In this section, exemplary results will be presented illustrating the strong capabilities of in-situ time-resolved GISAXS for the investigation of the stages governing the kinetics of thin film growth and self-assembly, both phenomena of high importance to gain control over the processes so as to tune the thin film properties to the required functionality.

3.1. Vacuum deposition of nanostructured metallic thin films

Vacuum deposition of nanostructured metallic films constitutes a very important technological and research field with applications ranging from coatings for antibacterial activity and catalysis to plasmonics, optoelectronics and sensors. In most cases, the morphology is closely related to the functionality of the film. Therefore, it is extremely important to achieve a deep

understanding of the growth mechanism and morphological development of the nanostructures so as to allow for tailoring the nanostructured metallic thin film to the desired application.

In order to investigate in-situ vacuum deposition processes using GISAXS, deposition chambers have been specifically designed to be installed at synchrotron beamlines [27–29]. In addition, a growing amount of systems have been investigated during the last years—some examples can be found in [30–33] —from which, in the following, only some selected results will be discussed.

In-situ μGISAXS has been applied to study the sputter deposition process of both Au and Ag on SiO_x with time resolutions of 15 and 100 ms, respectively [34, 35]. The growth kinetics of these two systems has been probed to proceed in a similar way and in-situ μGISAXS has contributed to elucidate the growth regimes and the associated kinetic thresholds of the systems. The analysis of the temporal evolution of the main scattering features – namely the position and full-width-at-half-maximum (FWHM) of the out-of-plane scattering peak (line cuts of the 2D scattering pattern along q_y at constant q_z) together with the evolution of the scattering profile of the so-called detector cuts and off-detector cuts (line cuts of the 2D scattering pattern along q_z at $q_y = 0$ and at constant $q_y \neq 0$, respectively) —led to identify four different growth stages dominating the morphological development of Au and Ag thin films, from the nucleation phase to the formation of a complete layer (**Figure 5**).

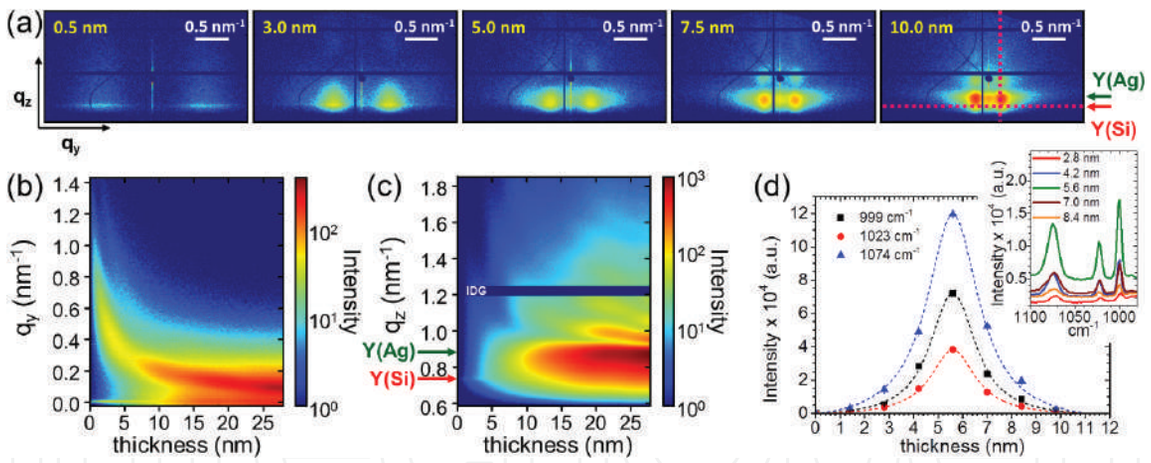

Figure 5. (a) Selected 2D μGISAXS patterns during sputter deposition of Ag on SiO_x. The deposition process was continuously monitored with a time resolution of 100 ms. The effective film thickness is indicated in each GISAXS pattern. The dotted lines on the right pattern mark the positions where line cuts were performed to evaluate the data. (b) Out-of-plane (along q_y) line cuts versus sputtered thickness at the Si Yoneda peak ($q_{z,c}$(Si; 13 keV) = 0.733 nm^{-1}). The evolution of the out-of-plane scattering peak from large q_y toward lower values is related to an increase in the mean distance between Ag nanoclusters as a consequence of the increase in clusters size. When the percolation threshold is reached, the peak gets arrested at a nearly constant value. A quantitative analysis of the mean distance D between nanoclusters can be performed from the peak maximum applying $q_y \approx 2\pi/D$. (c) Off-detector (along q_z) line cuts versus sputtered thickness at q_y = 0.112 nm^{-1}. As the deposition proceeds, the maximum intensity changes from the Si Yoneda peak to the Ag Yoneda peak and vertical modulations related to the formation of Ag layers appear. (d) Intensity of the characteristic SERS bands of thiophenol shown in the inset for different Ag thickness. The dashed lines are Voigt fittings to the data. IDG: intermodule detector gap. Y(Si): Si Yoneda peak. Y(Ag): Ag Yoneda peak. Adapted with permission from Santoro et al. [35] with the permission of AIP Publishing.

http://dx.doi.org/10.5772/64877

The growth kinetics of Au during sputter deposition, apart from being of industrial and technological relevance, is of significant importance from a basic point of view. To simulate the complete 2D μGISAXS patterns along the deposition process, a geometrical model based on the 2D hexagonal paracrystalline arrangement of hemispherical clusters was developed [34] allowing for extracting important parameters such as the surface coverage, film porosity or cluster density, thus enabling to predict morphology-dependent properties of the thin film such as the optoelectronic response.

Since the growth of Ag on SiO_x proceeds in a similar manner, the geometrical model proposed by Schwartzkopf et al. [34] has been also successfully applied to the deposition of nanostructured Ag thin films on SiO_x for surface enhanced Raman spectroscopy (SERS) (**Figure 5**(d)) [35]. A key point in SERS, whose underlying main mechanism is the enormous enhancement of the local electromagnetic field in the vicinity of nanostructured noble metal surfaces due to localized surface plasmons, is the gap between nanostructures. At the nanostructure gaps—the so-called "hot-spots" —the electromagnetic enhancement is maximum. In this case, in-situ μGISAXS during sputter deposition of Ag allowed not only identifying the main growth regimes and thresholds but also to correlate the developed morphology to the SERS activity. By modeling the full 2D μGISAXS patterns within the DWBA and the SSCA, a maximum SERS enhancement was found for a mean gap of 1 nm between Ag nanoclusters, corresponding to an effective film thickness of 5.6 nm.

On the other hand, the deposition kinetics of Au on a quasi-regular hexagonal array of self-assembled cadmium selenide (CdSe) quantum dots has also been investigated by in-situ μGISAXS [36]. Opposite to the growth of Au and Ag on SiO_x, in the early deposition stage the out-of-plane peak did not change in position but remained fairly constant. The deposition of Au only led to an increase in electronic contrast, thus, of the diffuse scattering intensity produced by the underlying array of CdSe quantum dots. This implies that the quantum dots act as nucleation sites for Au growth. Subsequently, lateral growth and coalescence of Au/CdSe-dot clusters were observed forming a compact Au/CdSe-dot layer. Finally, Au growth proceeded in the surface normal direction developing a capping layer on the CdSe quantum dots array.

In-situ GISAXS has also contributed to shed light on an intriguing issue during the growth of metallic thin films, namely the influence of the chemical affinity between the metal and the substrate on the deposition kinetics and thin film morphology. This is highly important in the case of, e.g., the deposition of metallic electrodes on organic solar cells or light emitting diodes where, in some cases, the electrodes represent the limiting factor in device performance. The great capabilities of in-situ GISAXS studies for this purpose has been demonstrated during the sputter deposition of Al and Ag on tris(8-hydroxyquinolinato)aluminum (Alq3), a key material in organic light emitting diodes. Alq3 presents a strong chemical interaction with Al whereas it interacts weakly with Ag, which translates into different growth mechanisms. In the case of Al deposition, three different stages of growth were identified and modeling of the 2D patterns revealed the formation of Al nanopillars after diffusion of Al in Alq3 and subsequent metal complex agglomeration [37]. On the other hand, without diffusing into the Alq3 thin film, Ag presents a morphological transition from truncated sphere clusters to cylindrical nanostruc-

tures upon surpassing the Ag percolation threshold at an effective film thickness of 5.0 nm (**Figure 6**), which was attributed to the different Ag-Ag and Ag-Alq3 interactions [38].

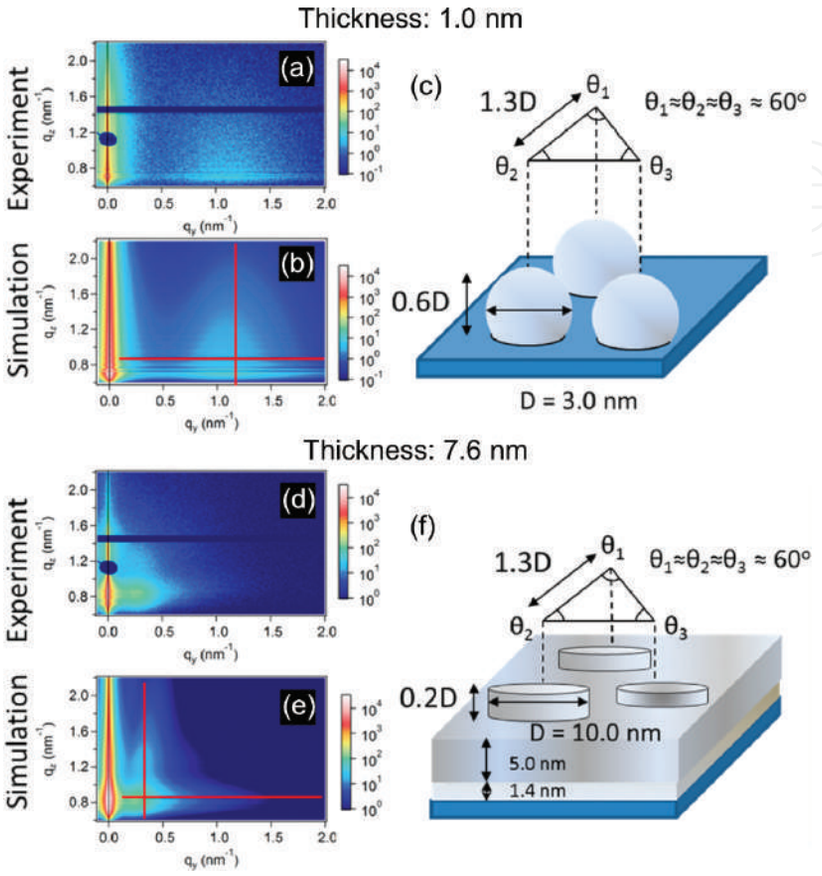

Figure 6. Morphological transition in cluster shape upon surpassing the percolation threshold (effective film thickness of 5.0 nm) during sputter deposition of Ag on a 36.0 nm thick Alq3 film. (a–c) Experimental 2D μGISAXS pattern, simulated 2D μGISAXS pattern and geometrical model used to simulate the data, respectively, at an effective Ag film thickness of 1.0 nm. (d-f) Experimental 2D μGISAXS pattern, simulated 2D μGISAXS pattern and geometrical model used to simulate the data, respectively, at an effective Ag film thickness of 7.6 nm. In both cases, the DWBA and the LMA were employed to simulate the scattering patterns. Adapted and reprinted with permission from Yu et al. [38]. Copyright 2015 American Chemical Society.

The differences in metal interaction and nanocluster diffusion coefficient on different materials can be exploited to tailor the thin film morphology. In this sense, an interesting approach consists in employing polymer thin films as templates in the nanoscale, given the known ability of block copolymers to spontaneously form nanostructures due to phase segregation. In general, when employing vacuum deposition of metals on organic thin films, in a first deposition stage, the metal diffuse into the film which influences the subsequent growth kinetics and, in the case of block copolymers, a selective wetting of the metal on one of the domains is commonly observed, which is ascribed not only to the different metal-polymer interaction but also to the differences in metal diffusion in each of the blocks. From in-situ μGISAXS measurements, the surface diffusion coefficient of Au on polystyrene (PS) has been extracted and a correlation of the developed Au morphology with the optical properties of the

film could be achieved by combining μGISAXS with real-time UV-Vis spectroscopic measurements during the growth [39].

On the other hand, Metwalli et al. [40] have taken advantage of the selective wetting of Co on spontaneously nanostructured polystyrene-block-poly(ethylene oxide) (PS-b-PEO) to prepare ordered Co nanoclusters along highly oriented PS domains. The morphology of the polymer thin film consisted of alternating highly oriented crystalline PEO and PS domains with a periodicity of around 30 nm and the in-situ GISAXS experiments demonstrated that selective wetting occurred below the Co thin film percolation threshold. They also elucidated the growth kinetics of Co on the block co-polymer nanostructured template.

A thorough study on the nanostructure development of transition metals on a PS-b-PEO template has also been recently reported [41]. It has been clearly revealed that the growth of Au, as a fairly inert element, was not influenced by the template, whereas Ag demonstrated slightly improved wetting on the PS domain, forming clusters. In the case of reactive metals, e.g., Fe, Ni, and Pt, well-defined and uniform nanocluster patterns were grown selectively on the PS domains. Additionally, by performing in-situ GISAXS experiments, it has been found that the substrate temperature plays an important role in shaping the metal clusters, showing that above the glass transition temperature, T_g, of PS, Ag clusters become more irregular. In addition, for Fe, flat nanodots with a low surface-to-volume ratio morphology were grown at substrate temperatures above T_g whereas a higher surface-to-volume ratio morphology is obtained for a substrate at room temperature during deposition. This is ascribed to the changes in diffusion coefficient with temperature, so that above T_g a higher diffusion coefficient of metal atoms and clusters during the deposition led to a lower surface-to-volume ratio cluster morphology.

The complicated growth kinetics of hierarchical anisotropic gold nanostructures on polystyrene-block-poly(methyl methacrylate) (PS-b-PMMA) thin films has been also studied with in-situ GISAXS [42]. An anisotropic shape of the deposited metal clusters was achieved by employing a glancing angle deposition (GLAD) geometry. In GLAD, the deposition plume is positioned at an oblique angle regarding the sample surface, which produced nonsymmetric Au clusters and its anisotropic shape manifested as nonsymmetric 2D scattering patterns with respect to the scattering plane ($q_y = 0$). In addition, a hierarchical ordering of the anisotropic Au was achieved benefiting from the selective wetting of Au on the PS domains. The anisotropy of this hierarchical nanostructure was also reflected in the anisotropic optical response of the system.

3.2. Vacuum deposition of organic thin films

Organic thin films are especially important since they are increasingly used in devices. In particular, organic semiconductors are employed in organic light emitting diodes (OLEDs), organic field-effect transistors (OFETs), and organic solar cells (OSCs). However, the basic processes of molecular thin film growth are still far from being understood and connecting molecular and nanoscopic/microscopic processes such as molecular diffusion and island size evolution, remains a major challenge. To this purpose in-situ GISAXS, being a non-invasive technique, is increasingly contributing.

As in the case of vacuum deposition of metals, several organic deposition chambers have been designed and built so as to perform in-situ X-ray scattering and/or diffraction measurements at synchrotron beamlines [43, 44].

To study these particular systems, in-situ grazing incidence X-ray diffraction (GIXD) and in-situ X-ray reflectivity (XRR) are most commonly applied [45–48], though the information provided by in-situ GISAXS is also very valuable since the dimensions probed are different. Whereas GIXD provides access to the crystal structure and molecular arrangement, GISAXS gives complementary information on the island shape and island-island distances as well as on the island electron density. Therefore, the combination of both techniques provides the necessary information to make a link between the molecular and micrometer size crystallite regimes.

These systems are usually investigated in the so called anti-Bragg geometry, i.e., at incident angles so that the specular peak corresponds to the anti-Bragg point of a given (*h k l*) permitted Bragg reflection of the molecular crystalline structure. The anti-Bragg points correspond to $|\vec{q}_{\text{anti-Bragg}}| = \frac{1}{2}|\vec{q}_{\text{Bragg}}|$ and are especially surface sensitive[8] [17]. From a practical point of view, for a selected (*h k l*) Bragg reflection, α_i is chosen so that at $\alpha_i = \alpha_f$ and $\psi = 0$ − i.e., the specular peak position—the following relationship is satisfied

$$q_z = \frac{2\pi}{\lambda}(\sin(\alpha_i) + \sin(\alpha_f)) = \frac{4\pi}{\lambda}\sin(\alpha_i) = \frac{1}{2}|\vec{q}_{Bragg}| \tag{11}$$

Note that in Eq. (11) only q_z is involved since for specular reflection $q_x = q_y = 0$ (Eq. (1)).

At this particular geometry, the specular intensity presents an oscillatory behavior during the growth—the so-called growth oscillations—which arises from destructive interference between neighboring odd and even monolayers (MLs) —lattice planes—so that the scattering from the first, third, fifth ML is cancelled by the growth of the second, fourth, sixth ML, etc. [49]. In the common case of (initial) layer-by-layer growth in organic heteroepitaxy, the periodicity of the oscillations consists in 2 MLs although interference between reflections at the growing surface, the substrate and the interfaces between different film layers can lead to more complex oscillatory behavior.[9] Through correct modeling of the growth oscillations, more complicated epitaxy growth models can be derived making assumptions about the intralayer and interlayer diffusion [50]. Therefore, additional information for the refinement of these models is very useful and can be obtained by performing GISAXS at the anti-Bragg geometry, which allows concurrently following the changes in the specular intensity—the growth oscillations—and the diffuse scattering [51–54].

[8] An introduction to surface X-ray diffraction, including the evanescent wave method that corresponds to GIXD, can be found in [17].

[9] For instance, considering an out-of-phase reflection on the substrate, the oscillations maxima appear at even instead of at odd numbers since an additional reflection occurs or, e.g., the oscillations period can change to 1 ML in the case of homoepitaxy. See [49].

http://dx.doi.org/10.5772/64877

The abovementioned geometry has been applied to investigate, e.g., the growth of multilayers of fullerene C_{60} molecules on mica in real time [55]. From the growth oscillations, a layer-by-layer growth was deduced whereas from the in-situ μGISAXS data the mean island distance was extracted and converted into surface island density assuming a hexagonal island arrangement. Interestingly, the GISAXS out-of-plane peaks present intensity oscillations with a period of 1 ML, in contrast to the 2 ML period of the specular intensity at the anti-Bragg point (**Figure 7**). This is due to the fact that diffuse scattering occurs only for uncomplete layers since this is the situation where a lateral variation in electron density—or, in other words, in refractive index—is present, whereas the growth oscillations are due to interference from the reflections at layer interfaces—plus at the substrate and at the growing layer—i.e., diffuse scattering is probing lateral contrast whereas the specular peak probes the structures in the surface normal direction. Through kinetic Monte Carlo simulations and a comparison to the experiments, values of the energy barriers were obtained—namely, the diffusion barrier and lateral binging energy for intralayer events and an Ehrlich-Schwoebel barrier for interlayer diffusion—and, more importantly, this set of parameters was demonstrated to be sufficient to describe the growth of a C_{60} layer on underlying C_{60} layers, of crucial importance so as to predict the growth dependence on the deposition rate and substrate temperature.

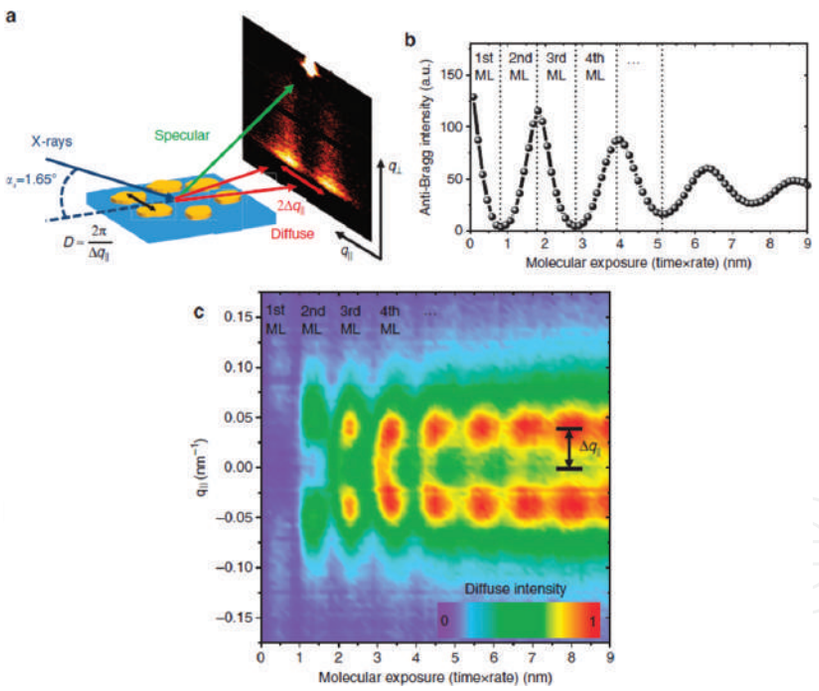

Figure 7. (a) Scattering geometry employed showing the simultaneous acquisition of specular and diffuse scattering. The incident angle is chosen so that the specular peak corresponds to the anti-Bragg position of the C_{60} (1 1 1) reflection. (b) Intensity at the anti-Bragg point $q_z = 0.38$ Å^{-1} as a function of the molecular exposure during the film growth. A damping of the growth oscillations from the third monolayer on is due to surface roughening since an imperfect layer-by-layer growth for high number of MLs occurs, providing a measurement of the roughening onset. (c) Oscillations of the out-of-plane GISAXS intensity as a function of the molecular exposure. From the out-of-plane peak position, the mean island distance can be extracted by $q_y \approx 2\pi/D$. © 2014 S. Bommel, N. Kleppmann, C. Weber, H. Spranger, P. Schäfer, J. Novak, S.V. Roth, F. Schreiber, S.H.L. Klapp and S. Kowarik. Adapted with permission from Bommel et al. [55]; originally published under Creative Commons Attribution 4.0 License. Available from: 10.1038/ncomms6388.

The simultaneous acquisition of the specular intensity and GISAXS signal has also been applied to in-situ investigate the molecular diffusion and island evolution during the growth of diindenoperylene (DIP, $C_{32}H_{16}$) on SiO_x [56]. Opposite to the C_{60} molecule, DIP presents shape anisotropy imposing additional degrees of freedom—tilting and bending—which increases the complexity of the growth process. In this case, above a surface coverage of 3 MLs the GISAXS out-of-plane peak oscillations vanished and the peak position remained constant, meaning a constant island center-to-center distance. This is a clear signature of a transition between a layer-by-layer to a three dimensional (3D) growth, i.e., formation of molecular islands with a fixed surface island density. Additionally, effective activation energies for island nucleation of DIP on SiO_x and of DIP on DIP could be extracted from the mean island diameter —derived from the diffuse scattering peak position—at 0.5 ML and 1.5 ML surface coverage, respectively, by varying the deposition substrate temperature.

Another organic semiconductor with rod-like morphology whose growth has been in-situ investigated performing GISAXS using the anti-Bragg geometry is *N*,*N*'-dioctyl-3,4,9,10-perylene tetracarboxylic diimide (PTCDI-C_8, $C_{40}H_{42}N_2O_4$) [57]. It has been shown that PTCDI-C_8, as is the case for DIP, underwent a transition from a layer-by-layer growth to a 3D growth but in a smoother fashion. This manifested both as a slow increase in the mean roughness of the completed MLs—derived from the growth oscillations—as well as in a smooth leveling off of the island density—derived from the out-of-plane GISAXS peak position by assuming a hexagonal arrangement of islands. Moreover, the island density extracted from the diffuse scattering at different substrate temperatures, allowed demonstrating higher molecular mobility of PTCDI-C_8 on PTCDI-C_8 than that of PTCDI-C_8 on SiO_x, which is responsible for the decreased island density observed in upper MLs.

3.3. Wet deposition of polymer and colloidal thin films

Wet deposition encompasses a collection of different methods for the fabrication of thin solid films from a liquid solution and/or suspension as precursor. All of them exploit self-assembly concepts to prepare thin films such as colloidal crystals, thin polymer films and nanocomposites with applications ranging from photonic crystals to polymer solar cells and superhydrophobic or superhydrophilic coatings. During wet deposition, the interaction between the suspended particles—or the dissolved compounds—together with the liquid flow—responsible of internal mass transport—govern the drying kinetics and self-assembly. Hence, tuning these parameters makes it possible to control the self-assembly, thus adjusting the morphology of the dried thin film (ideally) on demand.

Grazing incidence X-ray scattering (GIXS) techniques has been applied to study wet deposition processes such as solution casting [58, 59], spin-coating [60], dip-coating [61, 62], and blade coating [63]. Nevertheless, although these deposition methods are very useful for device fabrication at research scale, they are not easily scaled-up and/or they are restricted to specific substrate geometries. In this sense, it is important to explore other wet deposition methods of potential industrial relevance.

In recent years, spray coating is gaining interest due to its easy scale-up and integration into production lines as well as to its lack of substrate geometry/size constrains. Moreover, it has

http://dx.doi.org/10.5772/64877

already been successfully applied to fabricate operating devices such as polymer solar cells [64–66]. Nevertheless, although there are evident similarities to, e.g., solution casting, the drying kinetics present some particularities still not well understood. To this respect, GISAXS has been used to study the self-assemble of colloidal particles during spray coating [65, 67, 68]. In particular, Herzog et al. [67] were able to identify three different stages during the spray deposition of polystyrene (PS) nanoparticles and subsequent drying corresponding to the formation of a structureless thin liquid film, which subsequently breaks up into small droplets allowing for possible transient nanoparticle ordering and a final freezing of a self-assembled colloidal nanostructure once the solvent is fully evaporated, respectively. These three stages were revealed in the in-situ μGISAXS patterns as first, a decrease in the overall scattered intensity due to the homogeneous liquid film right after a 100 ms spray shot; second, an increase and broadening of the Yoneda peak ascribed to the homogeneity loss of the liquid film that breaks into small droplets as the solvent evaporation proceeds and last, the emergence of well-defined out-of-plane symmetric peaks regarding the scattering plane (**Figure 8**). In addition, controlling the evaporation rate by adjusting the substrate temperature the assembly process of the nanocolloids can be managed to achieve different film morphologies, what has been investigated in-situ by μGISAXS as well [68].

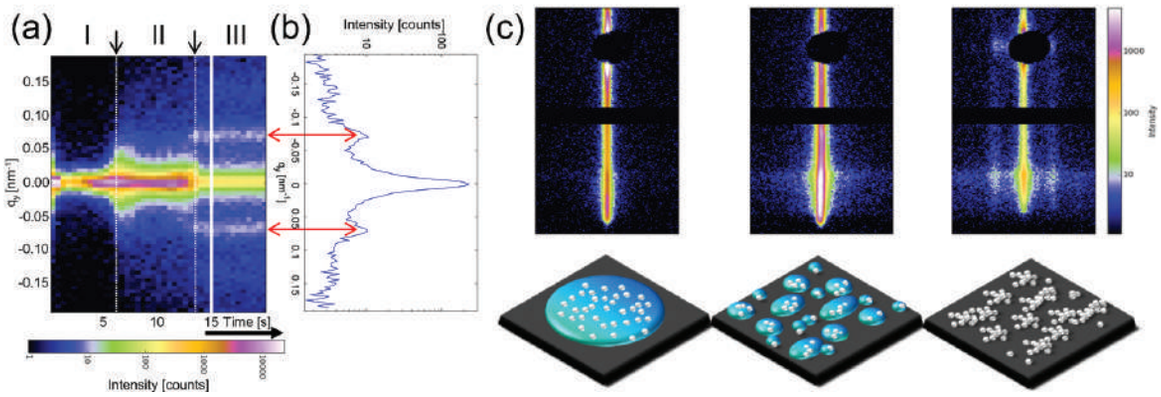

Figure 8. (a) Out-of-plane cuts (along q_y) at the Si Yoneda peak ($q_{z,c}$(Si; 13 keV) = 0.733 nm^{-1}) as a function of time during spray deposition of PS nanoparticles with a nominal diameter of 100 nm. The vertical dotted lines indicate the transitions between drying stages. (b) Individual out-of-plane cut of the dried sample at 15 s after spray deposition displaying side maxima corresponding to the most prominent lateral length scale of ≈ 90 nm. (c) Representative 2D GISAXS patterns of each of the three identified drying stages. Below each pattern a sketch of the corresponding drying stage in real-space is depicted. Reprinted (adapted) with permission from Herzog et al. [67]. Copyright 2013 American Chemical Society.

Apart from spray coating, another interesting approach for large scale low-cost production of organic photovoltaic (OPV) devices is inkjet printing, a method that has drawn considerable attention from an industrial point of view as the field of organic flexible electronics is maturing. As in the case of spray coating, GIXS has been applied to in-situ investigate the structure development during inkjet printing of, e.g., conductive polymer thin films widely used as electrodes in OPV devices [69] as well as of the active layer in bulk-heterojunction (BHJ) polymer solar cells [70]. The film morphology in OPV devices has a direct relationship with its performance and the combination of in-situ wide- and small angle scattering (GIWAXS/

GISAXS) allowed developing qualitative models of the structural evolution of the semicrystalline polymer thin films morphology.

Finally, although it does not present the current large-scale production promises of spray coating and inkjet printing, an interesting approach for wet deposition consist in employing microfluidics, which may be critical for lab-on-chip applications. Here, the peculiarity lies in the nondrying nature of the deposition, i.e., the self-assembly process on the substrate does not take place during solvent evaporation but at the liquid-solid interface during liquid flow. In order to in-situ follow deposition processes using microfluidics by GISAXS—among others; see Section 4—special flow cells have been designed [71]. In this kind of experiments, it is extremely important to adjust the X-ray beam footprint on the substrate to the size of the fluidic channel so as to prevent an overillumination of the sample not in contact with the fluid, thus minimizing undesired signal that could obscure the accessible information. Therefore, the use of μGISAXS becomes essential [72]. This specific setup has been used to investigate the attachment of Au nanoparticles to a polymer thin film (**Figure 9**) and different stages could be identified, namely the dried polymer film before the liquid inlet was opened (denoted as 1 in **Figure 9**), a wetted film by the liquid vapor once the liquid inlet was opened (denoted as 2 in **Figure 9**) and the attachment of Au nanoparticles once the liquid flow reached the probed thin film position (denoted as 3 in **Figure 9**). Moreover, the increase in intensity of the out-of-plane peak as the experiment proceeded indicated a cumulative deposition of the Au nanoparticles from which it is possible to analyze the deposition kinetics.

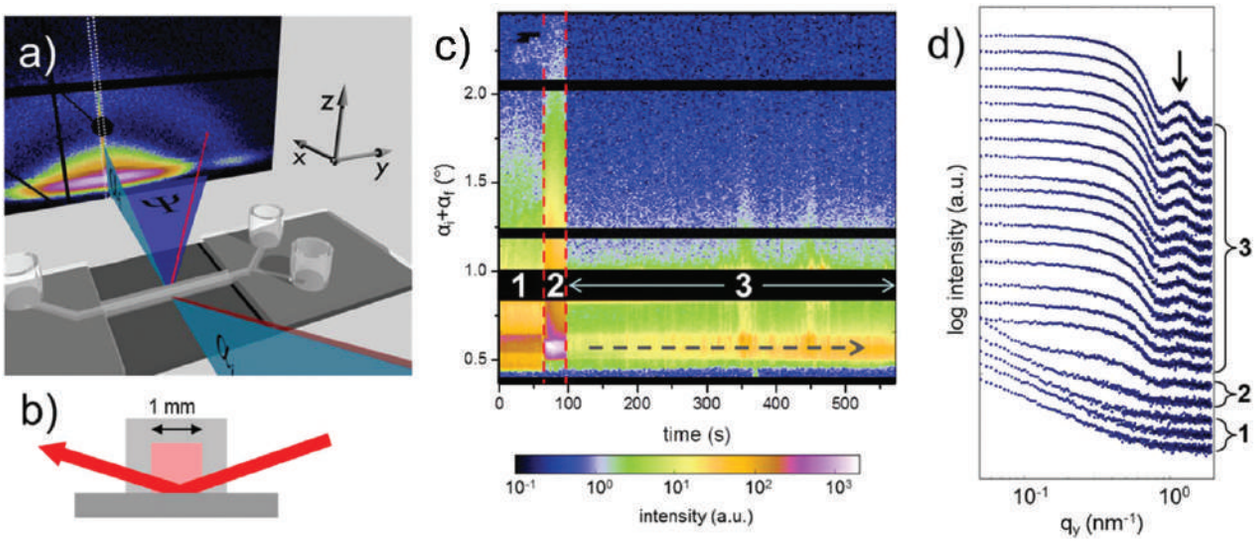

Figure 9. (a) Sketch of the μGISAXS setup with microfluidic cell. (b) Illustration of the X-ray beam transmitting the channel walls and the footprint on the sample surface. For clarity the incident angle and X-ray beam size are not in scale. (c) Detector cuts (along q_z at q_y = 0) as a function of time while 10 nm diameter Au nanoparticles attach to a poly(ethyleneimine) (PEI) thin film on a SiO_x substrate. Black regions correspond to the specular beamstop and the intermodule detector gaps. (d) Out-of-plane cuts (along q_y) at the Si Yoneda peak ($q_{z,c}$(Si; 13 keV) = 0.733 nm^{-1}) as sum of 10 consecutive measurements. The curves are vertically shifted for clarity. The numbers denote the deposition stages. Reprinted from Santoro et al. [72], with the permission of AIP Publishing.

http://dx.doi.org/10.5772/64877

4. In-situ GISAXS during thin film processing

In addition to the aforementioned deposition processes, a different kind of studies in which in-situ GIXS is increasingly contributing consist in thin film processing. GIXS has been performed during thin film nanostructuring in order to gain insight into the morphology transformation processes, e.g., metal nanocluster formation through high temperature annealing induced dewetting [73, 74], dewetting of organic multilayer films [75], or refinement of block co-polymer thin film morphology during solvent vapor annealing [76]. Furthermore, working devices have also been investigated by in-situ GIXS so as to identify the structural changes that the active thin film undergo during operation with the aim of improving the device design and final performance, e.g., catalysis on nanoparticles [77], roughening of surfaces during electrodeposition [78], electrochemistry in ionomer matrices of interest in fuel-cell devices [79], or BHJ polymer solar cells [80, 81]. As in the previous section, the development of specific environmental cells to be installed at synchrotron beamlines commonly constitutes a prerequisite to conduct this kind of experiments. In the following, we will shortly describe some recent exemplary results of in-operando and in-situ GISAXS during thin film processing.

As mentioned in the previous paragraph, a well-known way of producing – or modifying the morphology of—metal nanoclusters on a surface consists in the thermal induced dewetting of metallic thin films. This process has been in-situ investigated by GISAXS for the case of Au on Si (1 1 1) up to the bulk eutectic point T_e of the Au/Si system [82]. After the deposition of Au thin nanostructured films by thermal evaporation, a linear increase of the mean distance between Au nanoclusters was observed—associated to an increase in cluster size—together with an increase in the mean cluster height as the temperature approached T_e, which jointly translated to an increase in the contact angle of the nanoclusters. More interestingly, from the Au nanoclusters contact angle at T_e, the liquid-solid interface tension of nanometer-sized Au clusters was calculated and it was found to be larger than that of macroscopic Au droplets on Si (1 1 1). Additionally, the work of adhesion of an Au nanodroplet at the system eutectic point was derived.

In the case of semiconductor materials, ion beam bombardment is a very useful process to induce surface nanostructuring. During the erosion of a surface by accelerated ions, the produced instabilities can lead to the formation of self-assembled patterns of nanostructures and different surface topographies can be obtained as a function of the ion mass, ion energy and bombardment geometry. In-situ GISAXS with partially coherent X-ray beams (Co-GISAXS) has been employed to study the nanodot formation on a gallium antimonide (GaSb) (0 0 1) surface by normal incidence bombardment of 500 eV Ar ions [83]. The use of partially coherent beams allows not only accessing the kinetic phenomena but also the dynamics. Under a coherent illumination, the scattered intensity consists of a speckle pattern (**Figure 10**) and the speckle distribution and speckle intensity fluctuations reflect the underlying dynamics of the surface morphology [84]. From a kinetic point of view—GISAXS analysis—the mean size and distance of the nanodots as a function of time was extracted and the kinetic regimes and onsets derived. More interestingly, though the characteristic GISAXS signal remained stable after saturation of the nanostructuring process, the dynamics showed that ageing—slow down

of the dynamics—was occurring, mainly ascribed to hindered mass redistribution phenomena. The dynamics was extracted from the speckle analysis through the so-called two-time correlation function that accounts for the fast variation of intensity redistribution within the scattering peak with respect to the averaged intensity distribution over time. Finally, a dynamical transition to a regime dominated by the build-up of stress at the surface was identified.

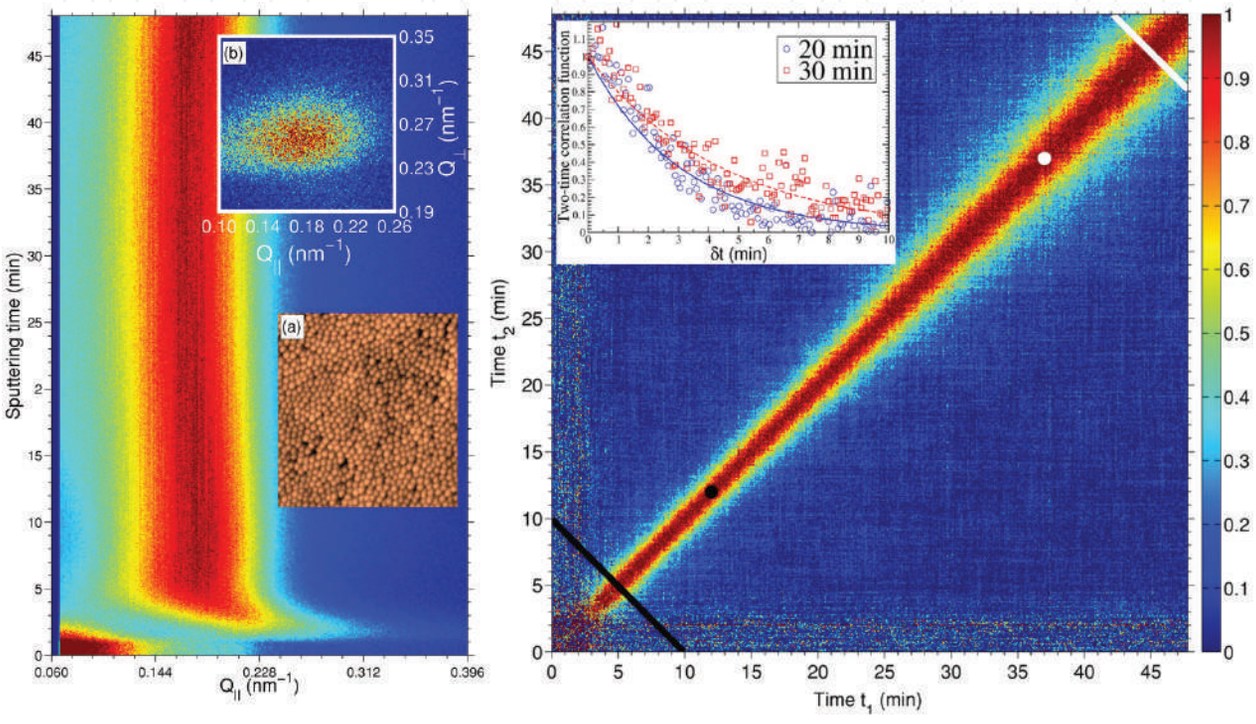

Figure 10. Left: Evolution of the GISAXS out-of-plane peak as a function of ion bombardment time. The onset of surface nanostructuring is evidenced by the emergence of the side peak 1 min after erosion started. After around 5 min the out-of-plane peak remained at constant position revealing the saturation of the nanostructuring process. The upper inset show the speckle distribution within the out-of-plane peak at t = 47 min whereas the lower inset shows the real-space morphology as revealed by atomic force microscopy. Right: Normalized two-time correlation function calculated around the out-of-plane GISAXS peak. The black and white lines mark the start and end of aging, respectively, whereas the black and white dots correspond to the average times where a change in the correlation time occurred (change in dynamical regimes). The inset shows cuts of the two-time correlation function as function of $\delta t = t_2 - t_1$ (hollow blue dots and hollow red squares). A good fitting was achieved using exponential decay functions. © 2013 O. Bikondoa, D. Carbone, V. Chamard and T.H. Metzger. Adapted from Bikondoa et al. [83]; originally published under Creative Commons Attribution 3.0 Unported License. Available from: 10.1038/srep01850.

On the other hand, nanostructuring of polymer thin films is an intense field of research and different strategies are being employed, e.g., nanoimprint lithography, porous anodic aluminum oxide (AAO) templating or, as mentioned in Section 3.1, the design of block co-polymer morphologies. An interesting approach consists in the formation of nanostructured surfaces by the so-called laser-induced periodic surface structure (LIPSS) formation, a technique that has been used for years to nanostructure metals and semiconductors but has only recently been applied to polymers [85, 86]. In LIPSS, a pulsed laser of a definite polarization is shined

http://dx.doi.org/10.5772/64877

on the material at fluences (optical energy per surface area) well below the ablation threshold and the material surface gets nanostructured by interference of the incoming and scattered electromagnetic wave through a feeding mechanism not yet well understood. In the common case of linearly polarized incident light the process induces ripple formation on the surface with a periodicity resembling the wavelength of the laser employed. By performing in-situ GISAXS measurements while irradiating a poly(trimethylene therephthalate) (PTT) thin film the onset of ripple formation at different laser repetition rates and fluences has been revealed [87]. Moreover, the results support a feeding mechanism based on a local heating of the polymer thin film so that LIPSS formation becomes more efficient the shorter is the laser pulse separation, whereas for long enough laser pulse separation heat dissipation takes place between pulses hindering the ripple formation.

A different way in which polymer thin films are processed does not consist in the promotion of structuring to tailor the material properties but in the processes that polymeric materials undergo during operation. For instance, in several applications the polymeric material is in contact with fluids, e.g., in the case of polymeric materials used in human implants. Here, the combination of μGISAXS and microfluidics offers unique capabilities for investigating the morphological changes of polymer thin films in contact with a fluid flow.

A model system comprising of a thin film of sodium alginate with embedded dispersed PS nanoparticles have been investigated by in-situ μGISAXS during water flow in a microfluidic device [88]. This system served as a model to investigate the detachment of thin films and nanoparticle aggregates therein by a fluid flow, both with and without additional sodium alginate cross-linking. More interestingly, the combination of in-situ μGISAXS and a microfluidic cell have resulted in the accurate description of the swelling behavior of the thermoresponsive poly(*N*-isopropylacrylamide) (PNIPAM) polymer, a well-known hydrogel when cross-linked [89]. An important feature observed in the GISAXS pattern of soft thin films deposited on rough surfaces is the correlated roughness of the film, i.e., the soft matter thin film present a roughness that replicates that of the substrate. Thus, the film shows X-ray waveguiding effects producing scattering with partial coherence and resonant diffuse scattering is observed [13]. In this case, the diffuse scattering with partial phase coherence coming from the different interfaces concentrates into narrow sheets parallel to the q_x direction and appear in the 2D GISAXS pattern as intensity modulations in the scattering plane (along q_z at $q_y = 0$). These modulations enable a direct determination of the distance between the correlated surfaces by $q_z = 2\pi/d_{\text{corr}}$ (**Figure 11(a)** and **(b)**). It is important to calculate d_{corr} for large q_z values so that the Yoneda peak intensity does not introduce an additional signal that could distort an accurate determination of d_{corr}. From the in-situ μGISAXS measurements, neither the thickness nor the topography of the PNIPAM thin film was observed to change during exposure to highly undersaturated water vapor. However, as early as the film is brought in contact with liquid water it starts swelling mostly in a 1D manner, i.e., mainly an increase of film thickness occurs, being the restructuration of the surface topography (surface flattening) slightly retarded but obviously correlated to the swelling process (**Figure 11(c)**).

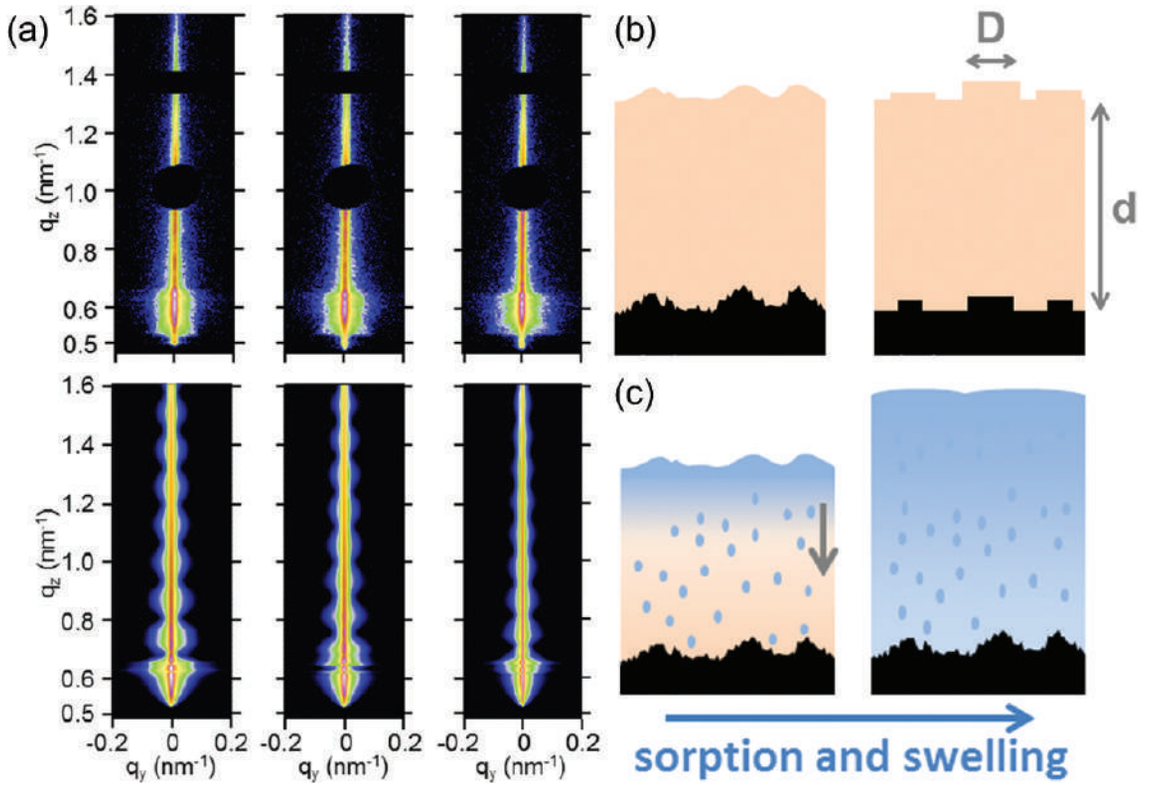

Figure 11. (a) Experimental (upper row) and simulated (lower row) 2D μGISAXS patterns during swelling of a PNIPAM thin film under water flow in a microfluidic cell. The scattering patterns correspond to exposure to water vapor (left), after 30 s of water flow (middle) and after 48 s of water flow (right). The GISAXS patterns were continuously acquired before and during water flow with a time resolution of 1 s. The DWBA and the LMA were employed to simulate the scattering patterns. (b) Schematic drawings of the glass-supported, as-spun PNIPAM film, possessing partially correlated interfaces (left) and the corresponding morphological model used in the simulations (right). The parameters that were varied to simulate the water uptake process are the thickness of the PNIPAM layer, d, and the diameter of the PNIPAM discs, D. (c) Illustration of the surface restructuration in the course of the swelling of the thin, glass-supported PNIPAM film. Left: sorption of liquid water, filling the accessible free PNIPAM volumes and inducing the devitrification of its near-surface layer. Right: mainly 1D swelling occurs as the gel-glass phase boundary propagates into the depth of the film; the surface flattens as the mobility of the macromolecules is sufficient. Reprinted (adapted) with permission from Philipp et al. [89]. Copyright 2015 American Chemical Society.

Other polymeric thin films that have been investigated by in-situ GISAXS during operation are the active layers of BHJ polymer solar cells (**Figure 12**). In general, although polymer solar cells hold the promise of future low-cost flexible solar cells, a major problem of these OPV devices is the performance loss during operation. In this sense, in-operando μGISAXS studies have revealed that the active layer suffer from morphological changes during operation [90]. These morphological changes are directly related to the decrease in short-circuit current density (SCCD) that was derived from the simultaneous measurement of current-voltage curves while the device was illuminated by a solar simulator. In order to demonstrate this unequivocal relationship between performance loss and morphological transformation, Monte Carlo (MC) simulations of the SCCD were performed using the structural parameters extracted from modeling of the μGISAXS patterns. The agreement between the MC simulations and the measured SCCD was excellent (**Figure 12(c)**) concluding that an increase in P3HT

http://dx.doi.org/10.5772/64877

domain size and separation during illumination is responsible for the decrease of effective light harvesting area, thus decreasing the exciton splitting events, whereas the PCBM domain size and distance remained fairly constant. Moreover, a temperature effect was ruled out since the solar cell did not exceed 45°C during the experiments due to Peltier cooling.

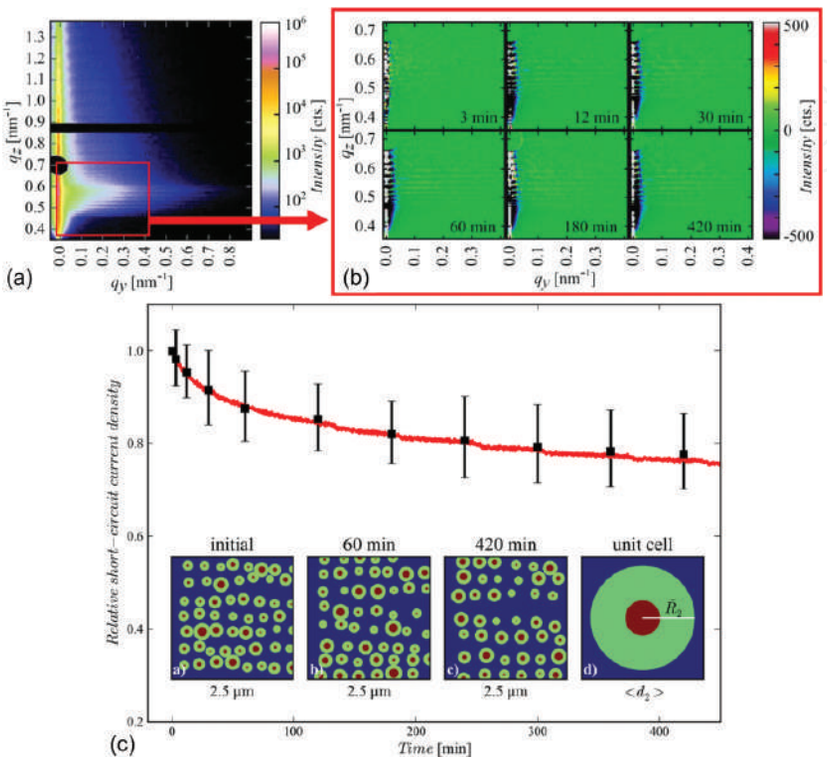

Figure 12. (a) 2D µGISAXS pattern of the polymer solar cell before illumination. (b) Difference scattering patterns, i.e., 2D µGISAXS measurements obtained at different operation times after subtraction of the initial scattering pattern within the marked window (red box) in (a). Negative values mean a loss of signal with respect to the initial measurement. (c) Simulated (black dots) and measured short-circuit current density (red line). The simulated short-circuit current density was derived from the morphological parameters extracted by µGISAXS. The insets show the inner film morphology at different times as generated by the Monte Carlo simulations. The inset on the right presents the domain morphology model used in the simulations and extracted from the µGISAXS experiments: red correspond to the core of P3HT domains, green to the effective light harvesting area and blue to the non-active effective area of the solar cell. Reproduced with permission from Schaffer et al. [90]. Copyright 2013, John Wiley and Sons.

5. Conclusions

In this chapter, we have reviewed the current trends in the application of time-resolved GISAXS for in-situ and in-operando studies during thin film formation and processing. It has been shown that GISAXS presents unique capabilities as a noninvasive technique with intrinsic statistical relevance and time resolutions down to the millisecond regime. Moreover, GISAXS constitutes a very versatile technique that can be applied to a large variety of materials with a vast range of applications, and the relative easiness of combining it with other characterization

techniques for simultaneous measurements offers the possibility of correlating the film structure to its properties, of utmost importance in most of the applications of thin films.

In the near future, the present developments for the next generation of 2D X-ray photon counting pixel detectors will allow investigating even faster processes since frame rates higher than 10 kHz with large detector dynamic ranges are foreseen. Additionally, the application of present technique improvements to in-situ studies will further contribute to gain deeper knowledge of thin film fabrication and processing. In this sense, the present advances in grazing incidence resonant soft X-ray scattering (GI-RSoXS), with its inherent material contrast through tuning the incident beam energy to one of the absorption edges of the materials under investigation, will certainly help in understanding, e.g., alloying, blending or phase segregation phenomena in-situ with adequate time resolution. Furthermore, the decrease in beam emittance at synchrotrons is currently enabling longer sample to detector distances—up to several tens of meters—which translates in access to lower q ranges (of the order of 0.001 nm $^{-1}$ or even lower, i.e., real space sizes in the micron range) by performing grazing incidence ultra-small angle X-ray scattering (GIUSAXS) experiments. Thus, through the combination of in-situ GIWAXS ($q \approx 1$–50 nm^{-1}), GISAXS ($q \approx 0.01$–1 nm^{-1}) and GIUSAXS ($q \approx 0.01$–0.0001 nm $^{-1}$) real space structures from 1 Å to 10 μm will be accessible, which will provide a complete morphological description of the processes from the atomic structure to the microscopic regime allowing to establish an extremely important link between atomic, nanoscopic and macroscopic ordering, which is not yet fully developed.

Finally, the development of new magnet arrays in storage rings is currently taking place and diffraction-limited sources are not far from becoming available. This will provide an enhanced coherence of the X-ray beams and therefore, it is not difficult to anticipate a growth in the application of time-resolved coherent GISAXS (Co-GISAXS). So far, most of the GISAXS experiments are noncoherent, thus the scattered photon phase is lost making modeling indispensable during data analysis. On the contrary, in Co-GISAXS the phase information can be directly retrieved via mathematical algorithms so that, to some extent, the morphology of the scattering entity can be directly reconstructed from the experimental data. Furthermore, as already known from other X-ray coherent techniques such as X-ray photon correlation spectroscopy (XPCS), not only kinetics but also dynamics of the nano-objects may be probed. However, a good resolution of the speckles is necessary to guarantee an accurate determination of the dynamical processes. This requires a high q resolution that corresponds to small detector pixel size and for fast dynamic processes 2D X-ray photon counting pixel detectors with pixel sizes comparable to those of CCD detectors will be indispensable.

Acknowledgements

We would like to kindly acknowledge José Ángel Martín-Gago for the critical reading of the chapter as well as Stefan Kowarik for his valuable suggestions in Section 3.2. S.Y. acknowledges the financial support from the Knut and Alice Wallenberg Foundation.

Author details

Gonzalo Santoro[1*] and Shun Yu[2]

*Address all correspondence to: gonzalo.santoro@icmm.es

1 Materials Science Institute of Madrid (ICMM-CSIC), Madrid, Spain

2 KTH Royal Institute of Technology, Stockholm, Sweden

References

[1] Zhao XY, Wei CM, Yang L, et al. Quantum confinement and electronic properties of silicon nanowires. Phys. Rev. Lett. 2004; 92. DOI: 10.1103/PhysRevLett.92.236805.

[2] Sun YG, Mayers B, Xia YN. Metal nanostructures with hollow interiors. Adv. Mater. 2003; 15:641–646. DOI: 10.1002/adma.200301639.

[3] Narayanan R,El-Sayed MA. Shape-dependent catalytic activity of platinum nanoparticles in colloidal solution. Nano Lett. 2004; 4:1343–1348. DOI: 10.1021/nl0495256.

[4] Kelly KL, Coronado E, Zhao LL, et al. The optical properties of metal nanoparticles: the influence of size, shape, and dielectric environment. J. Phys. Chem. B. 2003; 107:668–677. DOI: 10.1021/jp026731y.

[5] Daniel MC,Astruc D. Gold nanoparticles: assembly, supramolecular chemistry, quantum-size-related properties, and applications toward biology, catalysis, and nanotechnology. Chem. Rev. 2004; 104:293–346. DOI: 10.1021/cr030698+.

[6] Hentschel M, Saliba M, Vogelgesang R, et al. Transition from isolated to collective modes in plasmonic oligomers. Nano Lett. 2010; 10:2721–2726. DOI: 10.1021/nl101938p.

[7] Jiao F, Frei H. Nanostructured cobalt oxide clusters in mesoporous silica as efficient oxygen-evolving catalysts. Angew. Chem. Int. Ed. 2009; 48:1841–1844. DOI: 10.1002/anie.200805534.

[8] Ellison CJ,Torkelson JM. The distribution of glass-transition temperatures in nanoscopically confined glass formers. Nat. Mater. 2003; 2:695–700. DOI: 10.1038/nmat980.

[9] Glatter O, Kratky O, editors. Small Angle X-ray Scattering. London: Academic Press Inc.; 1982. 515 p. ISBN: 0-12-286280-5.

[10] Levine JR, Cohen LB, Chung YW, et al. Grazing-incidence small-angle X-ray-scattering —new tool for studying thin-film growth. J. Appl. Crystallogr. 1989; 22:528–532. DOI: 10.1107/s002188988900717x.

[11] Müller-Buschbaum P. Grazing incidence small-angle X-ray scattering: an advanced scattering technique for the investigation of nanostructured polymer films. Anal. Bioanal. Chem. 2003; 376:3–10. DOI: 10.1007/s00216-003-1869-2.

[12] Renaud G, Lazzari R, Leroy F. Probing surface and interface morphology with grazing incidence small angle X-ray scattering. Surf. Sci. Rep. 2009; 64:255–380. DOI: 10.1016/j.surfrep.2009.07.002.

[13] Müller-Buschbaum P. A basic introduction to grazing incidence small-angle X-ray scattering. In: Ezquerra TA, Nogales A, García-Gutiérrez MC, et al., editors. Applications of Synchrotron Light to Scattering and Diffraction in Materials and Life Sciences. Berlin, Heidelberg: Springer; 2009. p. 61–89. DOI: 10.1007/978-3-540-95968-7_3.

[14] Yoneda Y. Anomalous surface reflection of X rays. Phys. Rev. 1963; 131:2010–2013. DOI: 10.1103/PhysRev.131.2010.

[15] Lu XH, Yager KG, Johnston D, et al. Grazing-incidence transmission X-ray scattering: surface scattering in the Born approximation. J. Appl. Crystallogr. 2013; 46:165–172. DOI: 10.1107/s0021889812047887.

[16] Dosch H. Evanescent X-ray scattering. In: Dosch H, editor. Critical Phenomena at Surfaces and Interfaces: Evanescent X-Ray and Neutron Scattering. Berlin, Heidelberg: Springer; 1992. p. 6–31. DOI: 10.1007/BFb0045211.

[17] Robinson IK,Tweet DJ. Surface X-ray diffraction. Rep. Prog. Phys. 1992; 55:599–651. DOI: 10.1088/0034-4885/55/5/002.

[18] Lazzari R. IsGISAXS: a program for grazing-incidence small-angle X-ray scattering analysis of supported islands. J. Appl. Crystallogr. 2002; 35:406–421. DOI: 10.1107/s0021889802006088.

[19] Babonneau D. FitGISAXS: software package for modelling and analysis of GISAXS data using IGOR Pro. J. Appl. Crystallogr. 2010; 43:929–936. DOI: 10.1107/s0021889810020352.

[20] Chourou ST, Sarje A, Li XS, et al. HipGISAXS: a high-performance computing code for simulating grazing-incidence X-ray scattering data. J. Appl. Crystallogr. 2013; 46:1781–1795. DOI: 10.1107/s0021889813025843.

[21] Durniak C, Ganeva M, Pospelov G, et al. BornAgain—software for simulating and fitting X-ray and neutron small-angle scattering at grazing incidence [Internet]. 2015. Available from: http://www.bornagainproject.org [Accessed: 2016-05-23].

[22] Lee B, Yoon J, Oh W, et al. In-situ grazing incidence small-angle X-ray scattering studies on nanopore evolution in low-*k* organosilicate dielectric thin films. Macromolecules. 2005; 38:3395–3405. DOI: 10.1021/ma048214e.

[23] Busch P, Rauscher M, Smilgies DM, et al. Grazing-incidence small-angle X-ray scattering from thin polymer films with lamellar structures—the scattering cross section in

the distorted-wave Born approximation. J. Appl. Crystallogr. 2006; 39:433–442. DOI: 10.1107/s0021889806012337.

[24] Salditt T, Metzger TH, Peisl J, et al. Determination of the height-height correlation function of rough surfaces from diffuse X-ray scattering. Europhys. Lett. 1995; 32:331. DOI: 10.1209/0295-5075/32/4/008.

[25] Hexemer A, Mueller-Buschbaum P. Advanced grazing-incidence techniques for modern soft-matter materials analysis. IUCrJ. 2015; 2:106–125. DOI: 10.1107/s2052252514024178.

[26] Lazzari R, Leroy F, Renaud G. Grazing-incidence small-angle X-ray scattering from dense packing of islands on surfaces: development of distorted wave Born approximation and correlation between particle sizes and spacing. Phys. Rev. B. 2007; 76. DOI: 10.1103/PhysRevB.76.125411.

[27] Döhrmann R, Botta S, Buffet A, et al. A new highly automated sputter equipment for in situ investigation of deposition processes with synchrotron radiation. Rev. Sci. Instrum. 2013; 84. DOI: 10.1063/1.4798544.

[28] Cantelli V, Geaymond O, Ulrich O, et al. The In situ growth of nanostructures on surfaces (INS) endstation of the ESRF BM32 beamline: a combined UHV-CVD and MBE reactor for in situ X-ray scattering investigations of growing nanoparticles and semiconductor nanowires. J. Synchrotron Radiat. 2015; 22:688–700. DOI: 10.1107/s1600577515001605.

[29] Ibrahimkutty S, Seiler A, Prussmann T, et al. A portable ultrahigh-vacuum system for advanced synchrotron radiation studies of thin films and nanostructures: EuSi2 nanoislands. J. Synchrotron Radiat. 2015; 22:91–98. DOI: 10.1107/s1600577514019705.

[30] Renaud G, Lazzari R, Revenant C, et al. Real-time monitoring of growing nanoparticles. Science. 2003; 300:1416–1419. DOI: 10.1126/science.1082146.

[31] Lazzari R, Renaud G, Revenant C, et al. Adhesion of growing nanoparticles at a glance: surface differential reflectivity spectroscopy and grazing incidence small angle X-ray scattering. Phys. Rev. B. 2009; 79:125428. DOI: 10.1103/PhysRevB.79.125428.

[32] Revenant C, Renaud G, Lazzari R, et al. Defect-pinned nucleation, growth, and dynamic coalescence of Ag islands on MgO(001): an in situ grazing-incidence small-angle X-ray scattering study. Phys. Rev. B. 2009; 79:235424. DOI: 10.1103/PhysRevB.79.235424.

[33] Kaune G, Metwalli E, Meier R, et al. Growth and morphology of sputtered aluminum thin films on P3HT surfaces. ACS Appl. Mater. Interfaces. 2011; 3:1055–1062. DOI: 10.1021/am101195m.

[34] Schwartzkopf M, Buffet A, Korstgens V, et al. From atoms to layers: in situ gold cluster growth kinetics during sputter deposition. Nanoscale. 2013; 5:5053–5062. DOI: 10.1039/c3nr34216f.

[35] Santoro G, Yu S, Schwartzkopf M, et al. Silver substrates for surface enhanced Raman scattering: correlation between nanostructure and Raman scattering enhancement. Appl. Phys. Lett. 2014; 104:243107. DOI: 10.1063/1.4884423.

[36] Paul N, Metwalli E, Yao Y, et al. Templating growth of gold nanostructures with a CdSe quantum dot array. Nanoscale. 2015; 7:9703–9714. DOI: 10.1039/c5nr01121c.

[37] Yu S, Santoro G, Sarkar K, et al. Formation of Al nanostructures on Alq3: an in situ grazing incidence small angle X-ray scattering study during radio frequency sputter deposition. J. Phys. Chem. Lett. 2013; 4:3170–3175. DOI: 10.1021/jz401585d.

[38] Yu S, Santoro G, Yao Y, et al. Following the island growth in real time: Ag nanocluster layer on Alq3 thin film. J. Phys. Chem. C. 2015; 119:4406–4413. DOI: 10.1021/jp512675w.

[39] Schwartzkopf M, Santoro G, Brett CJ, et al. Real-time monitoring of morphology and optical properties during sputter deposition for tailoring metal-polymer interfaces. ACS Appl. Mater. Interfaces. 2015; 7:13547–13556. DOI: 10.1021/acsami.5b02901.

[40] Metwalli E, Körstgens V, Schlage K, et al. Cobalt nanoparticles growth on a block copolymer thin film: a time-resolved GISAXS study. Langmuir. 2013; 29:6331–6340. DOI: 10.1021/la400741b.

[41] Erb DJ, Schlage K, Röhlsberger R. Uniform metal nanostructures with long-range order via three-step hierarchical self-assembly. Sci. Adv. 2015; 1:e1500751. DOI: 10.1126/sciadv.1500751.

[42] Roth SV, Santoro G, Risch JFH, et al. Patterned diblock co-polymer thin films as templates for advanced anisotropic metal nanostructures. ACS Appl. Mater. Interfaces. 2015; 7:12470–12477. DOI: 10.1021/am507727f.

[43] Ritley KA, Krause B, Schreiber F, et al. A portable ultrahigh vacuum organic molecular beam deposition system for in situ X-ray diffraction measurements. Rev. Sci. Instrum. 2001; 72:1453–1457. DOI: 10.1063/1.1336822.

[44] Ferrer P, Rubio-Zuazo J, Heyman C, et al. A multipurpose ultra-high vacuum-compatible chamber for in situ X-ray surface scattering studies over a wide range of temperature and pressure environment conditions. J. Phys.: Conf. Series. 2013; 425:132002. DOI: 10.1088/1742-6596/425/13/132002.

[45] Schreiber F, Eberhardt A, Leung TYB, et al. Adsorption mechanisms, structures, and growth regimes of an archetypal self-assembling system: Decanethiol on Au(111). Phys. Rev. B. 1998; 57:12476–12481. DOI: 10.1103/PhysRevB.57.12476.

[46] Kowarik S, Gerlach A, Sellner S, et al. Real-time observation of structural and orientational transitions during growth of organic thin films. Phys. Rev. Lett. 2006; 96:125504. DOI: 10.1103/PhysRevLett.96.125504.

[47] Mayer AC, Kazimirov A, Malliaras GG. Dynamics of bimodal growth in pentacene thin films. Phys. Rev. Lett. 2006; 97. DOI: 10.1103/PhysRevLett.97.105503.

[48] Kowarik S, Gerlach A, Schreiber F. Organic molecular beam deposition: fundamentals, growth dynamics, and in situ studies. J. Phys.: Condens. Matter. 2008; 20. DOI: 10.1088/0953-8984/20/18/184005.

[49] Kowarik S, Gerlach A, Skoda MWA, et al. Real-time studies of thin film growth: measurement and analysis of X-ray growth oscillations beyond the anti-Bragg point. Eur. Phys. J.: Special Topics. 2009; 167:11–18. DOI: 10.1140/epjst/e2009-00930-y.

[50] Woll AR, Desai TV, Engstrom JR. Quantitative modeling of in situ X-ray reflectivity during organic molecule thin film growth. Phys. Rev. B. 2011; 84. DOI: 10.1103/PhysRevB.84.075479.

[51] Alvarez J, Lundgren E, Torrelles X, et al. Effect of a surfactant in homoepitaxial growth of Ag (001): dendritic versus faceted island morphologies. Surf. Sci. 2000; 464:165–175. DOI: 10.1016/s0039-6028(00)00648-8.

[52] Fleet A, Dale D, Woll AR, et al. Multiple time scales in diffraction measurements of diffusive surface relaxation. Phys. Rev. Lett. 2006; 96. DOI: 10.1103/PhysRevLett.96.055508.

[53] Ferguson JD, Arikan G, Dale DS, et al. Measurements of surface diffusivity and coarsening during pulsed laser deposition. Phys. Rev. Lett. 2009; 103. DOI: 10.1103/PhysRevLett.103.256103.

[54] Frank C, Banerjee R, Oettel M, et al. Analysis of island shape evolution from diffuse X-ray scattering of organic thin films and implications for growth. Phys. Rev. B. 2014; 90. DOI: 10.1103/PhysRevB.90.205401.

[55] Bommel S, Kleppmann N, Weber C, et al. Unravelling the multilayer growth of the fullerene C60 in real time. Nat. Commun. 2014; 5:5388. DOI: 10.1038/ncomms6388.

[56] Frank C, Novak J, Banerjee R, et al. Island size evolution and molecular diffusion during growth of organic thin films followed by time-resolved specular and off-specular scattering. Phys. Rev. B. 2014; 90:045410. DOI: 10.1103/PhysRevB.90.045410.

[57] Zykov A, Bommel S, Wolf C, et al. Diffusion and nucleation in multilayer growth of PTCDI-C8 studied with in situ X-ray growth oscillations and real-time small angle X-ray scattering. J. Chem. Phys. Accepted manuscript.

[58] Vegso K, Siffalovic P, Jergel M, et al. A non-equilibrium transient phase revealed by in situ GISAXS tracking of the solvent-assisted nanoparticle self-assembly. J. Nanopart. Res. 2014; 16:1–11. DOI: 10.1007/s11051-014-2536-6.

[59] Corricelli M, Altamura D, Curri ML, et al. GISAXS and GIWAXS study on self-assembling processes of nanoparticle based superlattices. Cryst. Eng. Commun. 2014; 16:9482–9492. DOI: 10.1039/C4CE01291G.

[60] Chou KW, Yan B, Li R, et al. Spin-cast bulk heterojunction solar cells: a dynamical investigation. Adv. Mater. 2013; 25:1923–1929. DOI: 10.1002/adma.201203440.

[61] Perlich J, Schwartzkopf M, Körstgens V, et al. Pattern formation of colloidal suspensions by dip-coating: an in situ grazing incidence X-ray scattering study. Phys. Stat. Sol. Rapid Res. Lett. 2012; 6:253–255. DOI: 10.1002/pssr.201206114.

[62] Nagpure S, Das S, Garlapalli RK, et al. In situ GISAXS investigation of low-temperature aging in oriented surfactant-mesostructured titania thin films. J. Phys. Chem. C. 2015; 119:22970–22984. DOI: 10.1021/acs.jpcc.5b06945.

[63] Smilgies D-M, Li R, Giri G, et al. Look fast: crystallization of conjugated molecules during solution shearing probed in-situ and in real time by X-ray scattering. Phys. Stat. Sol. Rapid Res. Lett. 2013; 7:177–179. DOI: 10.1002/pssr.201206507.

[64] Abdellah A, Virdi KS, Meier R, et al. Successive spray deposition of P3HT/PCBM organic photoactive layers: material composition and device characteristics. Adv. Funct. Mater. 2012; 22:4078–4086. DOI: 10.1002/adfm.201200548.

[65] Sarkar K, Braden EV, Pogorzalek S, et al. Monitoring structural dynamics of in situ spray-deposited zinc oxide films for application in dye-sensitized solar cells. ChemSusChem. 2014; 7:2140–2145. DOI: 10.1002/cssc.201402049.

[66] Song L, Wang W, Körstgens V, et al. Spray Deposition of titania films with incorporated crystalline nanoparticles for all-solid-state dye-sensitized solar cells using P3HT. Adv. Funct. Mater. 2016; 26:1498–1506. DOI: 10.1002/adfm.201504498.

[67] Herzog G, Benecke G, Buffet A, et al. In situ grazing incidence small-angle X-ray scattering investigation of polystyrene nanoparticle spray deposition onto silicon. Langmuir. 2013; 29:11260–11266. DOI: 10.1021/la402254q.

[68] Zhang P, Santoro G, Yu S, et al. Manipulating the assembly of spray-deposited nanocolloids: in situ study and monolayer film preparation. Langmuir. 2016; 32:4251–4258. DOI: 10.1021/acs.langmuir.6b00892.

[69] Palumbiny CM, Liu F, Russell TP, et al. The crystallization of PEDOT:PSS polymeric electrodes probed in situ during printing. Adv. Mater. 2015; 27:3391–3397. DOI: 10.1002/adma.201500315.

[70] Pröller S, Liu F, Zhu C, et al. Following the morphology formation in situ in printed active layers for organic solar cells. Adv. Energy Mater. 2016; 6:1501580. DOI: 10.1002/aenm.201501580.

[71] Moulin JF, Roth SV, Müller-Buschbaum P. Flow at interfaces: a new device for X-ray surface scattering investigations. Rev. Sci. Instrum. 2008; 79:015109. DOI: 10.1063/1.2816220.

[72] Santoro G, Buffet A, Döhrmann R, et al. Use of intermediate focus for grazing incidence small and wide angle X-ray scattering experiments at the beamline P03 of PETRA III, DESY. Rev. Sci. Instrum. 2014; 85:043901. DOI: 10.1063/1.4869784.

[73] Felici R, Jeutter NM, Mussi V, et al. In situ study of the dewetting behavior of Ni-films on oxidized Si(001) by GISAXS. Surf. Sci. 2007; 601:4526–4530. DOI: 10.1016/j.susc.2007.04.210.

[74] Daudin R, Nogaret T, Schuelli TU, et al. Epitaxial orientation changes in a dewetting gold film on Si(111). Phys. Rev. B. 2012; 86. DOI: 10.1103/PhysRevB.86.094103.

[75] Bommel S, Spranger H, Weber C, et al. Thermally-activated post-growth dewetting of fullerene C60 on mica. Phys. Status Sol. Rapid Res. Lett. 2015; 9:646–651. DOI: 10.1002/pssr.201510258.

[76] Zhang J, Posselt D, Smilgies D-M, et al. Lamellar diblock copolymer thin films during solvent vapor annealing studied by GISAXS: different behavior of parallel and perpendicular lamellae. Macromolecules. 2014; 47:5711–5718. DOI: 10.1021/ma500633b.

[77] Hejral U, Muller P, Balmes O, et al. Tracking the shape-dependent sintering of platinum-rhodium model catalysts under operando conditions. Nat. Commun. 2016; 7:10964. DOI: 10.1038/ncomms10964.

[78] Ruge M, Golks F, Zegenhagen J, et al. In operando GISAXS studies of mound coarsening in electrochemical homoepitaxy. Phys. Rev. Lett. 2014; 112:055503. DOI: 10.1103/PhysRevLett.112.055503.

[79] Modestino MA, Kusoglu A, Hexemer A, et al. Controlling nafion structure and properties via wetting interactions. Macromolecules. 2012; 45:4681–4688. DOI: 10.1021/ma300212f.

[80] Wang W, Schaffer CJ, Song L, et al. In operando morphology investigation of inverted bulk heterojunction organic solar cells by GISAXS. J. Mater. Chem. A. 2015; 3:8324–8331. DOI: 10.1039/C5TA01109D.

[81] Schaffer CJ, Palumbiny CM, Niedermeier MA, et al. Morphological degradation in low bandgap polymer solar cells—an in-operando study. Adv. Energy Mater. 2016; 1600712. DOI: 10.1002/aenm.201600712.

[82] Daudin R, Revenant C, Davi G, et al. Growth and dewetting of gold on Si(1 1 1) investigated in situ by grazing incidence small angle X-ray scattering. Physica E: Low Dimens. Syst. Nanostruct. 2012; 44:1905–1909. DOI: 10.1016/j.physe.2012.05.021.

[83] Bikondoa O, Carbone D, Chamard V, et al. Ageing dynamics of ion bombardment induced self-organization processes. Sci. Rep. 2013; 3:1850. DOI: 10.1038/srep01850.

[84] Nugent KA. Coherent methods in the X-ray sciences. Adv. Phys. 2010; 59:1–99. DOI: 10.1080/00018730903270926.

[85] Rebollar E, Vazquez de Aldana JR, Martin-Fabiani I, et al. Assessment of femtosecond laser induced periodic surface structures on polymer films. Phys. Chem. Chem. Phys. 2013; 15:11287–11298. DOI: 10.1039/c3cp51523k.

[86] Martínez-Tong DE, Rodríguez-Rodríguez A, Nogales A, et al. Laser fabrication of polymer ferroelectric nanostructures for nonvolatile organic memory devices. ACS Appl. Mater. Interfaces. 2015; 7:19611–19618. DOI: 10.1021/acsami.5b05213.

[87] Rebollar E, Rueda DR, Martín-Fabiani I, et al. In situ monitoring of laser-induced periodic surface sStructures formation on polymer films by grazing incidence small-angle X-ray scattering. Langmuir. 2015; 31:3973–3981. DOI: 10.1021/acs.langmuir.5b00285.

[88] Körstgens V, Philipp M, Magerl D, et al. Following initial changes in nanoparticle films under laminar flow conditions with in situ GISAXS microfluidics. RSC Adv. 2014; 4:1476–1479. DOI: 10.1039/c3ra44554b.

[89] Philipp M, Körstgens V, Magerl D, et al. Sorption of water and initial stages of swelling of thin PNIPAM films using in situ GISAXS microfluidics. Langmuir. 2015; 31:9619–9627. DOI: 10.1021/acs.langmuir.5b01978.

[90] Schaffer CJ, Palumbiny CM, Niedermeier MA, et al. A direct evidence of morphological degradation on a nanometer scale in polymer solar cells. Adv. Mater. 2013; 25:6760–6764. DOI: 10.1002/adma.201302854.

Chapter 3

Grazing-Incidence Small Angle X-Ray Scattering in Polymer Thin Films Utilizing Low-Energy X-Rays

Katsuhiro Yamamoto

Additional information is available at the end of the chapter

http://dx.doi.org/10.5772/65090

Abstract

The intricate nanoscopic morphology of soft materials such as block copolymer and polymer blend system successfully analyzed by small angle X-ray scatterings (SAXS). In thin films, those soft material systems have attracted great attention because of a potential for practical use of functional materials. The morphology has been revealed by grazing-incidence (GI) methods. Recently, advanced grazing-incidence technique for analysis for surface-, volume-, and material-sensitive method (high time, spatial, and/or material resolution) has been reported. Using low X-ray photon energy, tender X-ray (1–4 eV) and soft X-ray near *K*-edge carbon, allows probing a complex nanomorphology with those sensitivity. In this chapter, recent GI-SAXS with tender X-ray and resonant soft X-ray (GI-RSoX) will be picked up to open for discussion on new possibility of structural analyses.

Keywords: grazing-incidence X-ray scattering, organic thin film, block copolymer, tender X-rays, depth profiling

1. Introduction

Block copolymer (BCP) composed of two (more) immiscible polymers form variety structures with the periodicity of several tens nanometer both in bulk and thin films. BCP thin film has attracted great attention as an applicable material to various fields, e.g., solar cell [1–3], nanolithography [4–6], and size-selective separation [7, 8]. In bulk state, microphase-separated structure is predicted by the Flory-Huggins interaction parameter, the degree of polymerization, and the volume fraction of blocks [9], whereas in thin film, film thickness [10, 11] and substrate-polymer interaction and/or also polymer-air interaction[12] must be taken into

consideration. Controlling morphology, orientation and size of the structures are necessary for practical use although phase-separation behavior of BCP in thin film becomes more complicated. This has motivated numerous orientation control methodology studies that have examined the influence of film thickness [10, 11, 13, 14], surface/or interfacial free energy [14–17], surface topology [15, 18, 19], external applied fields (shear-induced [4, 20], electric field [21], magnetic field [22], and light-driven [23, 24]), solvent vapor or thermal annealing[25–30], and directional solidification [31–33]. Since functionality and physical property are also strongly related to the structure and the mobility in the vicinity of interface, revealing structure in detail is required. Suitable characterization techniques are required to monitor the structures of BCP both laterally and in-depth. Several approaches have been used to find BCP structures. Atomic force microscopy (AFM), electron microscopy, dynamic secondary ion mass spectrometry (DSIMS), X-ray photoelectron spectroscopy (XPS), grazing incidence small angle X-ray or neutron scattering (GISAXS, GISANS), X-ray or neutron reflectivity (XRR, NR), etc. have been used to study the structure of BCP thin films. AFM can enable an access of the information only near the surface although the surface structure can be directly observed and easily understandable. Electron microscopy is a powerful tool for visually examining a cross-sectional view of polymeric thin films in two-and three-dimensional real space [34]. DSIMS can elucidate the BCP morphology and the self-diffusion of polymer chains in thin films along a depth direction [35]. Time-of-flight (ToF) SIMS using ion cluster beam was reported to be a particularly well-suited technique that enables the in-depth profiling of polymers [36, 37]. X-ray photoelectron spectroscopy depth profiling with $C60^{+}$ sputtering revealed the ion distribution in lithium salt-doped BCP thin films [38, 39].Electron microscopy, DSIMS, and XPS techniques are essentially accompanied by the destruction of specimen because of processing such as sectioning or etching for analysis. In particular, it is important to take into account the deformation and losing of a precise original spatial coordinate induced by sectioning and chemical reactions induced by etching in the analysis of results obtained by these techniques. In contrast, neutron reflectivity (NRR) measurements enable a practically nondestructive analysis of depth profiles and ordering of microphase-separated structure in BCP thin films [40, 41]. However, the NRR provides structural information (density profile) only in the vertical direction to the sample surface and lateral information of the structure is inaccessible. In addition, accuracy of the density profile (depth-resolved information) perpendicular to the surface becomes worse when the film thickness is large for analyzing periodicity of microphase-separated structure. Generally, NRR depth profiling is suited for very thin film (less than 100 nm) as in the above case. GISAXS is another very powerful tool for understanding the nanostructure in both vertical and lateral directions of organic thin film (BCP thin film). And GISAXS is essentially nondestructive method under the condition of the no radiation damage of X-rays [42–47]. Commonly, SAXS and GISAXS methods have been conducted using hard X-rays with energy range of 6–14 keV. However, under these conditions, the penetration depth of X-rays rapidly reaches the thickness scale of the organic materials in the vicinity of the critical angle α_C of total reflection at the polymeric surface, which is making depth-resolved GISAXS measurements with hard X-rays totally impractical. A depth-sensitive GISAXS method using tender X-ray (1.77 keV) was first reported for the BCP thin film by Okuda et al. [48] and Wernecke et al. [49]. They investigated the structural relaxation near the

http://dx.doi.org/10.5772/65090

surface and the dynamic heterogeneity of polymer chains in thin films. At even lower X-ray photon energies, near the adsorption *K* edges of the polymeric materials (the oxygen, nitrogen, and carbon *K* edges), the fine structure of the adsorption edge can be utilized in GISAXS as reported by Ruderer et al. [50]. The grazing-incidence resonant soft X-ray (GI-RSoXS) has been applied for polymer blend thin films with low contrast in the real part of the refractive index for the hard X-rays but with significant differences in the soft X-ray regime. Furthermore, the X-ray penetration depth is drastically affected by the changes in the X-ray photon energy across the *K*-edge. The surface-and volume-sensitive structure of polymer blend films had been analyzed using this technique [50]. Similar to the GISAXS, GISANS has been developed by Müller-Buschbaum and co-workers. GISANS is a perfectly nondestructive approach for structure analysis and has essentially the same capability for surface-sensitive [51], interface-sensitive (structural information near the polymer-substrate interface enabled by the ability of the neutrons to go through the substrate) [52, 53], and depth-sensitive analysis [54]. Moreover, in time-of-flight mode GISANS (ToF-GISANS) [52, 55] a broad wavelength band is used instead of a single neutron wavelength, i.e., a range of different scattering vectors is directly probed by the measurement under a fixed angle of incidence. At an appropriate incident angle, it is possible to simultaneously conduct surface- and bulk-sensitive measurements. While GISANS possesses advantages as compared with the GISAXS, GISANS experiments still remain very rare because GISANS requires very high-flux sources to measure the much weaker signals in grazing-incidence geometry and the need for deuterium labeling (in some cases, of course, this is beneficial for structure analysis by tuning the contrast). These GISANS techniques have been well summarized in the reviews [56].

In this chapter, recent advanced GISAXS experiment utilizing low-energy X-rays will be introduced. GISAXS probes the complex nano- and microphase-separated structure in polymer thin films. Especially, tuning the energy of GISAXS in the tender and soft X-ray regime allows to the tailoring of X-ray penetration depth and contrast and thereby the probing of more complex morphologies in polymer thin films. GI-RSoXS has been applied for polymer blend thin films with low contrast in the real part of the refractive index for the hard X-rays but with significant differences in the soft X-ray regime. Furthermore, the X-ray penetration depth is drastically affected by the changes in the X-ray photon energy across the *K*-edge. The surface-and volume-sensitive structure of polymer blend films had been analyzed using this technique.

2. Grazing-incidence small angle X-ray scattering

Incident X-ray beam goes into the sample surface at a very shallow angle α_i (normally less than 1°). Scattering is measured with a two-dimensional detector as a function of the exit angle α_f (out-of-plane angle) and the in-plane angle 2Θ. The magnitude of the scattering vector is given by $q = 4\pi\sin\theta/\lambda$($\lambda$: wavelength of X-ray, 2θ: scattering angle). The scattering vector q_z means the component vertical to the film surface. The q_x and q_y are the components of scattering vectors in the sample surface, perpendicular to and directed to the X-ray beam, respectively. For each data set *I*(y, z), pixels of the detector were converted into exit angle α_f normal to the

sample surface and a scattering angle 2Θ parallel to the surface by simple geometrical consideration. The amplitude of scattering vector q is composed of q_x, q_y, and q_z related to the experimental angles by

$$q = \begin{pmatrix} q_x \\ q_y \\ q_z \end{pmatrix} = \frac{2\pi}{\lambda} \begin{pmatrix} \cos 2\Theta \cos\alpha_f - \cos\alpha_i \\ \sin 2\Theta \cos\alpha_f \\ \sin\alpha_i + \sin\alpha_f \end{pmatrix}, \quad (1)$$

As shown in **Figure 1**, typical sample-to-detector distances (SSD) for GISAXS are of the order of 1–2 m. In the case of small angle scattering, the two-dimensional detector probes mainly the q_y and q_z information because q_x is very small and the curvature of the Ewald sphere is negligible. The calculation of the out-of-plane scattering vector is considerably complex. Above critical angle α_C of polymeric materials, the theoretical penetration depth is much larger than the film thickness (order of micro-meter) (when hard X-ray is normally used) as shown in **Figure 2**. The transmitted wave can therefore be reflected at the polymer-substrate interface in combination with diffraction from the structures in the thin film. Under the assumption that each X-ray scatters no more than once from the objects and there is no transmission through the substrate, there are four possible scattering events to happen, additionally refraction at the sample surface (air-polymer interface) (**Figure 3**).

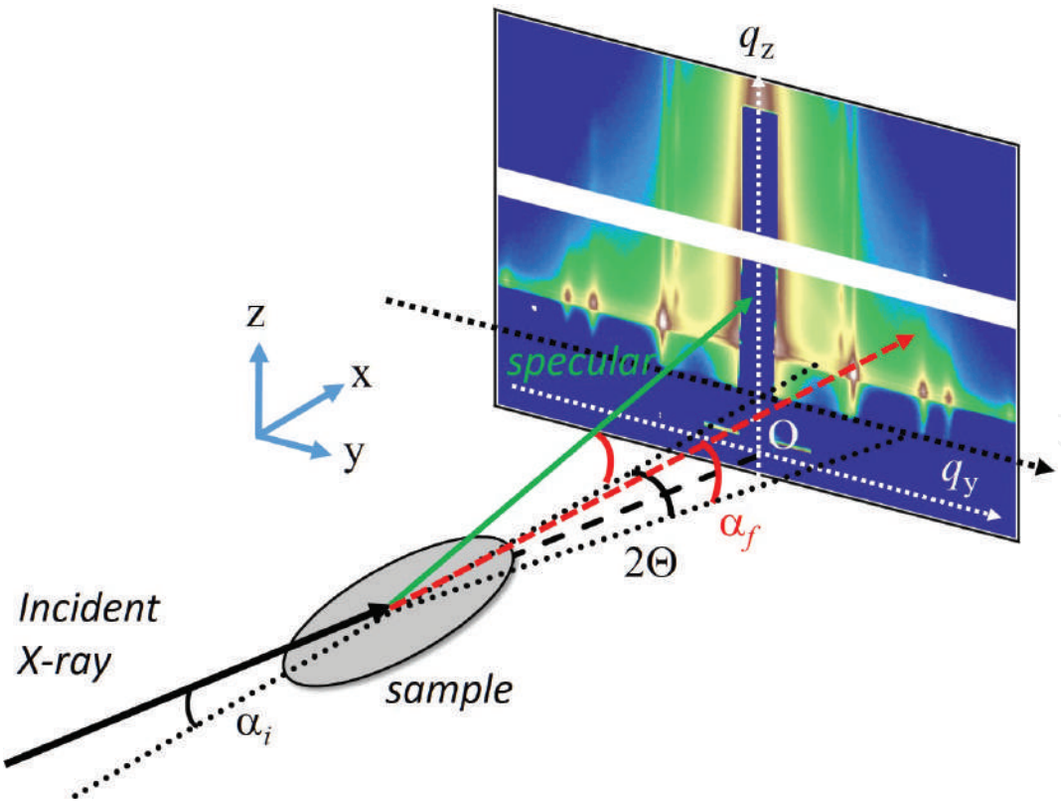

Figure 1. Schematic illustration of the scattering geometry used in GISAXS. The sample surface is inclined by incident angle with respect to the horizon. The exit and in-plane angles are denoted α_i and 2Θ, reepectively.

http://dx.doi.org/10.5772/65090

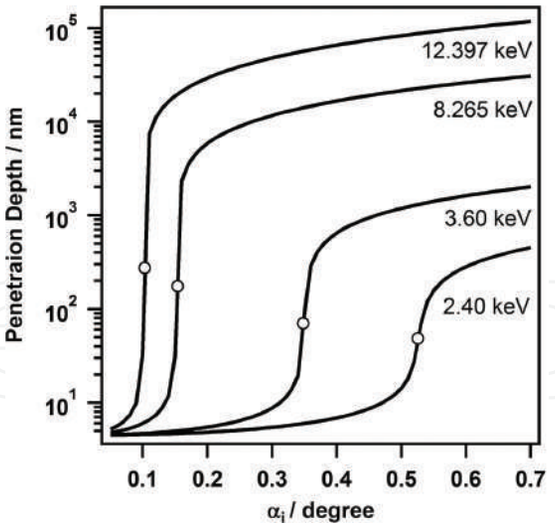

Figure 2. Penetration depth calculated for a block copolymer (S2VP) film for different X-ray energies, 12.397, 8.265, 3.60, and 2.40 keV.

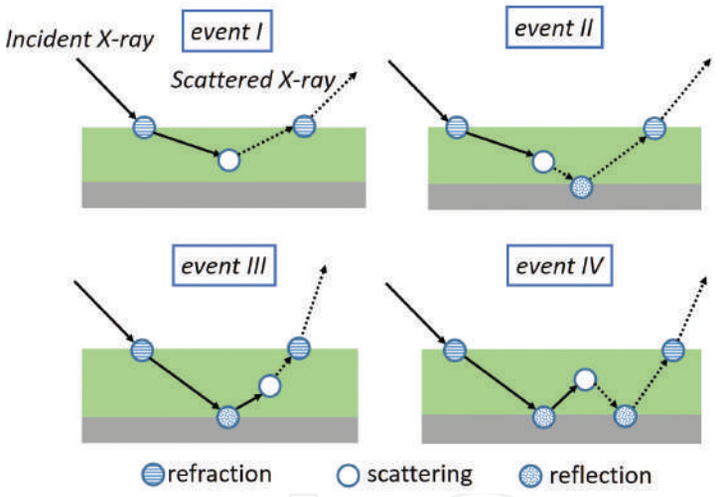

Figure 3. Four scattering events, demonstrating different combinations of reflection from the substrate with diffraction from the objects.

3. Depth-resolved structure analysis of microphase-separated structures in block copolymer thin film by grazing-incidence small angle X-ray scattering utilizing tender X-ray

3.1. Cylindrical microdomain in block copolymer thin film [57]

In this section, GISAXS measurement with low energy (tender) X-ray (2.40 keV) is introduced in order to precisely elucidate the depth profile of a microphase-separated structure (hexago-

nally packed cylinders) of a polystyrene-b-poly (2-vinylpyridine (S2VP) thin film on a silicon wafer with the cylindrical microdomains (poly (2-vinylpyridine): P2VP) oriented parallel to the substrate after the appropriate thermal annealing in vacuum. The cylindrical domains in the S2VP thin film were preferentially oriented parallel to the surface of the substrate induced by the surface free energies and/or an interfacial interaction between S2VP and the substrate. In GISAXS, the structural parameters of the cylindrical domains in both the lateral and vertical directions are accessible because the diffraction spots appear with the offset in the q_y direction.

S2VP thin film (number average molecular weight M_n = 26,400, molecular weight polydispersity index = 1.24, and φ_{PS} = 76.3 vol%) was prepared by spin casting from toluene solution (10 wt%) of S2VP onto a silicon wafer substrate at 3000 rpm for 30 s. Subsequently, the S2VP thin film was thermally annealed under vacuum at 170 °C for 48 h. The sample surface was composed of PS component (X-ray photoelectron spectroscopy and water contact angle [58], predicted by surface free energies of components [59]) was a very flat and smooth examined by atomic force microscopy and optical white-light interferometer microscopy measurements.

Tender X-ray GISAXS measurement (room temperature) was performed at BL15A2 [60] at the Photon Factory, KEK, Tsukuba in Japan. The BL15A2 is an undulator beamline where X-rays in a wide energy range from 2.1 to 15 keV (energy resolution is 2×10^{-4}) is available. In this study, the energy of X-ray was set at 2.40 keV (the wavelength of 5.16 Å) and the sample-to-detector distance (SDD) was 830 ± 5 mm. The accuracy of the camera lengths arises from the scattering vector calibration on a detector with a standard specimen and a footprint of the incident beam on the sample surface (sample size of c.a.1 cm). The X-ray incident angle was varied between 0.290° and 0.620° and PILATUS 2M designed for usage in vacuum was used as a detector for the 2D scattering pattern. X-ray exposure time of 300 s was sufficient to obtain a clear scattering pattern. Hard X-ray (wavelength 1.0 Å) GISAXS measurements were performed at BL10C in Photon Factory and BL03XU57 in SPring-8, Harima, Japan using PILATUS 2M and CCD (Hamamatsu Photonics) detectors with SDD of 2.3 m. All detectors were calibrated using lead stearate prepared in-house (d = 5.01 nm, calibrated).

The X-ray penetration depth Λ is defined as the depth at which the X-ray intensity is attenuated by 1/e. The value of Λ depends on X-ray energy (wavelength λ), the critical angle, α_C, of total reflection, and the incident angle α_i. Surface roughness influences practically the penetration depth of X-rays because various α_i are provided. The roughness of the surface used here is regarded as sufficiently small to estimate the penetration depth as evidenced by the clear observation of the critical angle in XRR. Under experimental conditions with the ideally flat surface, Λ is given by

$$\Lambda = \frac{\lambda}{4\pi}\sqrt{\frac{2}{\sqrt{(\alpha_i^2 - \alpha_c^2)^2 + 4\beta^2} - (\alpha_i^2 - \alpha_c^2)}}, \tag{2}$$

http://dx.doi.org/10.5772/65090

where β is the imaginary part of the complex refractive index. The critical angle α_C is specified as $\alpha_c \sim \sqrt{2\delta}$ where δ is deviation from the real part of the refractive index, δ and β are given by

$$\delta = \left(r_e \lambda^2 N_A / 2\pi\right) \rho_M \sum_Z w_Z \left(f_{0Z} + f'_Z(E)\right) / \sum_Z w_i A_Z, \tag{3}$$

$$\beta = \left(r_e \lambda^2 N_A / 2\pi\right) \rho_M \sum_Z w_Z f''_Z(E) / \sum_Z w_Z A_Z, \tag{4}$$

where r_e is the classical electron radius (2.82×10^{-5} Å), N_A is Avogadro's number, ρ_M is the mass density, w_Z is the fraction of element Z, $A_{Z,}$ is the relative atomic mass, f_{0Z} is the nonresonant term of the atomic scattering factor corresponding to the atomic number, and $f'_Z(E)$ and $f''_Z(E)$ are the real and imaginary parts of the anomalous dispersion for the incident X-ray energy E, respectively. For example, here we used 4.1468×10^{-5} for δ and 7.0239×10^{-7} for β of PS at 2.40 keV. The α_c value of S2VP thin film using GISAXS and XRR measurements was obtained. The calculated S2VP penetration depth is shown in **Figure 2**. It is hard to precisely control the penetration depth Λ at the nanometer scale for GISAXS experiment conducted using hard X-rays (8–12.4 keV) because the value of Λ rises steeply at α_C. On the other hand, as the X-ray energy decreases, Λ changes more gradually near the critical angle and shows decreased depth values at angles even greater than α_C. Hence, better control ofΛ is expected for depth-resolved GISAXS measurements using tender X-ray (2.40 keV) because of the critical angle and attenuation coefficient values that are much greater than those for the hard X-rays.

GISAXS measurements of the S2VP thin film (thickness of 420 nm) using tender X-ray were performed at various incident angles and many Bragg spots were measured as shown for large α_i in **Figure 4**. All spots were assigned to parallel oriented hexagonally packed cylinders. GISAXS patterns at approximately q_y of 0.26 nm^{-1} are presented in **Figure 4(c)** and **(d)** and show a remarkable elongation of the Bragg spots in the q_z direction for smaller α_i. One-dimensional scattering profiles vertically cut at q_y = 0.26 nm^{-1} with various incident angles are shown in **Figure 5**. Bragg peaks were assigned to the scattering from transmitted (denoted by T) and reflected (denoted by R) beams by the substrate. These two scattering events are typically noticeable in GISAXS measurements [45, 46]. The second-order peaks derived from (11) reflection at q_z approximately 0.6 and 0.7 nm^{-1} were used for structure analysis because the primary peak from the (10) plans was partially invisible due to the detector gap. The magnitudes of the Bragg spot full widths at half maximum (FWHM) varied in the vicinity of the α_C, with larger FWHM values observed at smaller incident angles.

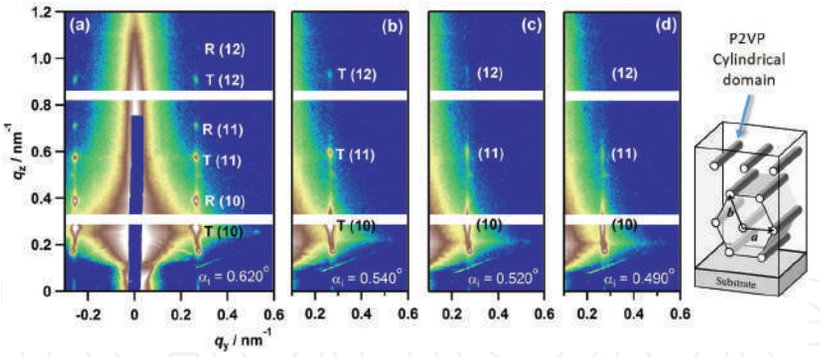

Figure 4. 2D-GISAXS (with λ of 5.166Å) patterns of S2VP-25k thin film annealed for 48 h at 170°C. (a) α_i was set at 0.62° ($\alpha_i > \alpha_C$), (b) 0.54°($\alpha_i > \alpha_C$), (c) 0.52°($\alpha_i < \alpha_C$), and (d) 0.49° ($\alpha_i > \alpha_C$). Schematic illustration represents the cross section of cylindrical microdomains in the thin film forming HEX aligned parallel to the substrate.

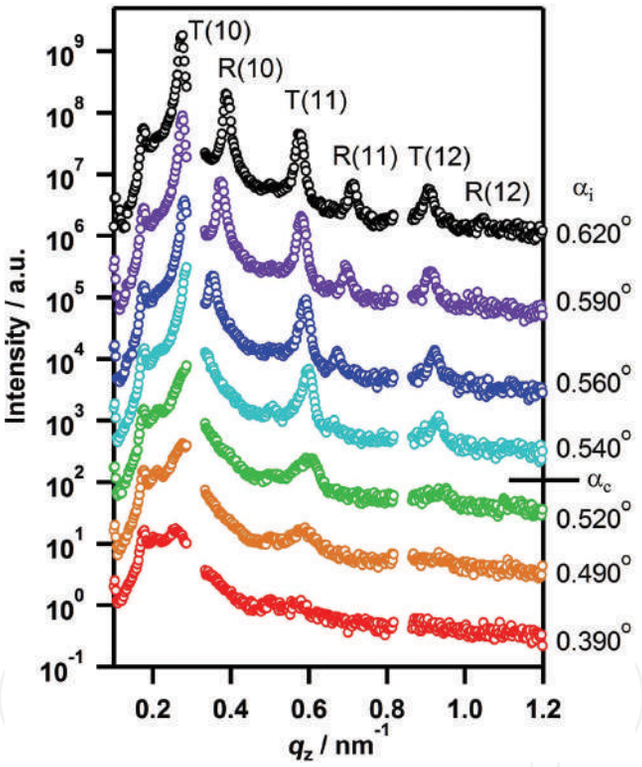

Figure 5. One-dimensional GISAXS profiles along q_z direction obtained by vertical cut at q_y = 0.26 mn^{-1}. Reprinted with permission from Saito et al. [57]. Copyright 2015 American Chemical Society.

The observed peak broadening can be interpreted by the change in the penetration depth. While generally such broadening can be understood by either the grain size effect and/or disordering of the crystal lattice, the FWHM in the q_y indicated no change irrespective of the incident angles as shown in **Figure 6**, eliminating the influence of the lattice disordering because the broadening was mainly seen in the q_z direction and the size effect was dominantly considered. Rather, the broadening in this case is because of the reduction in the size of the

http://dx.doi.org/10.5772/65090

observed region. The FWHM of a scattering peak depends on the grain size of a crystal, as expressed by the Laue function, $L(q)$

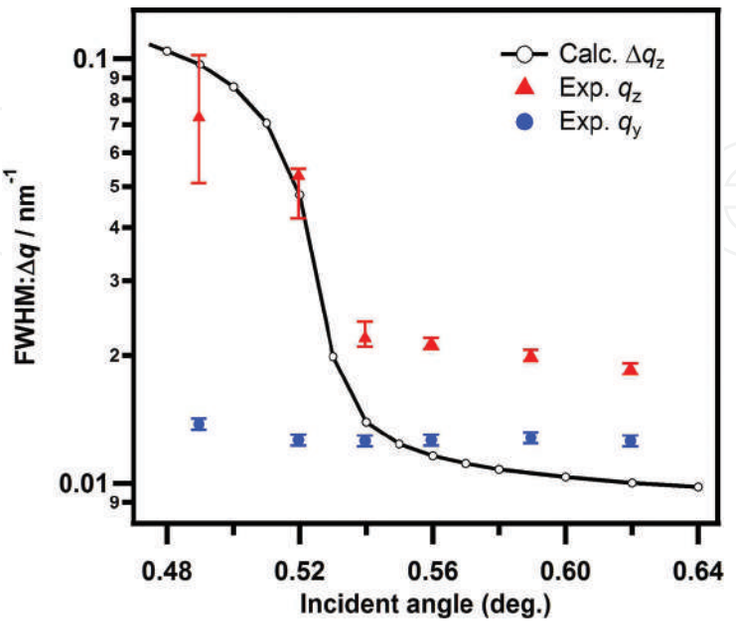

Figure 6. FWHM values of (11) Bragg spots obtained experimentally and calculated using Eq. (6). Reprinted with permission from Saito et al. [57]. Copyright 2015 American Chemical Society.

$$L(\boldsymbol{q}_z) = \sum_N \exp(iN\boldsymbol{q}_Z \cdot \boldsymbol{b}) = \frac{\sin\left[(N+1)\boldsymbol{q}_z \cdot \boldsymbol{b}/2\right]}{\sin\left[\boldsymbol{q}_z \cdot \boldsymbol{b}/2\right]}, \tag{5}$$

where N is the number of the reflection plane and $\boldsymbol{b}$ is the unit lattice vector related to z-direction normal to the surface. Here, the X-ray wave decays exponentially, and considering attenuation decay, the Laue function can be re-expressed as

$$L(\boldsymbol{q}_z) = \sum_N \frac{\sin[(N+1)q_z \cdot D_{01}/2]}{\sin[q_z \cdot D_{01}/2]} \exp\left[-\frac{\left(\frac{1}{2}+\frac{2}{3}N\right)D_{01}}{2\Lambda}\right], \tag{6}$$

where D_{01} is the periodicity of the (01) plane. Since the scattering intensity is proportional to the square of the Laue function, the FWHM can be calculated simply. The FWHM of the Bragg spots of the T (11) plane in q_z direction experimentally obtained is shown in **Figure 6**. The calculated values for FWHM in the q_z direction for the penetration depth Λ given by Eq. (2)

are also plotted in **Figure 6**. The change in the calculated width shows the same trend as the experimental results, indicating that the broadening of the Bragg spots can be explained by the size effect determined by the depth Λ. Thus, the observed region of GISAXS measurement can be controlled with the incident angle, enabling depth-resolved GISAXS.

When $\alpha_i < \alpha_C$, X-rays travel on the surface of the film and cannot propagate in the film. Only the evanescent wave can penetrate from the sample surface into the film. In this situation, the scattering peak α_z along the q_z direction is observed at the position given by the sum of the incident angle and the true scattering angle α_S derived from the period of the observed structure. Thus, α_s can be given as follows:

$$\alpha_S = \alpha_Z - \alpha_i \tag{7}$$

Using above relation, the true q_z value of the (11) spot can be estimated from the experimental peaks. On the other hand, in the case of $\alpha_i < \alpha_C$, an X-ray wave can travel into the film. The X-ray first refracts at the sample surface, goes through the film, is reflected by the interface between the sample and substrate, and finally exits out of the film surface with refraction as shown in **Figure 3**. Normally, some scattering events in GISAXS experiments occur because of the refracted X-rays at the polymer surface and reflected X-ray on the substrate surface, resulted in appearance of a number of scattering peaks. The scattering cross-section for GISAXS of the block copolymer thin film has been calculated within the framework of the distorted wave Born approximation (DWBA) [61]. Lee et al. [44], Yoon et al. [44, 45], and Busch et al. [46, 47] introduced the DWBA (or a combination of Bragg's and Snell's laws, refraction and reflection) to estimate the scattering peak positions. Scattering intensity due to the incident X-ray (transmission) and reflected X-ray (reflection) were pronounced. Debye-Scherrer rings of the block copolymer films with powder-like orientation of lamellar domains. The scattering peaks arising from transmitted and reflected X-rays at the substrate can be calculated following [53]

$$q_z = \frac{2\pi}{\lambda}\left[\sin\alpha_i + \left\{\sin^2\alpha_c + \left[\left\{\left(\frac{m\lambda}{D}\right)^2 - \left(\frac{q_y\lambda}{2\pi}\right)^2\right\}^{\frac{1}{2}} \mp (\sin^2\alpha_i - \sin^2\alpha_c)^{\frac{1}{2}}\right]^2\right\}^{\frac{1}{2}}\right], \tag{8}$$

where m represents the peak order, which is $3^{1/2}$ for the (11) plane in hexagonally packed cylindrical microdomains. The upper (−) and lower (+) branches in the equation indicate the Bragg diffraction of the transmitted and reflected X-rays, respectively. D is the characteristic length of the given plane. As for the (11) plane, Eq. (9) can be derived from Eq. (8) as follows:

$$q_z = \frac{2\pi}{\lambda}\left[\sin\alpha_i + \left\{\sin^2\alpha_c + \left[\frac{3\lambda}{2D} \mp (\sin^2\alpha_i - \sin^2\alpha_c)^{\frac{1}{2}}\right]^2\right\}^{\frac{1}{2}}\right], \tag{9}$$

http://dx.doi.org/10.5772/65090

where D corresponds to the D_{01} in this case. When the D_{01} was set to 18.8 nm, the DWBA calculation Eqs. (8) and (9) gave the best representation for all Bragg spots as shown by crosses in **Figure 7**.

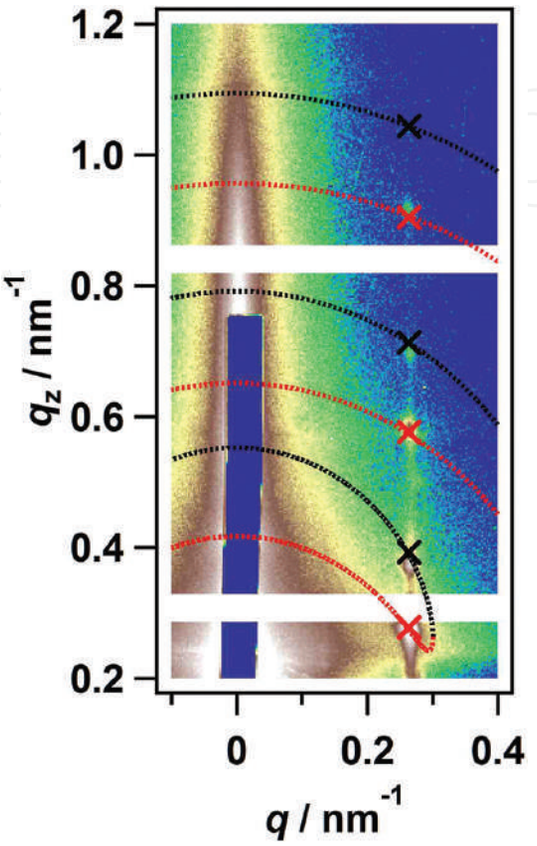

Figure 7. GISAXS patterns measured with tender X-ray (2.40 keV) at the angle of incidence 0.620. The dotted lines of the calculated Debye-Scherrer like rings from transmitted (red) and reflected (black) beams obtained using Eq. (8) as assuming the characteristic length $D_{\perp}$ (perpendicular to the surface) is smaller than the $D_{\parallel}$ (virtual parallel component). The $D_{\perp}$ corresponds to D_{01}. The crosses were obtained using Eqs. (8) and (9).

For GISAXS experiment in the soft X-ray region, the large curvature of the Ewald sphere may give rise to an apparent distortion of the GISAXS pattern when the measurements are conducted with a fixed angle of incidence and using the area 2D plane detector. Yamamoto et al. [62] discussed the effect of the Ewald sphere curvature and performed model calculations using DWBA [61]. At the lower energy of 1.77 keV, while the interparticle interference peaks extended and bent inward at large q_z, (approximately 2.0 nm^{-1}), no bending of the extended peaks was observed using hard X-rays. In the presence of the Ewald sphere curvature, the unmodified equation is no longer valid. In this study, Eq. (9) that had been developed for the hard X-ray regime to explain the experimental GISAXS pattern is confirmed to be valid for this observed q-range with tender X-ray regime 2.40 keV [57].

The lattice constant $\boldsymbol{b}$ associated with the direction perpendicular to the surface was slightly smaller than the lateral lattice constant $\boldsymbol{a}$. The hexagonal lattice was slightly deformed, in

particular, the nanocylinders were packed into distorted hexagonal lattice that was laterally elongated and/or vertically collapsed. The distorted hexagonal lattice in polymeric films has been often observed during the drying of solvents [63]. The lattice constant remained almost constant with respect to the depth. In contrast, the constant b and the angle ϕ between the lattice vectors increased with decreasing depth, i.e., approaching the surface, the lattice deformation was relaxed to a normal hexagonal lattice (**Figure 8**).

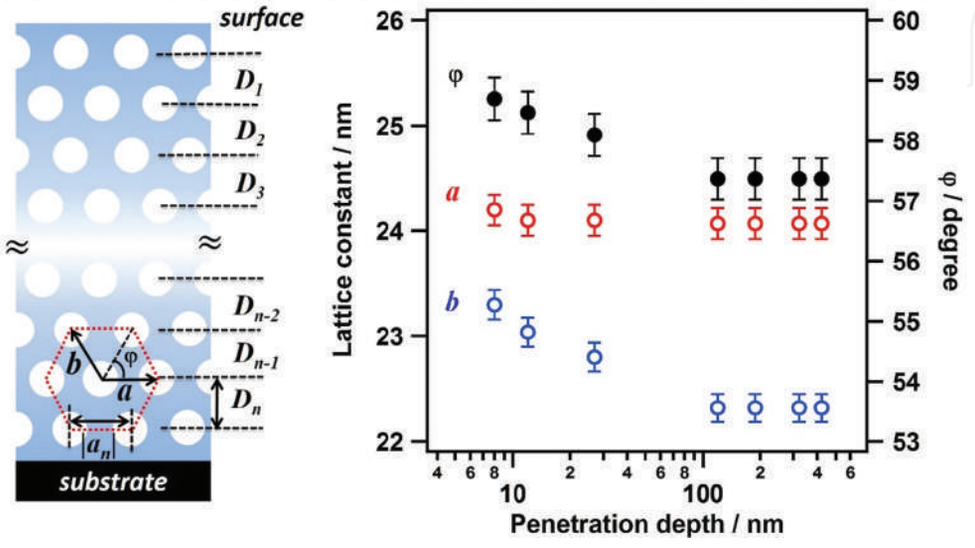

Figure 8. Lattice parameters plotted against the penetration depth (left). Right illustration indicates parallel-aligned cylindrical domains in thin film and the unit cell. The spacing D_n corresponds to the vertical distance neighboring planes (1). $|\boldsymbol{a}_n|$ and $|\boldsymbol{b}_n|$ represents the distance between neighboring cylindrical domains. The following relations were obtained by analysis; $D_1 > D_2 > D_3 > \cdots > D_c = \cdots = D_n$. $|\boldsymbol{a}_0| = |\boldsymbol{a}_1| = \cdots = |\boldsymbol{a}_n|$. $|\boldsymbol{a}_n| > |\boldsymbol{b}_n|$. Here, D_c means D_n reached constant value. Reprinted with permission from Saito et al. [57]. Copyright 2015 American Chemical Society.

3.2. Orientation and relaxation behaviors of lamellar microdomains of poly(methyl methacrylate)-b-poly(n-butyl acrylate) thin film [64]

In this section, we investigated the phase-separation behavior of poly (methyl methacrylate-b-n-butyl acrylate) (PMMA-PnBA) forming a lamellar structure aligned parallel to the substrate after appropriate thermal annealing with GISAXS measurement. The structure development through such as degree of the lamellar orientation and relaxation of the lamellar domain spacing was inquired. Also, the GISAXS with tender X-ray for depth-sensitive analysis was conducted to reveal that the difference of the lamellar domain spacing near the surface from the bulk.

To obtain a thin film of the block copolymer PMMA-b-PnBA (M_n = 32,000, M_w/M_n = 1.17, f_{PMMA} = 0.44), PMMA-b-PnBA in toluene (5 wt% polymer solution) was prepared. The thin film was obtained by spin cast on silicon wafer at 3000 rpm for 30 s. The thin films (thickness was 280±30 nm) were dried at room temperature, subsequently thermal annealing was performed at 160° for given time. GISAXS measurement utilizing hard X-ray and tender (soft) X-ray was performed. Hard X-ray GISAXS measurement was conducted at beamlines BL6A and BL10C

http://dx.doi.org/10.5772/65090

in Photon Factory of KEK, Tsukuba in Japan and BL03XU in SPring-8, Hyogo in Japan [65, 66] with wavelength of 0.15 (BL6A), 0.1488 (BL10C), and 0.1 nm (BL03XU), respectively. Tender X-ray GISAXS measurement was performed at BL15A2 in Photon Factory.

2D GISAXS (hard X-ray) patterns with various annealing times were shown in **Figure 9**. The pattern of as-spun sample (**Figure 9a**) was shaped like an ellipse, which might arise from kinetically frozen or poorly ordered structure. Partially intense scattering was observed at q_z of 0.25–0.28 nm^{-1} where was emphasized due to the so-called Yoneda peak, i.e., it did not indicate specific orientation, suggesting that no orientation of phase-separated structure of PMMA-b-PnBA appeared without thermal annealing. After the sample was thermally annealed for even 1 min, the scattering intensity around $q_y = 0$ (near the beam stop) grew. In addition, two clear ring-shaped scattering patterns like Debye-Scherrer rings were observed. Each scattering ring was arising from transmitted (denoted by T) and reflected (denoted by R) beams as described in previous section. The scattering intensity near beam stop became strong with annealing time. This change in GISAXS pattern indicates the growth of the parallel orientation of the lamellar microdomain. The development of the normalized scattering intensity [64] from parallel lamellar structure is shown in **Figure 10**. Orientation is nearly complete after annealing for 60 min. The GISAXS measurement gave structure information about domain spacing of the lamellar morphology. The domain spacing (D) of the lamellar structures aligned parallel to the surface was estimated. To determine the accurate domain spacing, the distorted wave Born approximation (DWBA) was applied for analysis of the GISAXS patterns. The experimentally estimated D values are also plotted as a function of the annealing time in **Figure 10**. The value of the D approached to the D_0 of the bulk sample (independently obtained to be 21.6 nm) with an increase in annealing time. The D of the parallel orientated structure was slightly smaller than D_0 even after 4 h thermal annealing, i.e., the spacing collapsed vertically. Consequently, the lamellar structure was deformed along the depth direction (similar phenomena as the previous section). Thermal annealing induced the relaxation of the domain spacing and it seems taking approximately more than 2 h to complete the relaxation of D (equals to the value of the bulk)

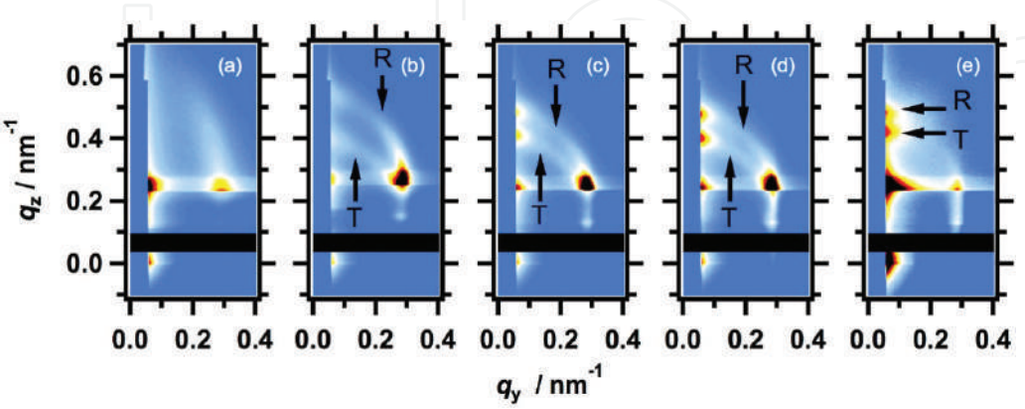

Figure 9. GISAXS patterns (hard X-ray, 1.488 Å) of PMMA-b-PnBA thin film (a) as cast and (b–e) as annealed at 160°C with given annealing time; (b) 1, (c) 3, (d) 5, and (e) 10 min. R and T denoted the scatterings from reflected and transmitted X-rays, respectively. Reprinted from Saito et al. [64]. Copyright Nature Publishing Group.

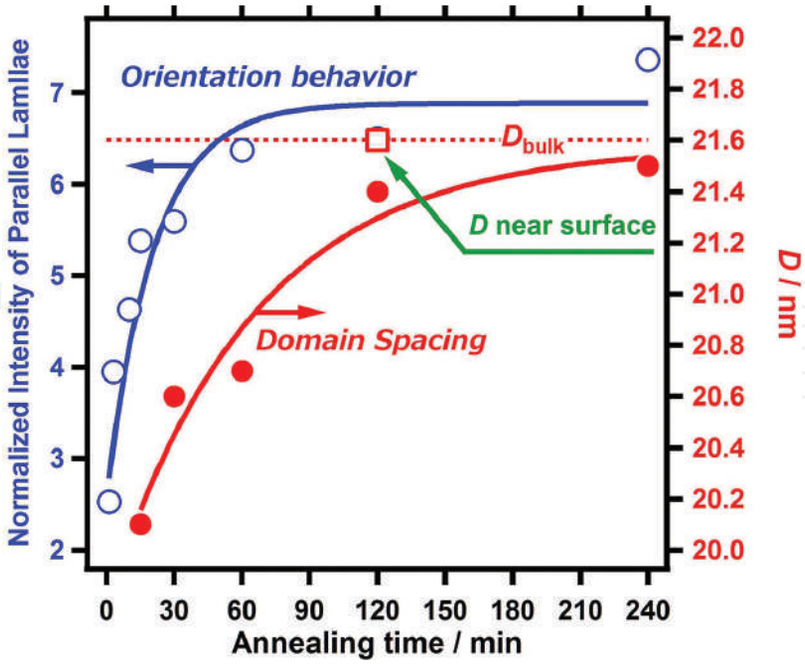

Figure 10. Time evolution of the orientation of the lamellar domain (open circles) and the relaxation of the lamellar *D* (filled circles). The solid lines were drawn as a guide to eyes. Dotted line shows the D_0 value of the bulk. Open square indicates the *D* value near the surface. Reprinted from Saito et al. [64]. Copyright Nature Publishing Group.

As is well known, preferential wetting of surface and substrate interfaces plays an important role of orientation in thin film [12, 17]. In this case, surface energies of PMMA, PnBA, and Si substrate are 41.1, 33.7, and 77.4 ± 0.5 mJ/m^2, respectively [16]. According to the surface free energies, it will be predicted that PMMA segregates to the surface of the silicon substrate, whereas PnBA segregates to air surface. As a result of preferential wetting, the parallel orientation of lamellar structure is induced at the surface and/or the polymer/substrate interfaces and the oriented lamellae propagate into the entire film [67]. In fact, XPS measurement proved that surface molar fractions of PnBA (within a few nanometers) were 80 mol% (repeat unit) in as-cast film and the PnBA component perfectly covered on the surface after thermal annealing with only 60 s. The segregation of each component, orientation of the lamellae, and relaxation of the domain spacing occurred in different time scale. It can be concluded that the PnBA first segregated at air surface within a minute after annealing (PMMA may segregated at the interface), second the microphase-separated structure aligned parallel to the surface, followed by relaxation of the domain spacing.

The polymer thin films have reported to have different mobility dependent on the local region, i.e., near the surface, inside, or near the polymer/substrate interface. It is quite intriguing to investigate that the depth dependence of structure difference exists, in other words, whether there are difference between the structure (orientation, morphology, d-spacing, etc.) in the vicinity of the surface and inside of the film, or not. The GISAXS measurements of PMMA-b-PnBA thin film thermally annealed for 2 h with tender X-ray was performed with various incident angles. As shown in **Figure 11(a)** and **(b)**, in the case of $\alpha_i < \alpha_c$, the scattering (marked arrows) of the lamellar structure oriented parallel to the substrate was considerably diffuse

http://dx.doi.org/10.5772/65090

and broaden, while in the case of $\alpha_i > \alpha_c$, the scattering became clear and sharp. The FWHM values of scattering peak (parallel lamellar domains) in the one-dimensional GISAXS profile obtained vertically cut at various incident angles can be simulated as the same manner of the size effect of measured region as discussed in the previous section (modified the Laue function). Thus, the penetration depth was controlled by changing the incident angle. At near the critical angle, the surface-sensitive measurement is possible as predicted from Eq. (2). The true q_z value of the oriented lamellar structure parallel to the substrate is estimated using the experimentally observed peaks, i.e. D near the surface can be estimated. At α_i of 0.525° (penetration depth Λ of 32.4 nm), D was obtained to be 21.6 nm which is equal to the D_0 value (21.6 nm) of the bulk sample. The value of D near the surface is slightly larger than the value 21.4 nm obtained from DWBA calculation (inside the whole film). This means that relaxation of the domain spacing near the film surface preceded that of the inside. According to previous reports, polymer chain near the surface indicates higher mobility (lower glass transition temperature or viscosity) [68–70]. Moreover, the lamellar structure started to orient from both the air/polymer and polymer/substrate interfaces, which was induced by segregation of one component in the BCP. Therefore, that the faster relaxation of the D of the lamellar structure near the surface was caused by the faster orientation and higher mobility in the vicinity of the surface.

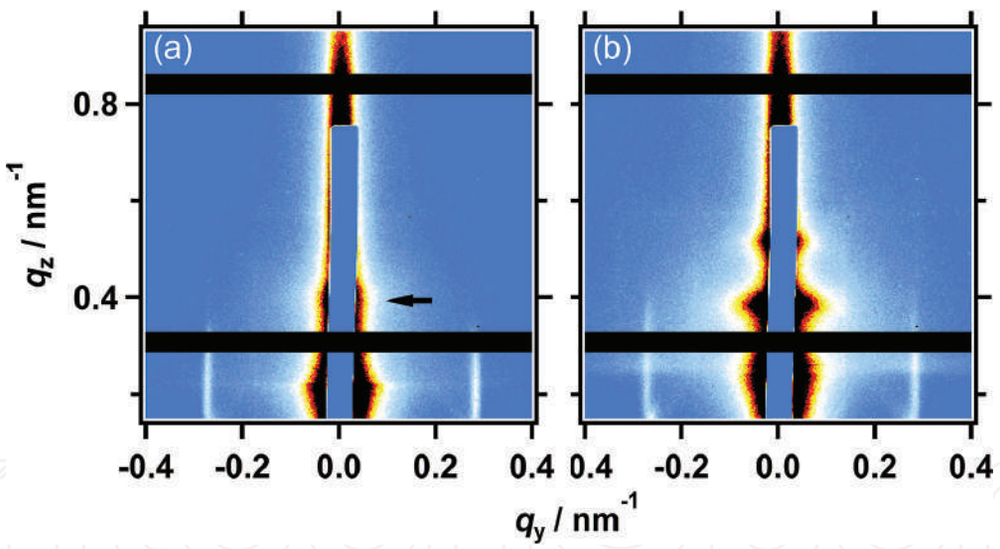

Figure 11. Tender X-ray (2.40 keV) GISAXS patterns of PMMA-b-PnBA thin films annealed at 160 °C for 2 hours at incident angles (a) 0.525° and (b) 0.625°. Reprinted from Saito et al. [64]. Copyright Nature Publishing Group.

3.3. Evaluation of mesogen orientation in thin films of polyacrylate with cyanobiphenyl side chain [71]

Understanding the orientation behavior of polymer chain in the vicinity of interfaces (both substrate and free surfaces) is of practical importance in organic thin film technologies such as coating and photoresisting processes. Thus, a large amount of fundamental knowledge has been ever accumulated. It has been broadly recognized that diverse physical properties of

polymeric materials in ultrathin film state are very different from those in the bulk state. Compared with the vast amount of studies for amorphous and crystalline (LC) polymers, studies on the anomaly in structure and orientation of side chain liquid crystalline polymers in ultrathin film states are rather unexplored. A large number of data related to mesogen orientation have been reported [72–78]. Accordingly, the side chain LC polymers are mostly aligned homeotropically [23, 79–81] The significant effect of the sample surface is apparent from the fact that the mesogen orientation changes to a planer orientation as the sample surface is covered by another layer or material [23, 82–84]. A cyanobiphenyl(CB)-containing polymethacrylate (PCBMA) exceptionally indicated the planar orientation regardless of the fact that the homologous polyacrylate (PCBA) oriented homeotropically [33]. This unexpected orientation behavior is responsible for the difference in the main chain rigidity (but still no rational explanation). In these contexts, the investigation to reveal in detail the orientation of PCBA is proceeded by the GISAXS measurements by systematically changing the film thickness. Additionally, GISAXS with hard (8.05 keV) and tender (2.30 keV) X-rays were carried out.

The side chain LC polymer PCBA (chemical structure shown in **Figure 12**, M_n = 12,000, M_w/M_n = 1.83, glassy state – 13°C (T_g: glass-transition temperature)–smectic A - 95°C (T_i: isotropization temperature)) films on quartz plates were prepared by spin-casting from 0.12–3.0 wt % chloroform solutions to make different thickness samples. The spin-cast film samples were annealed at 135 °C, cooled to a target temperature, kept for 10 min, and then subjected to the measurements. The layer spacing of the smectic A of LC polymers in the bulk was estimated to be 4.6 nm (SAXS). GI-SAXS experiments with hard X-rays (Cu Kα radiation (λ = 0.154 nm)) were conducted with a FR-E X-ray diffractometer equipped with two-dimensional imaging plate R-AXIS IV detector (Rigaku). GI-SAXS experiments using low-energy X-rays were performed at BL-15A2 [60] at the Photon Factory, KEK, Tsukuba, Japan. Experimental details of the GI-SAXS measurements were described in previous sections.

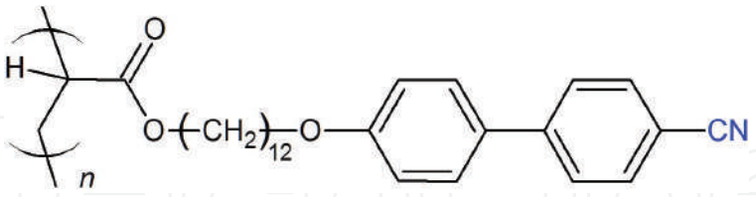

Figure 12. Chemical structure of the side chain LC polymer.

Figure 13 indicates GI-SAXS data measured with hard X-rays (λ = 0.154 nm) for 30 nm thick at 80 °C. For 140 nm thick film, the scattering peaks corresponding to d (smectic layer) = 4.6 nm (100) and 2.3 nm (200) were clearly seen in both out-of-plane and in-plane directions. The intensity of the peaks in the out-of-plane direction was significantly small in 30 nm thick film (as peaks was weakly shown in 1D profile), and no peaks were essentially recognized for 15 nm thick film, although those in the in-plane direction were clearly seen. These results evidently indicate the coexistent of planarly and homeotropically oriented CB in the films with film thickness greater than 30 nm, and that the CB mesogens were oriented only planarly at 15 nm thickness.

http://dx.doi.org/10.5772/65090

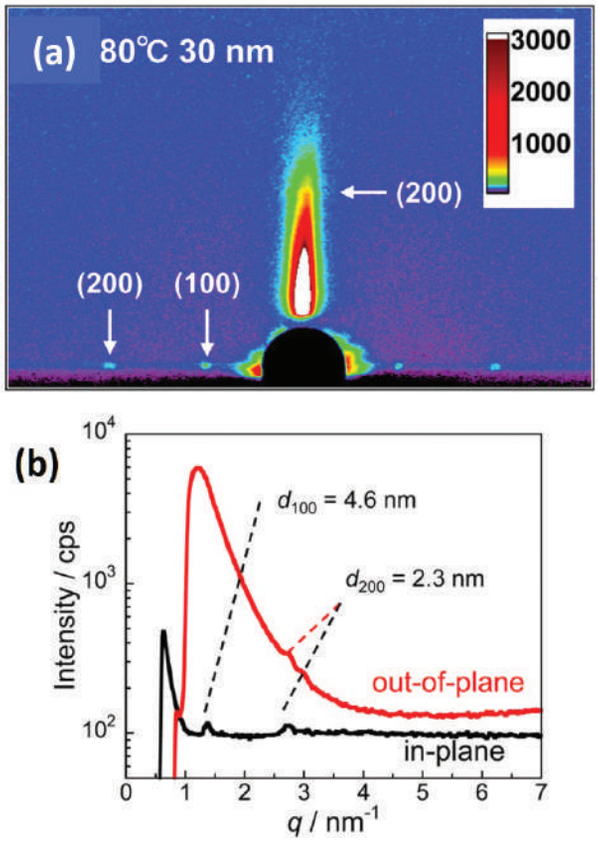

Figure 13. 2D GI-SAXS (Cu Kα) patterns (a) of PCBA films with a thickness of 30 nm at 80 °C. Lower figure (b) indicates 1D intensity profiles (black: in-plane; red: out-of-plane directions). Reprinted with permission from Tanaka et al. [71]. Copyright 2016 American Chemical Society.

GI-SAXS measurements with synchrotron tender X-rays (λ = 0.539 nm, 2.30 keV) were achieved at various α_i. **Figure 14** shows the 2D GI-SAXS images for 30 nm thick film at room temperature. The CB mesogens at this thickness as mentioned before are oriented both in the homeotropic and planar directions (coexistence). The α_c in this sample was estimated at about 0.54° for this X-ray energy. Under conditions of $\alpha_i < \alpha_c$ (α_c is about 0.54° for 2.30 keV), the scattering signals in the thin film was observed only the out-of-plane direction as shown in **Figure 14a** and **b**, where Λ is estimated as in the range less than 10–20 nm in these experimental conditions. It is apparently indicated that the CB mesogens adopt homeotropic orientation in the free surface region. When $\alpha_i > \alpha_c$, the out-of-plane scatterings were split into double peaks in the q_z direction as shown in **Figure 14c–e**. The split double peaks originate from the transmitted X-ray through the film and then reflected on the substrate [44]. Hence, the high q_z peak of the double peaks can be assigned to the scattering from the reflection path on the film surface. The split spots means that the X-ray beam actually travelled through the overall film thickness and reached the sample/substrate interface. When $\alpha_i > \alpha_c$ (Λ > 100 nm), the peaks appeared in-plane direction due to the planar orientation were clearly observed as shown in **Figure 14d–f** with arrows. These signals undoubtedly originate from the mesogens near the polymer/substrate interface.

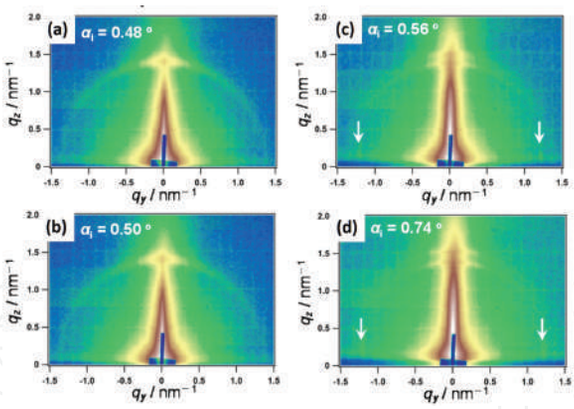

Figure 14. Two-dimensional GI-SAXS patterns for PCBA thin film with 30 nm thickness using tender X-rays (0.539 nm). Measurements were conducted at α_i = 0.48 (Λ = 11 nm) (a), 0.50 (Λ = 16 nm) (b), 0.56 (Λ = 167 nm) (c), 0.74 (Λ = 453 nm), and (d). Note that α_c (0.54°) is positioned between (b) and (c). Reprinted with permission from Tanaka et al. [71]. Copyright 2016 American Chemical Society.

From the overall data of UV-vis absorption spectroscopic [71] and the GISAXS measurements utilizing hard and tender X-rays, the orientation structural models of CB mesogens in PCBA thin films are schematically illustrated in **Figure 15**. In thick films with 140 nm, the CB mesogens are almost aligned homeotropically. However, a considerable number of the CB mesogens planarly anchored exist near the substrate (polymer/substrate interface) as revealed by GI-SAXS measurements with hard X-rays (**Figure 13**). At a thickness of 30 nm, the amounts of homeotropically and planarly oriented CB mesogens is comparable, where depth-resolved information is obtained by GI-SAXS with tender X-ray experiments (**Figure 14**). In the film thickness of 10–15 nm, the CB mesogens adopt almost planar alignment. When the film becomes further thinner from the critical level of 7 nm, the planar alignment near the surface disappears where the liquid crystal structuring (antiparallel packing of the CB mesogens) is lost.

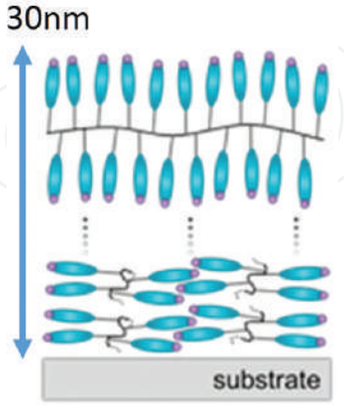

Figure 15. Schematic illustration of orientation of the CB mesogens in films with film thickness 30 nm. Purple circles indicate the cyano group at the terminal of mesogen. Note that the antiparallel interactions (LC structuring) are kept among the CB mesogens at thickness above 10–15 nm. Such LC structuring is lost at thickness of 7 nm. Reprinted with permission from Tanaka et al. [71]. Copyright 2016 American Chemical Society.

http://dx.doi.org/10.5772/65090

4. Grazing-incidence resonant soft X-ray scattering [50]

The GI-RSoXS is a novel technique, which is in particular suited for more complex system such as multicomponent block copolymer and polymer blend films. Resonant soft X-ray scattering has already been successful for probing morphology and spatial structure in organic photovoltaic (OPV) systems [85, 86] and triblock copolymer system [87]. GI-RSoXS allows for detecting near surface and inner structure separately at fixed incident angle by tuning X-ray photon energy because the penetration depth of the X-ray beam is drastically affected by the change in X-ray photon energy across the adsorption edge. Adsorption *K* edge for organic materials composed of mainly carbon, nitrogen, and oxygen are 284, 409, and 543 eV. The fine structure of the adsorption edge can be utilized in GISAXS measurements. Near edge X-ray adsorption fine structure (NEXAFS) spectrum needs to be probed for the polymeric materials in order to estimate the complex refractive index of X-ray that becomes important for depth-sensitive and component sensitive analyses. Typically, the NEXAFS spectra of polymers, which have low contrast in the real part of the refractive index in the hard photon energy regime, indicate considerable differences in the soft X-ray regime. In this section, investigation of nanostructure in the polymer blend thin film, poly(3-hexylthiophene) (P3HT) and poly[5-(2-ethylhexyloxy)-2-methoxycyanoterephtalylidene] (MEH-CN-PPV), is introduced as an example of GI-RSoXS experiment carried out by Ruderer et al. [50].

GI-RSoXS measurements with soft X-ray were conducted at the synchrotron beamline 11.0.1.2 of the advanced light source (ALS) at the LBNL in Berkeley (USA) [88, 89]. Due to the high adsorption of soft X-ray in air, full setup (sample and X-ray detector) was kept in high vacuum. The energy of X-ray was used in the range of 280–320 eV (λ: 4.4–3.9 nm). Sample-to-detector was 18.5 cm that was sufficient for detecting length scale in the range from 21 nm to a few micron meters. An incident angle $\alpha_i = 2°$, which is near the critical angle α_C of 2.3° for 280eV and 1.5° for 283 eV. The both polymers (P3HT and MEH-CN-PPV) were dissolved in chloroform. The thin film of polymer blend was prepared by spin coating from the solution; the thickness was controlled to be about 70 nm. The films were annealed at 200 °C for 10 min in air without degradation. The NEXAFS spectroscopy measurement was conducted for taking the wavelength dependent refractive index ($n = 1 - \delta + i\beta$) of polymers used here for electromagnetic radiation near the adsorption edge. NEAXFS spectra were also obtained at the same beam line of the ALS. The sample environment is identical to the GI-RSoXS setup. The polymer thin films were prepared on silicon nitride membranes and measured in transmission geometry. The adsorption part β of the refractive index was obtained through Beer's law. The real part δ of the refractive index was calculated from the β using Kramers-Krongis relation.

Figure 16a shows the X-ray energy dependence of the dispersion δ and the adsorption β of P3HT and MEH-CN-PPV homopolymer. The spectra of respective homo polymers are different. NEXAFS spectra of the blend system with different blend ratio can be obtained by a linear superposition of the spectra of P3HT and MEH-CN-PPV homopolymer weighted with the corresponding blend ratio. The dispersion δ spectra of P3HT and MEH-CN-PPV reveal positive and negative values and differ strongly depending X-ray energy. Therefore, the scattering contrast depends on the X-ray energy. Using the adsorption β spectra, the

penetration depth Λ of the soft X-rays into the blend film is calculated as shown in **Figure 16b**. **Figure 17** indicates the GI-RSoXS patterns of as spun P3HT/MEH-CN-PPV bulk heterojunction films with a P3HT content of 70 wt% for different energies from 280 to 289 eV (wavelength of X-rays from 4.43 to 4.29 nm). Although the wavelength is varied by only 3%, the scattering patterns significantly change. For energy below 284 eV, an intensity oscillation in vertical direction is observed, which comes from the correlated roughness originating from the interference of scattered X-rays from different interfaces. The correlated roughness vanishes with increasing energies of the X-rays. It indicates no scattering signal from the substrate interface is detected and X-ray penetrates near the surface as shown in **Figure 17**. The low scattering intensity of GI-RSoXS at 284 eV (**Figure 17c**) is due to the very low incident intensity at this energy. The reduction of the intensity at 286 eV (**Figure 17e**) can be ascribed to the significant low contrast between P3HT and MEH-CN-PPV at this energy. Thus, the surface structure is accessible at 286 eV. The change in the total scattered intensity was attributed to the changed contrast conditions from the contrast variation.

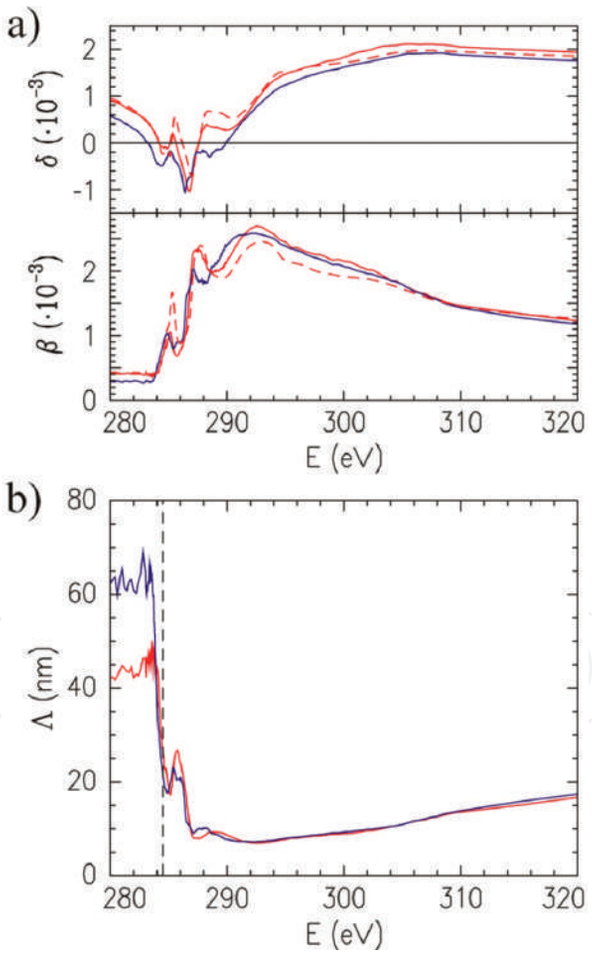

Figure 16. (a)Dispersion δ and the absorption β of P3HT (red solid lines) and MEH-CN-PPV (blue solid lines) as a function of the X-ray energy. For comparison, the calibrated P3HT spectra (dashed lines) from the database [90] are drawn. (b) Penetration depth of X-ray of P3HT (red) and MEH-CN-PPV (blue) as a function of X-ray energy. Reprinted with permission from Ruderer et al. [50]. Copyright 2016 American Chemical Society.

http://dx.doi.org/10.5772/65090

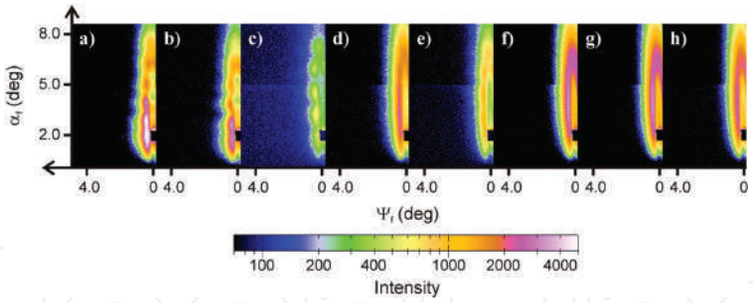

Figure 17. Two-dimensional GI-RSoXS patterns of as-spun P3HT: MEH-CN-PPV film with a P3HT content of 70 wt% with different X-ray energies. The X-ray energy: (a) 282, (b) 283, (c) 284, (d) 285, (e) 286, (f) 287, (g) 288, and (h) 289 eV. Copyright American Chemical Society, Ruderer et al. [50].

Author details

Katsuhiro Yamamoto

Address all correspondence to: yamamoto.katsuhiro@nitech.ac.jp

Department of Life Science and Applied Chemistry, Frontier Research Institute for Materials Science, Field of Soft Materials, Graduate School of Engineering, Nagoya Institute of Technology, Nagoya, Japan

References

[1] Zhang, Q.; Cirpan, A.; Russell, T. P.; Emrick, T. Donor-acceptor poly (thiophene-block-perylene diimide) copolymers: synthesis and solar cell fabrication. Macromolecules. 2009;42:1079–1082.

[2] Sun, S. S.; Zhang, C.; Ledbetter, A.; Choi, S.; Seo, K.; Bonner, C. E. Jr; Dress, M; Sariciftchi, N. S. Photovoltaic enhancement of organic solar cells by a bridged donor-acceptor block copolymer approach. Appl. Phys. Lett. 2007;90:043117.

[3] Crossland, E. J. W.; Kamperman, M.; Nedelcu, M.; Ducati, C.; Wiesner, U.; Smilges, D.-M.; Toombes, G. E. S.; Hilmyer, M. A.; Ludwigs, S.; Steiner, U.; Naith, H. J. A bicontinuous double gyroid hybrid solar cell. Nano Lett. 2008;9:2807–2812.

[4] Singh, G.; Yager, K.; Berry, B.; Kim, H.-C.; Karim, A. Dynamic thermal field-induced. ACS Nano. 2012;6:10335–10342.

[5] Luo, Y.; Montarnal, D.; Kim, S.; Shi, W.; Barteau, K. P.; Pester, C. W.; Hustad, P. D.; Christianson, M. D.; Fredrickson, G. H.; Kramer, E. J.; Hawker, C. J. Poly(dimethylsi-

loxane-b-methyl methacrylate): a promising candidate for sub-10 nm patterning. Macromolecules. 2015;48:3422–3430.

[6] Gu, W.; Zhao, H.; Wei, Q.; Coughlin, E. B.; Theato, P.; Russell, T. P. Line patterns from cylinder-forming photocleavable block copolymers. Adv. Mater. 2013;25:4690–4695.

[7] Wan, L.-S.; Li, J.-W.; Ke, B.-B.; Xu, Z.-K. Ordered microporous membranes template by breath figures for size-selective separation. J. Am. Chem. Soc. 2012;134:95098.

[8] Jeong, U.; Ryu, D. Y.; Kim, J. K.; Kim, D. H.; Wu, X.; Russell, T. P. Precise control of nanopore size in thin film using mixtures of asymmetric block copolymer and homopolymer. Macromoelcules. 2003;36:10126–10129.

[9] Matsen, M. W.; Schick, M. Stable and unstable phases of a diblock copolymer melt. Phys. Rev. Lett. 1994;72:2660–2663.

[10] Stein, G. E.; Kramer, E. J.; Li, X.; Wang, J. Layering transitions in thin films of spherical-domain block copolymers. Macromolecules. 2007;40:2453–2460.

[11] Suh, H. S.; Kang, H.; Nealey, P. F.; Char, K. Thickness dependence of neutral parameter windows for perpendicularly oriented block copolymer thin films. Macromolecules. 2010;43:4744–4751.

[12] Albert, J.; Epps, T. H. Self-assembly of block copolymer thin films. Mater. Today. 2010;13:24–44.

[13] Jung, J.; Park, H. W.; Lee, S.; Lee, H.; Chang, T.; Matsunaga, T.; Jinnai, H. Effect of film thickness on the phase behaviors of diblock copolymer thin film. ACS Nano. 2010;4:3109–3116.

[14] Luo, M.; Seppala, J. E.; Albert, J. N. L.; Lewis, R.; Mahadevapuram, N.; Stein, G. E.; Epps, T. H. Manipulating nanoscale morphologies in cylinder-forming poly (styrene-b-isoprene-b-styrene) thin films using film thickness and substrate surface chemistry gradient. Macromolecules. 2013;45:1803–1811.

[15] Kim, S. O.; Solak, H. H.; Stoykovich, M. P.; Ferrier, N. J.; Pablo, J. J.; Nealey, P. F. Epitaxial self-assembly of block copolymers on lithographically defined nanopatterned substrates. Nature. 2003;424:411–414.

[16] Shelton, C. K.; Epps, T. H. Decoupling substrate surface interactions in block polymer thin film self-assembly. Macromolecules. 2015;48:4572–4580.

[17] Mansky, P.; Liu, Y.; Huang, E.; Russell, T. P.; Hawker, C. Controlling polymer-surface interactions with random copolymer brushes. Science. 1997;275:1458–1460.

[18] Park, S.; Lee, D. H.; Xu, J.; Kim, B.; Hong, S. W.; Jeong, U.; Xu, T.; Russell, T. P.. Macroscopic 10-terabit–per–square-inch arrays from block copolymers with lateral order. Science. 2009;323:1030–1033.

[19] Sivaniah, E.; Hayashi, Y.; Iino, M.; Hashimoto, T.; Fukunaga, K. Observation of perpendicular orientation in symmetric diblock copolymer thin films on rough substrates. Macromolecules. 2003;36:5894–5896.

[20] Qiang, Z.; Zhang, L.; Stein, G. E.; Cavicchi, K. A.; Vogt, B. D. Macromolecules. Unidirectional Alignment of Block Copolymer Films Induced by Expansion of a Permeable Elastomer during Solvent Vapor Annealing. 2014;47:1109–1116.

[21] Xu, T.; Zvelindovsky, A. V.; Sevink, G. J. A.; Lyakhova, K. S.; Jinnai, H.; Russell, T. P. Electric field alignment of asymmetric diblock copolymer thin films. Macromolecules. 2005;38:10788–10798.

[22] Gopinadhan, M.; Majewski, P. W.; Osuji, C. O. Macromolecules. 2010;43:3286–3293.

[23] Fukuhara, K.; Nagano, S.; Hara, M.; Seki, T. Free-surface molecular command. Nat. Commun. 2014;5:3320.

[24] Sano, M.; Nakamura, S.; Hara, M.; Nagano, S.; Shinohara, Y.; Amemiya, Y.; Seki, T. Pathways toward photoinduced alignment switching in liquid crystalline block copolymer films. Macromolecules. 2014;47:7178–7186.

[25] Cui, G.; Ohya, S.; Matsutani, T.; Nagano, S.; Dohi, T.; Nakamura, S.; Sakurai, S.; Miyazaki, T.; Yamamoto, K. Perpendicular orientation of sub-10 nm channels in polystyrene-b-poly(4-hydroxyl styrene)/PEG oligomer blend thin films. Nanoscale. 2013;5:6713–6719.

[26] Gu, W.; Xu, J.; Kim, J.-K.; Hong, S. W.; Wei, X.; Yang, X.; Lee, K. Y.; Kuo, D. S.; Xiao, S.; Russell, T. P. Solvent-assisted directed self-assembly of spherical microdomain block copolymers to high areal density arrays. Adv. Mater. 2013;25:3677–3682.

[27] Kim, S. H.; Misner, M. J.; Yang, L.; Gang, O.; Ocko, B. M.; Russell, T. P. Salt complexation in block copolymer thin films. Macromolecules. 2013;39:8473–8479.

[28] Jeong, J. W.; Park, W. I.; Kim, M.-J.; Ross, C. A.; Jung, Y. S. Highly tunable self-assembled nanostructures from a poly(2-vinylpyridine-b-dimethylsiloxane) block copolymer. Nano Lett. 2011;11:4095–4101.

[29] Park, S.; Wang, J.-Y.; Kim, B.; Xu, J.; Russell, T. P. A simple route to highly oriented and ordered nanoporous block copolymer templates. ACS Nano. 2008;2:766–772.

[30] She, M.-S.; Lo, T.-Y.; Ho, R.-M. Long-range ordering of block copolymer cylinders driven by combining thermal annealing and substrate functionalization. ACS Nano. 2013;7:2000–2011.

[31] Tang, C.; Wu, W.; Smilgies, D. M.; Matyjaszewski, K.; Kowalewski, T. J. Am. Chem. Soc. Robust Control of Microdomain Orientation in Thin Films of Block Copolymers by Zone Casting. 2011;133:11802–11809.

[32] De Rosa, C.; Park, C.; Thomas, E. L.; Lotz, B. Nature. Microdomain patterns from directional eutectic solidification and epitaxy. 2000;405:433–437.

[33] Reiter, G.; Castelein, G.; Hoerner, P.; Riess, G.; Blumen, A.; Sommer, J. U. Phys. Rev. Lett. Nanometer-Scale Surface Patterns with Long-Range Order Created by Crystallization of Diblock Copolymers. 1999;83:3844–3847.

[34] Niihara, K.; Matsuwaki, U.; Torikai, N.; Atarashi, H.; Tanaka, K.; Jinnai, H. Macromolecules. A Novel Structural Analysis for a Cylinder-Forming Block Copolymer Thin Film Using Neutron Reflectivity Aided by Transmission Electron Microtomography. 2007;40:6940–6946.

[35] Yokoyama, H.; Kramer, E. J.; Rafailovich, M. H.; Sokolov, J.; Schwarz, S. A. Macromolecules. Structure and Diffusion of Asymmetric Diblock Copolymers in Thin Films: A Dynamic Secondary Ion Mass Spectrometry Study. 1998;31:8826–8830.

[36] Ninomiya, S.; Ichiki, K.; Yamada, H.; Nakata, Y.; Seki, T.; Aoki, T.; Matsuo, J. Rapid Commun. Mass Spectrom. 2009;23:1601.

[37] Terlier, T.; Tiron, R.; Gharbi, A.; Chevalier, X.; Veillerot, M.; Martinez, E.; Barnes, J. P. Surf. Interface Anal. 2014;46:83–91.

[38] Gilbert, J. B.; Rubner, M. F.; Cohen, R. E. Proc. Natl. Acad. Sci. U. S. A. 2013;110:6651–6656.

[39] Gilbert, J. B.; Luo, M.; Shelton, C. K.; Rubner, M. F.; Cohen, R. E.; Epps, T. H. III . ACS Nano. 2015;9:512–520.

[40] Mayes, A. M.; Russell, T. P.; Bassereau, P.; Baker, S. M.; Smith G. S. Macromolecules. 1994;27:749–755.

[41] Koneripalli, N.; Singh, N.; Levicky, R.; Bates, F. S.; Gallagher, P. D.; Satija, K. Macromolecules. 1995;28:2897–2904.

[42] Müller-Buschbaum, P. Anal. Bioanal. Chem. 2003;376:3–10.

[43] Roth, S. V.; Burghammer, M.; Riekel, C.; Bushbaum, P. M. Appl. Phys. Lett. 2003;82:1935–1937.

[44] Lee, B.; Park, I.; Yoon, J.; Park, S.; Kim, J.; Kim, K. W.; Chang, T.; Ree, M.. Macromolecules. 2005;38:4311–4323.

[45] Yoon, J.; Yang, S. Y.; Lee, B.; Joo, W.; Heo, K.; Kim, J. K.; Ree, M. J. Appl. Crystallogr. 2007;40:305–312.

[46] Busch, P.; Smilgies, D. M.; Rauscher, M.; Posselt, D.; Papadakis, C. M. J. Appl. Crystallogr. 2006;39:433–442.

[47] Busch, P.; Posselt, D.; Smilgies, D. M.; Rauscher, M.; Papadakis, C. M. Macromolecules. 2007;40:630–640.

[48] Okuda, H.; Takeshita, K.; Ochiai, S.; Sakurai, S.; Kitajima, Y. J. Appl. Crystallogr. 2011;44:380–384.

[49] Wernecke, J.; Okuda, H.; Ogawa, H.; Siewert, F.; Krumrey, M. Macromolecules. 2014;47:5719–5727.

[50] Ruderer, M. A.; Wang, C.; Schaible, E.; Hexemer, A.; Xu, T.; Müller-Buschbaum, P. Macromolecules. 2013;46:4491–4501.

[51] Müler-Buschbaum, P.; Maurer, E.; Bauer, E.; Cubitt, R. Langmuir. 2006;22:9295–9303.

[52] Müller-Buschbaum, P.; Schulz, L.; Metwalli, E.; Moulin, J.-F.; Cubitt, R. Langmuir. 2009;25:4235–4242.

[53] Busch, P.; Rauscher, M.; Moulin, J.-F.; Müller-Buschbaum, P. J. Appl. Crystallogr. 2011;44:370–379.

[54] Müller-Buschbaum, P.; Schulz, L.; Metwalli, E.; Moulin, J.-F.; Cubitt, R. Langmuir. 2008;24:7638–7644.

[55] Müller-Buschbaum, P.; Kaune, G.; Haese-Seiller, M.; Moulin, J.-F. J. Appl. Crystallogr. 2014;47:1228–1237.

[56] Müller-Buschbaum P. Grazing incidence small-angle neutron scattering: challenges and possibilities. Polymer J. 2013;45:34–42. DOI: 0.1038/pj.2012.190

[57] Saito, I.; Miyazaki, T.; Yamamoto, K. Depth-resolved structure analysis of cylindrical microdomain in block copolymer thin film by grazing-incidence small-angle X-ray scattering utilizing low-energy X-rays. Macromolecules. 2015;48:8190−8196. DOI: 10.1021/acs.macromol.5b01883

[58] Yin, J.; Yao, X.; Liou, J.-Y.; Sun, W.; Sun, Y.-S.; Wang, Y. ACS Nano. 2013;7:9961–9974.

[59] Kim, J.; Lew, B.; Kim, W. S. Nanoscale Res. Lett. 2011;6:616.

[60] Photon-Factory KEK. BL-15A2: High-brilliance Small-Angle X-ray Scattering beamline [Internet]. Available from: http://pfwww.kek.jp/saxs/beamline/bl15a2.html

[61] Sinha, S. K.; Sirota, E. B.; Garoff, S. Phys. Rev. B: Condens. Matter. Mater. Phys. X-ray and neutron scattering from rough surfaces. 1988;38:2297–2311.

[62] Yamamoto, T.; Okuda, H.; Takeshita, K.; Usami, N.; Kitajima, Y.; Ogawa, H. J. Synchrotron Radiat. Grazing-incidence small-angle X-ray scattering from Ge nanodots self-organized on Si(001) examined with soft X-rays. 2014;21:161−164.

[63] Tokarev, I.; Krenek, R.; Burkov, Y.; Schmeisser, D.; Sidorenko, A.; Minko, S.; Stamm, M. Macromolecules. Microphase Separation in Thin Films of Poly(styrene-block-4-vinylpyridine) Copolymer−2-(4′-Hydroxybenzeneazo)benzoic Acid Assembly. 2005;38:507−516.

[64] Saito, I.; Shimada, D.; Aikawa, M.; Miyazaki, T.; Shimokita, K.; Takagi, H.; Yamamoto, K. Orientation and relaxation behaviors of lamellar microdomains of poly(methyl methacrylate)-b-poly(n-butyl acrylate) thin films as revealed by grazing-incidence small-angle X-ray scattering. Polymer J. 2016;48:399–406. DOI: 10.1038/pj.2016.2

[65] Ogawa, H.; Masunaga, H.; Sasaki, S.; Goto, S.; Tanaka, T.; Seike, T.; Takahashi, S.; Takeshita, K.; Nariyama, N.; Ohashi, H.; Ohata, T.; Furukawa, Y.; Matsushita, T.; Ishizawa, Y.; Yagi, N.; Takata, M.; Kitamura, H.; Takahara, A.; Sakurai, K.; Tashiro, K.; Kanaya, T.; Amemiya, Y.; Horie, K.; Takenaka, M.; Jinnai, H.; Okuda, H.; Akiba, I.; Takahashi, I.; Yamamoto, K.; Hikosaka, M.; Sakurai, S.; Shinohara, Y.; Sugihara, Y.; Okada, A. Experimental station for multiscale surface structural analyses of oft-material films at SPring-8 via a GISWAX/GIXD/XR-integrated system. Polymer J. 2012;45:109–116.

[66] Masunaga, H.; Ogawa, H.; Takano, T.; Sasaki, S.; Goto, S.; Tanaka, T.; Seike, T.; Takahashi, S.; Takeshita, K.; Nariyama, N.; Ohashi, H.; Ohata, T.; Furukawa, Y.; Matsushita, T.; Ishizawa, Y.; Yagi, N.; Takata, M.; Kitamura, H.; Sakurai, K.; Tashiro, K.; Takahara, A.; Amamiya, Y.; Horie, K.; Takenaka, M.; Kanaya, T.; Jinnai, H.; Okuda, H.; Akiba, I.; Takahashi, I.; Yamamoto, K.; Hikosaka, M.; Sakurai, S.; Shinohara, Y.; Okada, A.; Sugihara, Y. Multipurpose soft-material SAXS/WAXS/GISAXS beamline at SPring-8. Polymer J. 2011;43:471–477.

[67] Russell, T. P.; Coulon, G.; Deline, V. R.; Miller, D. C. Characteristics of the surface-induced orientation for symmetric diblock PS/PMMA copolymers. Macromolecules. 1989;22:4600–4604.

[68] Kawaguchi, D.; Tanaka, K.; Kajiyama, T.; Takahara, A.; Tasaki, S. Mobility gradient in surface region of monodisperse polystyrene films. Macromolecules. 2003;36:1235–1240.

[69] Kajiyama, T.; Tanaka, K.; Takahara, A. Depth dependence of the surface glass transition temperature of a poly (styrene-block-methyl methacrylate) diblock copolymer film on the basis of temperature-dependent x-ray photoelectron spectroscopy. Macromolecules. 1995;28:3482–3484.

[70] Inoue, R.; Kawashima, K.; Matsui, K.; Nakamura, M. Interfacial properties of polystyrene thin films as revealed by neutron reflectivity. Phys. Rev. E. 2011;84:031802.

[71] Tanaka, D.; Mizuno, T.; Hara, M.; Nagano, S.; Saito, I.; Yamamoto, K.; Seki, T. Evaluations of mesogen orientation in thin films of polyacrylate with cyanobiphenyl side chain. Langmuir. 2016;32:3737–3745. DOI: 10.1021/acs.langmuir.6b00538

[72] Henn, G.; Stamm, M.; Poths, H.; Rücker, M.; Rabe, J. P. Influence of order in thin smectic polymer films on the structure at the surface. Phys. B. 1966;221:174–184.

[73] Mensinger, H.; Stamm, M.; Boeffel, C. Order in thin films of a liquid crystalline polymer. J. Chem. Phys. 1992;96:3183–3190.

[74] Elben, H.; Strobl, G.. Smectic surface structures in the isotropic phase of liquid-crystalline polymers studied by x-ray reflectivity. Macromolecules. 1993;26:1013–1018.

[75] van der Wielen, M. W. J.; Cohen Stuart, M. A.; Fleer, G. J.; de Boer, D. K. G.; Leenaers, A. J. G.; Nieuwhof, R. P.; Marcelis, A. T. M.; Sudhölter, E. J. R. Order in thin films of side-chain liquid-crystalline polymers. Langmuir. 1997;13:4762−4766.

[76] van der Wielen, M. W. J.; Cohen Stuart, M. A.; Fleer, G. J. Autophobicity and layering behavior of thin liquid-crystalline polymer films. Langmuir. 1998;14:7065–7071.

[77] Wu, J.-S.; Fasolka, M. J.; Hammond, P. T. Mixed surface morphologies of well-defined smectic diblock copolymer ultrathin films. Macromolecules. 2000;33. DOI: 1108-1110

[78] Morikawa, Y.; Nagano, S.; Watanabe, K.; Kamata, K.; Iyoda, T.; Seki, T. Optical alignment and patterning of nanoscale microdomains in a block copolymer thin film. Adv. Mater. 2006;18:883−886.

[79] Uekusa, T.; Nagano, S.; Seki, T. Highly ordered in-plane photoalignment attained by the brush architecture of liquid crystalline azobenzene polymer. Macromolecules. 2009;42:312–318.

[80] Haque, H. A.; Kakehi, S.; Hara, M.; Nagano, S.; Seki, T. High density liquid-crystalline azobenzene polymer brush attained by surface-initiated ring-opening metathesis polymerization. Langmuir. 2013;29:7571–7575.

[81] Asaoka, S.; Uekusa, T.; Tokimori, H.; Komura, M.; Iyoda, T.; Yamada, T.; Yoshida, H. Normally oriented cylindrical nanostructures in amphiphilic PEO–LC diblock copolymers films. Macromolecules. 2011;44:7645−7658.

[82] Fukuhara, K.; Fujii, Y.; Nagashima, Y.; Hara, M.; Nagano, S.; Seki, T. Liquid-crystalline polymer and block copolymer domain alignment controlled by free-surface segregation. Angew. Chem. Int. Ed. 2013;52:5988–5991.

[83] Komura, M.; Yoshitake, A.; Komiyama, H.; Iyoda, T. Control of air-interface-induced perpendicular nanocylinder orientation in liquid crystal block copolymer films by a surface-covering method. Macromolecules. 2015;48:672−678.

[84] Tanaka, D.; Nagashima, Y.; Hara, M.; Nagano, S.; Seki, T. Alternation of side-chain mesogen orientation caused by the backbone structure in liquid-crystalline polymer thin films. Langmuir. 2015;31:11379–11383.

[85] Swaraj, S.; Wang, C.; Yan, H.; Watts, B.; Lüning, J.; McNeill, C. R.; Ade, H. Nano Lett. Nanomorphology of Bulk Heterojunction Photovoltaic Thin Films Probed with Resonant Soft X-ray Scattering. 2010;10:2863–2869.

[86] Chen, W.; Xu, T.; He, F.; Wang, W.; Wang, C.; Strzalka, J.; Liu, Y.; Wen, J.; Miller, D. J.; Chen, J.; Hong, K.; Yu, L.; Darling, S. B. Nano Lett. Hierarchical Nanomorphologies Promote Exciton Dissociation in Polymer/Fullerene Bulk Heterojunction Solar Cells. 2011;11:3707–3713.

[87] Wang, C.; Lee, D. H.; Hexamer, A.; Kim, M. I.; Zhao, W.; Hasegawa, H.; Ade, H.; Russell, T. P. Nano Lett. Defining the Nanostructured Morphology of Triblock Copolymers Using Resonant Soft X-ray Scattering. 2011;11:3906–3911.

[88] Wang, C.; Hexemer, A.; Nasiatka, J.; Chan, E. R.; Young, A. T.; Padmore, H. A.; Schlotter, W. F.; Lüning, J.; Swaraj, S.; Watts, B.; Gann, E.; Yan, H.; Ade, H. IOP Conf. Ser.: Mater. Sci. Eng. Resonant Soft X-ray Scattering of Polymers with a 2D Detector: Initial Results and System Developments at the Advanced Light Source. 2010;14:012016.

[89] Gann, E.; Young, A. T.; Collins, B. A.; Yan, H.; Nasiatka, J.; Padmore, H. A.; Ade, H.; Hexemer, A.; Wang, C. Rev. Sci. Instrum. Soft x-ray scattering facility at the Advanced Light Source with real-time data processing and analysis. 2012;83:045110.

[90] Watts, B.; Swaraj, S.; Nordlund, D.; Lüning, J.; Ade, H. J. Chem. Phys. Calibrated NEXAFS spectra of common conjugated polymers. 2011;134:024702.